



Deliverable D2.12:
**High level radioactive waste package –
Characterization of glass/steel/buffer interaction
experiments**

Work Package [ACED](#)

The project leading to this application has received funding from the European Union's Horizon 2020 research and innovation programme under grant agreement No 847593.



<http://www.ejp-urad.eu/>

Document information

Project Acronym	EURAD
Project Title	European Joint Programme on Radioactive Waste Management
Project Type	European Joint Programme (EJP)
EC grant agreement No.	847593
Project starting / end date	1st June 2019 – 30 May 2024
Work Package No.	WP2
Work Package Title	Assessment of Chemical Evolution of ILW and HLW Disposal Cells
Work Package Acronym	ACED
Deliverable No.	2.12
Deliverable Title	High level radioactive waste package – Characterization of glass/steel/buffer interaction experiments
Lead Beneficiary	CEA
Contractual Delivery Date	June 2022
Actual Delivery Date	May 2023
Type	Report
Dissemination level	Public
Authors	Stéphane Gin (CEA), Alexis Delanoë (CEA), Florent Tocino (EDF), Karine Ferrand (SCK CEN), Jules Goethals (Subatech), Jérôme Sterpenich (University of Lorraine), Margit Fabian (MTA EK)

To be cited as:

Gin, S., Delanoë, A., Tocino, F., Ferrand, K., Goethals, J., Sterpenich, J., and Fabian, M. (2022): High level radioactive waste package – Characterization of glass/steel/buffer interaction experiments. Final version as of 04.05.2023 of deliverable D2.12x of the HORIZON 2020 project EURAD. EC Grant agreement no: 847593.

Disclaimer

All information in this document is provided "as is" and no guarantee or warranty is given that the information is fit for any particular purpose. The user, therefore, uses the information at its sole risk and liability. For the avoidance of all doubts, the European Commission has no liability in respect of this document, which is merely representing the authors' view.

Acknowledgement

This document is a deliverable of the European Joint Programme on Radioactive Waste Management (EURAD). EURAD has received funding from the European Union's Horizon 2020 research and innovation programme under grant agreement No 847593.

Status of deliverable		
	By	Date
Delivered (Lead Beneficiary)	Stéphane Gin	4 April 2022
Verified (WP Leader)	Diederik Jacques	21 June 2022
Reviewed (Reviewers)	Christelle Martin	15 December 2022
Verified (WP Leader)	Diederik Jacques	02 May 2023
Approved (PMO)	Louise Théodon	04 May 2023
Submitted to EC (Coordinator)	Andra	04 May 2023

Executive Summary

The main objective of the ACED work package (Assessment of Chemical Evolution of ILW and HLW Disposal Cells) in EURAD is to improve methodologies to obtain multi-scale quantitative models for the description of the chemical evolution at the disposal cell scale and to derive robust mathematical models including the most relevant processes.

For the interface and waste package scale, existing data on materials and material interfaces are combined with data from running experiments at the beginning of the project and dismantled during the course of the project as well as few complementary new experimental set-ups for evaluating the process integration methodology. While the interface scale investigations concentrate on steel-cement and steel-clay interfaces, long-term concrete degradation and implications of waste degradation are the focus at the waste package scale.

The subtask 3.1 concerns the first upscaling step from the relatively isolated processes at interfaces to repository sub-systems, representative for high-level radioactive waste (HLW) packages, where chemical and physical processes might be closely intertwined.

In case of HLW and according to existing HLW disposal concepts in Europe, the subtask 3.1 concentrates on the study of three experimental systems: « Glass/steel/clay » to « Glass/steel/cement » with an intermediate case « Glass/steel/cement buffer/clay »

These systems allow to study the different interfaces expected in HLW disposal cells with vitrified waste, metallic components, presence of cementitious material and near-field host rock.

This deliverable gives a detailed overview of information available about the following experiments:

Glass/Steel/Clay experiment performed by CEA and running for 6.1 years at 50°C (chapter 2),

Glass/Steel/Clay batch experiment performed by MTA and running for 1 year at 80°C (chapter 3),

Glass/Steel/Cement-bentonite/Clay experiment at 70°C by EDF and launched in April 2018 (chapter 4),

Glass/Steel/Cement experiment carried out by SCK-CEN on 20-25°C between 2009 and 2013 (chapter 5).

The different modelling approach began with the experimental data already available at the beginning of ACED. Here more data are provided that will be used in subtask 3.2 and Task 4 for the modelling effort.

Table of content

Executive Summary.....	4
Table of content.....	5
List of figures	7
List of Tables	11
Glossary.....	12
1 Introduction	14
2 Experiment 1: Glass/Steel/Clay system, 50°C	17
2.1 Background.....	17
2.2 Description.....	17
2.3 Materials involved: Chemical composition	18
2.3.1 COx claystone:	18
2.3.2 Synthetic pore water:	18
2.3.3 SON68 glasses coupons:	18
2.3.4 Iron piece	18
2.4 Solid or interface characterization	19
2.4.1 Methods	19
2.4.2 Results.....	19
2.4.3 Details of the characterizations	21
2.5 Analysis of the leaching solution	31
2.6 Other tests and characterization.....	32
2.6.1 LA-ICP-MS in the COx, Elementary Analysis.....	32
3 Experiment 2: Glass/Steel/Clay system, 80°C	34
3.1 Background.....	34
3.2 Description.....	34
3.3 Materials involved: Chemical composition	35
3.3.1 Glass - borosilicate glass.....	35
3.3.2 Steel: Fe powder (99%, from Acros Organics, CAS Nr. 7439-89-6).....	36
3.3.3 Clay: crushed claystone from Boda Claystone Formation (BCF)	36
3.4 Solid or interface characterization	37
3.4.1 Laboratory micro X-ray fluorescence (μ -XRF).....	37
3.4.2 SEM and Energy Dispersive X-ray (EDX) spectrometry	38
3.5 Analysis of leaching solution	46
3.6 Other tests and characterizations.....	48
3.6.1 X-ray diffraction (XRD) analysis	48

EURAD Deliverable D2.12 – High level radioactive waste package – Characterization of glass/steel/buffer interaction experiments

4	Experiment 3: Glass/Steel/Cement-bentonite/Clay system, 70°C	49
4.1	Background.....	49
4.2	Description.....	49
4.3	Materials involved: Chemical composition	51
4.4	Solid or interface characterization	51
4.4.1	SEM	51
4.5	Analysis of leaching solution	54
4.6	Other tests and characterization.....	54
5	Experiment 4: Glass/Steel/Cement system, 25°C.....	55
5.1	Background.....	55
5.2	Description.....	55
5.3	Materials involved.....	57
5.3.1	Hardened ordinary Portland cement.....	57
5.3.2	Stainless Steel	58
5.3.3	Glass.....	58
5.4	Solid or interface characterization	59
5.4.1	Methods	59
5.4.2	Results.....	61
5.5	Analysis of the leaching solution	80
5.5.1	Methods, operating conditions and uncertainties	80
5.5.2	Results.....	81
5.6	Other tests and characterizations.....	83
5.6.1	Porosity and density measurements of HCP.....	83
5.6.2	SEM grey analyses.....	84
5.7	Main findings, conceptual models and input towards modelling	88
6	Conclusions	91
7	References	92

List of figures

Figure 1-1 – Overall scope of the project, together with the link to (sub)task and information exchange between tasks.....	14
Figure 1-2 – Interfaces of interest for HLW disposal.....	16
Figure 2-1 – Schematic representation of the experiment	17
Figure 2-2 – Schematic representation of the glass/iron interface characterizations	19
<i>Figure 2-3– Backscattered electron micrograph of the sample after 6.1 years. Profile along which several variables are measured (Figure 2-4) is indicated as well.....</i>	<i>21</i>
Figure 2-4 – GAL thickness, Si/Zr ratio and Fe/Si ratio along the glass surface (Figure 2-3) after 6.1 years. The orange zone indicates the contact length between the glass and the iron; the white zone indicates direct contact with COx.	22
Figure 2-5 – SEM micrograph of the GAL (secondary electron for the 2.5 years sample, and backscattered electron for the 6.1 image). Note: The characteristics of the inner-GAL (i-GAL) evidenced on the image is not described in the present report).....	23
Figure 2-6 – SEM-EDX micrograph of the GAL after 2.5 years and 6.1 years. These EDX refer to SEM micrograph presented on Figure 2-5.....	24
Figure 2-7 – FIB thin foil of the GAL after the 6.1 years.....	25
Figure 2-8 – HRTEM characterizations of the GAL iron phyllosilicates	26
Figure 2-9 – STXM Fe L-edge spectra in the GAL and GAL precipitate.....	26
Figure 2-10 – STXM spectra at Si K-edge in the GAL and GAL precipitate	27
Figure 2-11 – Isotopic ²⁹ Si enrichment in the COx at the glass/COx interface after 6.1 years	28
Figure 2-12 – ICP after 6.1 years: backscattered micrograph (left) and SEM-EDX micrographs (right)	28
Figure 2-13 – STXM spectra at Fe L-edge in ICP	30
Figure 2-14 – STXM spectra at Si K-edge in ICP silicates.....	30
Figure 2-15 – Schematic representation of the pore water collection.....	31
Figure 2-16 – LA-ICP-MS characterizations at the glass/COx interface for Zr, Nd, Zn, La, Li and Mo	32
Figure 2-17 – LA-ICP-MS characterizations at the glass/COx interface for Fe and Si	32
Figure 2-18 – LA-ICP-MS characterizations at the glass/COx interface for Na, Mg, Be and B	33
Figure 3-1 – Schematic view (gray areas: internal and external Teflon vessel, blue area: synthetic pore water, brown area (middle) clay-iron-glass mixture) and physical dimensions of the experiments.	34
Figure 3-2 - Experimental setup of the glass/steel/clay systems.	35
Figure 3-3 – Elemental maps of glass/Fe/clay sample after 3 months experiment	37
Figure 3-4 – Elemental maps of glass/Fe/clay sample after 7 months experiment.	38
Figure 3-5 – Elemental maps of glass/Fe/clay sample after 12 months experiment	38
Figure 3-6 – SEM backscattered electron images on glass/Fe/clay sample after 3M treatment (solids of interest are marked as gl: glass, cl: clay and Fe)	39
Figure 3-7 – SEM backscattered electron images on glass/Fe/clay sample after 7M treatment.....	39

Figure 3-8 – SEM backscattered electron image and the corresponding EDX elemental maps on sample 7M.....	41
Figure 3-9 – SEM backscattered electron image and the corresponding EDX elemental maps on sample 7M.....	42
Figure 3-10 – SEM results after 12M, secondary (left, bottom) and backscattered electron image (right) of characteristic areas.	43
Figure 3-11 – Diffraction pattern of glass/Fe/clay mixture in function of treatment time.	48
Figure 4-1 – Stainless steel reactors.....	49
Figure 4-2 – Stainless steel reactor schematic representation (without buffer).....	50
Figure 4-3 – AVM glass sample monolith facing steel after being dissolved for 6 months.....	52
Figure 4-4 – Alteration layer thickness measured on AVM glass after 6, 12, 24 and 36 months. Steel canister (A), steel canister coated with magnetite (B) and “Sandwich” (C).....	52
Figure 4-5 – Alteration layer thickness measured on AVM glass (with buffer) after 6, 12, 24 and 36 months. Steel canister (A), steel canister coated with magnetite (B) and “Sandwich” (C).	53
Figure 4-6 – Alteration layer thickness measured on SON 68 glass after 6, 12, 24 and 36 months. Steel canister (A), steel canister coated with magnetite (B) and “Sandwich” (C).....	53
Figure 4-7 – Alteration layer thickness measured on SON 68 glass (with buffer) after 6, 12, 24 and 36 months. Steel canister (A), steel canister coated with magnetite (B) and “Sandwich” (C).	54
Figure 5-1 – Experimental setup for the integrated tests (hardened ordinary Portland cement paste/stainless steel filter/glass powder).....	55
Figure 5-2 – EDXS mapping (a) and SEM micrograph (b) of the interface between SS filter and HCP in the SM539 cell. Identified phases are brownmillerite (C4AF), alite (C3S), belite (C2S), Inner hydration products (Inner HP), tobermorite like C-S-H (Tb like C-S-H), Prtl (portlandite), monosulfoaluminate and ettringite mixture (S-containing AFt/AFm mixture), and Secondary alteration products (S.A.P).	63
Figure 5-3 – Ternary diagram CaO-SiO ₂ -Al ₂ O ₃ of SEM-EDXS analyses showing the plots of the chemical analyses of the OPC phases (C2S, C3S, portlandite, CSH, fibrous cement phase), the SON68 glass, the Secondary Alteration Phases (S.A.P.) next to glass grains (at the rim of grains), next to OPC paste. Reference minerals: tricalcium aluminate Ca ₃ Al ₂ O ₆ ; ettringite Ca ₆ Al ₂ (SO ₄) ₃ (OH) _{12.26} H ₂ O; alite Ca ₃ SiO ₅ ; larnite Ca ₂ SiO ₄ ;katoite Ca ₃ Al ₂ (SiO ₄) _{3-x} (OH) _{4x} x=1.5-3; gehlenite Ca ₂ Al(AlSi)O ₇ ; tobermorite Ca ₅ Si ₆ O ₁₆ (OH) ₂ •4(H ₂ O); stratlingite (Ca ₂ Al ₂ SiO ₃ (OH) ₈ :4H ₂ O); gismondite (Ca ₂ Al ₄ Si ₄ O ₁₆ :9H ₂ O); brownmillerite (Ca ₂ (Al,Fe ³⁺) ₂ O ₅), gyrolite NaCa ₁₆ Si ₂₃ AlO ₆₀ (OH) ₈₋₁₄ (H ₂ O).....	63
Figure 5-4 – EDXS mapping (a) and SEM micrograph (b) of the interface between SS filter and HCP in the SON68 cell. Identified phases are brownmillerite (C4AF), alite (C3S), belite (C2S), Inner hydration products (Inner HP), tobermorite like C-S-H (Tb like C-S-H), Secondary alteration products (S.A.P).	64
Figure 5-5 – Ternary diagram CaO- SiO ₂ -Al ₂ O ₃ of SEM-EDXS analyses showing the plots of the chemical analyses of the OPC phases (C2S, C3S, portlandite, CSH, fibrous cement phase), the SON68 glass, the Secondary Alteration Phases (S.A.P.) next to glass grains (at the rim of grains), next to OPC paste. Reference minerals: tricalcium aluminate Ca ₃ Al ₂ O ₆ ;ettringite Ca ₆ Al ₂ (SO ₄) ₃ (OH) _{12.26} H ₂ O; alite Ca ₃ SiO ₅ ; larnite Ca ₂ SiO ₄ ; katoite Ca ₃ Al ₂ (SiO ₄) _{3-x} (OH) _{4x} x=1.5-3; gehlenite Ca ₂ Al(AlSi)O ₇ ; tobermorite Ca ₅ Si ₆ O ₁₆ (OH) ₂ •4(H ₂ O); stratlingite (Ca ₂ Al ₂ SiO ₃ (OH) ₈ :4H ₂ O); gismondite (Ca ₂ Al ₄ Si ₄ O ₁₆ :9H ₂ O); brownmillerite (Ca ₂ (Al,Fe ³⁺) ₂ O ₅), gyrolite NaCa ₁₆ Si ₂₃ AlO ₆₀ (OH) ₈₋₁₄ (H ₂ O).....	65
Figure 5-6 – SEM-EDXS mapping of the SM539 glass grains at the vicinity of the stainless steel filter (a) together with quantitative EDXS analyses of the rim and cores of the grains (b) and a BSE picture displaying the different alteration patterns of SM539 glass grains located at the contact with the stainless steel filters (c).	66

Figure 5-7 – SEM-EDXS mapping of the SON68 glass grains at the vicinity of the SS filter (a) together with quantitative EDXS analyses of the rim and cores of the grains (b) and the location of the SEM EDXS mapping (c)..... 67

Figure 5-8 – XRD pattern of the HCP slice collected in the unaltered area (blue) and at the interface (red) with the stainless steel filter in the SM539 cell. The XRD pattern of a CIBELCOR® HCP cured for 20 days is given for comparison..... 68

Figure 5-9 – XRD pattern of the HCP slice collected in the unaltered area (blue) and at the interface (red) with the stainless steel filter in the SON68 cell. The XRD pattern of a CIBELCOR® HCP cured for 20 days is given for comparison..... 68

Figure 5-10 – TG-DSC measurements of the samples a) HCP-SON68 filter, b) HCP-SM539 filter and c) CIBELCOR® cement paste cured for 20 days. TG and DSC measurements are shown as black and blue lines respectively. 70

Figure 5-11 – Raman spectra of the precipitates localized at the interface between the SS filter and the HCP in the SON68 cell. The analysed spots are localized in the associated BSE-SEM picture..... 72

Figure 5-12 – Raman spectra of a precipitate localized at the interface between the SS filter and the HCP in the SM539 cell. The analysed spots are localized in a BSE image (spot 1) and an optical micrograph (spot 2). 73

Figure 5-13 – LA-ICP-MS profile measurements of major constituting elements across the hydrated cement paste for the SM539 cell (a) and for the SON68 cell as well as the SEM SE pictures of the sample SM539 (c) and SON68 (d) after laser ablation. The standard deviations are given at 95% confidence interval. Dots are connected for a better visualization..... 75

Figure 5-14 – Line mode LA-ICP-MS profile measurements of boron across the cement paste for the SM539 and SON68 cell (a) and (b) and spot mode LA-ICP-MS measurements of boron in the cell SM539 (c) and SON68 (d). Profiles 1 are only qualitative and correspond to the same profile as the major oxides and profile 2 correspond to profiles acquired in another cross section. The standard deviations are given at 95% confidence interval. Dots are connected for a better visualization..... 76

Figure 5-15 – Line mode LA-ICP-MS profile measurements of lithium across the cement paste for the SM539 and SON68 cell (a) and spot mode LA-ICP-MS measurements of lithium in the cell SM539 (b) and SON68 (c) . Profiles 1 are corresponding to the same profiles as the major constituent oxide ones and profile 2 correspond to a profile acquired in another cross section. The standard deviations are given at 95% confidence interval. Dots are connected for a better visualization..... 78

Figure 5-16 – LA-ICP-MS alkali profiles across the cement paste for the SON68 cell. Dots are connected for a better visualization. The standard deviations are given at 95% confidence interval. First points of the profiles are not presented for clarity reasons 79

Figure 5-17 – SEM-BSE image of LA-ICP-MS localized spot analyses of SM539 glass grains at the interface with SS filter (a) along with their B and Li content..... 80

Figure 5-18 – SEM-BSE image of LA-ICP-MS localized spot analyses of SON68 glass grains at the interface with SS filter along with their chemical composition..... 80

Figure 5-19 – Annotated BE-SEM images of the HCP in the SM539 cell (a) and in the SON68 cell (b) at a distance greater than 400 µm from interface, along with the corresponding maps which show coarse porosity (red), Very porous products (VPP pink), Hydration Products (HP blue), Unreacted Cement (UC green). 85

Figure 5-20 – BE-SEM images of the HCP at the interface with SM539 glass (a) and SON68 glass (b), along with the gray level histograms and the corresponding maps which show fractures (brown), macroporosity (red), newly formed C-S-H with low Ca/Si ratio (light blue), hydration products (HP, blue), carbonated hydrates (orange), unreacted cement (UC, green) and fractures (brown)..... 85

EURAD Deliverable D2.12 – High level radioactive waste package – Characterization of glass/steel/buffer interaction experiments

Figure 5-21 – Mineralogical and microstructural evolution in the HCP for SM539 cell obtained by gray level analyses except for porosity, carbonates and portlandite content in the unaltered area (100µm to 1mm). In this latter, porosity was obtain from water porosity measurement and portlandite and carbonate contents were obtained by TG-DSC measurements..... 87

Figure 5-22 – Mineralogical and microstructural evolution in the HCP for SON68 cell obtained by gray level analyses except for porosity, carbonates and portlandite content in the unaltered area (200µm to 1mm). In this latter, porosity was obtain from water porosity measurement and portlandite and carbonate contents were obtained by TG-DSC measurements..... 87

List of Tables

Table 2-1 – Theoretical composition of synthetic groundwater used for the experiment.....	18
Table 2-2 – pH and Eh of the synthetic groundwater used for the experiment.....	18
Table 2-3 – Composition of the SON68 glasses coupons	18
Table 2-4 – GAL and ICP thickness	22
Table 2-5 – SEM-EDX composition in the Pristine Glass (PG), GAL and GAL precipitate in wt.%.....	24
Table 2-6 – SEM-EDX composition in the Si-free ICP and ICP with Si in wt. %.....	28
Table 2-7 – Si and Fe enrichment determined by Tof-SIMS.....	31
Table 3-1 – Mineral composition of the rock types.....	36
Table 3-2 – The chemical composition of synthetic pore water (SBPW).	37
Table 3-3 – SEM/EDX results: elemental composition after 3M (wt.%)	39
Table 3-4 – SEM/EDX results: elemental composition after 7M (wt.%)	40
Table 3-5 – SEM/EDX results: elemental composition after 12M (wt.%)	43
Table 3-6 – ICP-OES and IC results, compared the 3-7-12 months sampling	46
Table 3-7 – Normalized mass loss and glass dissolution rate for boron.....	47
Table 4-1 – Configurations tested	50
Table 4-2 – Schedule	50
Table 4-3 – Mass of reagents for 1 kg of solution	51
Table 5-1 – Material specifications for the integrated tests (uncertainties are given at 95 % confidence interval).....	55
Table 5-2 – Composition of the synthetic cementitious water referred to as YCWCa in mg/L.	56
Table 5-3 – Schedule of the integrated test	56
Table 5-4 – Average analytical composition in weight % of CEM I 42.5 HSR5R LA CCB Portland cement provided by CIBELCOR®	57
Table 5-5 – Nominal composition of SON68 and SM539 HE 540-12 glasses in weight %.	58
Table 5-6 – Operating conditions for the LA-ICP-MS measurements.....	60
Table 5-7 – Volumetric and weight percent of portlandite and carbonates of the HCP coming from the cell SM539 and SON68 as well as a CIBELCOR® HCP cured for 20 days. The Loss on Ignition (LOI) values at 1000°C are also given.....	70
Table 5-8 – pH values measured at room temperature in the integrated tests.....	81
Table 5-9 – Element concentrations in mg/L in the integrated tests	82
Table 5-10 – Glass dissolution rates in $\text{g}\cdot\text{m}^{-2}\cdot\text{d}^{-1}$ determined from different leaching tests in YCWCa; the uncertainty at 2 sigma is <15%.	83
Table 5-11 – Water porosity measurement of the cement paste samples collected in the SM539 and SON68 with filter cells and of the CIBELCOR® cement paste cured for 20 days.	83

Glossary

ACED	Assessment of Chemical Evolution of ILW and HLW Disposal Cells
ASR	Alkali Silica Reaction
AVM	Atelier de Vitrification de Marcoule (Marcoule vitrification facility)
BE	Backscattered electron
C-A-S-H	Calcium Alumina Silicate Hydrate
CIGEO	Centre Industriel de stockage GEOlogique
COx	Callovo-Oxfordian
C-S-H	Calcium Silicate Hydrate
FIB	Focused Ion Beam
GAL	Glass Alteration Layer
HC	Hydrated Cement
HCP	Hydrated cement paste
HLW	High Level Waste
HR-LA-ICP-MS	High resolution-Laser Ablation-Inductively Coupled Plasma-Mass spectrometry
HRTEM	High-Resolution Transmission Electron Microscopy
ICP	Iron Corrosion Products
ICP-AES	Inductively Coupled Plasma – Atomic Emission Spectrometry
ICP-MS	Inductively Coupled Plasma – Mass Spectroscopy
ILW	Intermediate Level Waste
LA-ICP-MS	Laser Ablation ICP-MS
LIBS	Laser Induced Breakdown Spectroscopy
LIBS	Laser Induced Breakdown Spectroscopy
LOI	Loss on Ignition
OPC	Ordinary Portland Cement
PG	Pristine Glass
SEM EDX	Scanning Electron Microscopy with Energy Dispersive X-ray analysis
SEM	Scanning Electron Microscopy
SS filter	Stainless steel filter
STEM DF	Scanning Transmission Electron Microscopy, Dark Field
STXM	Scanning Transmission X-ray Microscopy
TEM	Transmission Electron Microscopy
TGA-DSC	Thermo Gravimetric analyses – Differential scanning calorimetry
ToF-SIMS	Time of Flight Secondary Ion Mass Spectrometry
UC	Unreacted Cement
URL	Underground Research Laboratory

EURAD Deliverable D2.12 – High level radioactive waste package – Characterization of glass/steel/buffer interaction experiments

W/C Water to cement ratio

YCWca Young water cement with calcium

Cement abbreviation notations:

C	CaO
S	SiO ₂
A	Al ₂ O ₃
H	H ₂ O
CH	Portlandite
C-S-H	Calcium Silicate Hydrate
C-A-S-H	Calcium Aluminium Silicate Hydrate
AFm	Aluminate Ferrite Monosulfate
Aft	Aluminate Ferrite Trisulfate

1 Introduction

The broader scope of the work package ACED is the assessment of the chemical evolution at the disposal cell scale involving interacting components/materials and thermal, hydraulic and/or chemical gradients by considering intermediate level waste (ILW) and high level waste (HLW) disposal concepts representative for different concepts throughout Europe. To increase the attention towards relevant materials and processes, the work package addresses ILW and HLW components up to the disposal cell scale. The study of the disposal cell in this WP ranges from microscale processes at interfaces between different materials up to interactions of waste packages with their immediate surrounding near field environment and the host rock.

The main objective is to improve methodologies to obtain multi-scale quantitative models for the chemical evolution at the disposal cell scale based on existing and new experimental data and process knowledge and to improve the description of the most relevant processes driving the chemical evolution into robust mathematical frameworks.

More specifically, ACED (Figure 1-1) seeks to:

- Compile and integrate the process level knowledge and description of reactivity at the interfaces between materials relevant for ILW and HLW disposal cells
- Develop and evaluate methodologies to integrate available process-level knowledge and processes into a multi-process and multi-scale modelling framework for assessing chemical evolution at the disposal cell level
- Propose and apply a step-wise scale-up process-based approach to identify (i) processes and features which control the chemical evolution for representative HLW and ILW disposal cells and (ii) to which detail and complexity these processes should be incorporated in models for different type of safety and performance related studies. The information gained through study of the more generic but European representative HLW and ILW disposal cells can later be used and adapted for more specific national disposal cell designs.

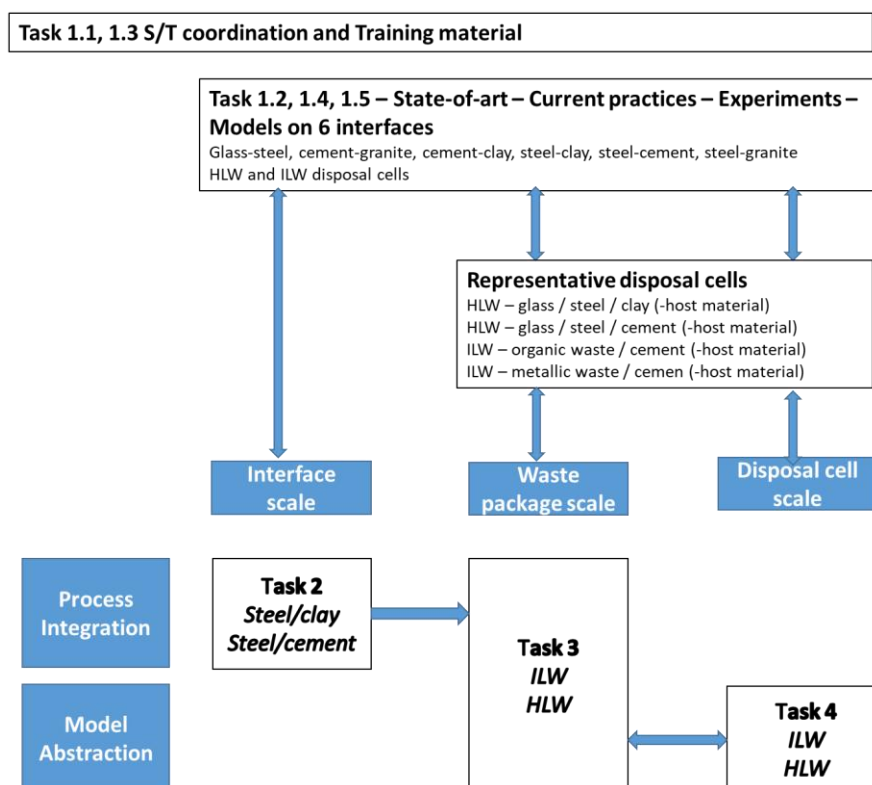


Figure 1-1 – Overall scope of the project, together with the link to (sub)task and information exchange between tasks.

Figure 1-2 – Interfaces of interest for HLW disposal

These systems allow for studying the different interfaces expected in HLW disposal cells with vitrified waste, metallic components (containers and possible overpack and liner), presence of cementitious material (e.g. a cement-base grout in the French concept and a cementitious overpack in the Belgian one) and near-field host rock. Although the experimental systems are set-up within a specific disposal concept, the sequence of interfaces represent a broad range of possibilities relevant for many concepts.

HL vitrified waste will be altered in contact with the host rock groundwater having drilled through the cementitious material (if present) and the corrosion products of metallic components. The glass alteration rate highly depends on the chemistry (pH, concentrations in silica, calcium and magnesium in solution) of the aqueous phase, and on the nature of corrosion products formed during the corrosion of the overpack before its failure.

This report provides

- a detailed overview of the selected existing experimental data with details on the used materials and methods,
- Results from solid and liquid characterization and their interpretation in terms of relevant mechanisms involved in the interaction between glass and surrounding materials.
- information that could be useful for modelling purposes.

2 Experiment 1: Glass/Steel/Clay system, 50°C

2.1 Background

Partner: CEA

Contact person: S. Gin (stephane.gin@cea.fr)

Written by: A. Delanoë

This experiment aims to investigate glass alteration in representative conditions of the disposal cell, after the canister failure. In this scenario, defined before the latest evolution of the CIGEO reference concept for HLW, the COx claystone is saturated with groundwater, which reacts with glass, steel canister and overpack.

2.2 Description

The experimental setup is shown on the Figure 2-1. Inside a COx claystone cylinder, two coupons of SON68 glass were inserted at the vicinity of an iron piece. One of the glass coupon was doped with ^{57}Fe and ^{29}Si to investigate their migration into the materials, while the second coupon remained undoped. The Callovo-Oxfordian claystone was saturated with synthetic pore groundwater. The mock-up was disposed into an oven at 50 °C under anoxic conditions. Two identical mock-ups were prepared and run in parallel for 2.5 and 6.1 years, respectively.

Each mock-up experiment was dismantled after the ageing process. The whole glass/steel/claystone system was dry-frozen to remove the water and embedded in a resin under vacuum. Then, inside a glove box (N_2 atmosphere), small samples were cross-sectioned, and polished up to 1 μm roughness, for further characterizations.

Post-mortem solids analysis were performed on a selection of samples to investigate chemical evolutions (SEM, SEM-EDX, Raman spectroscopy, Tof-SIMS, HRTEM and STXM). The results of the 2.5 years long experiment are already published (Carriere et al., 2021), and this report summarizes the main results from the two experiments.

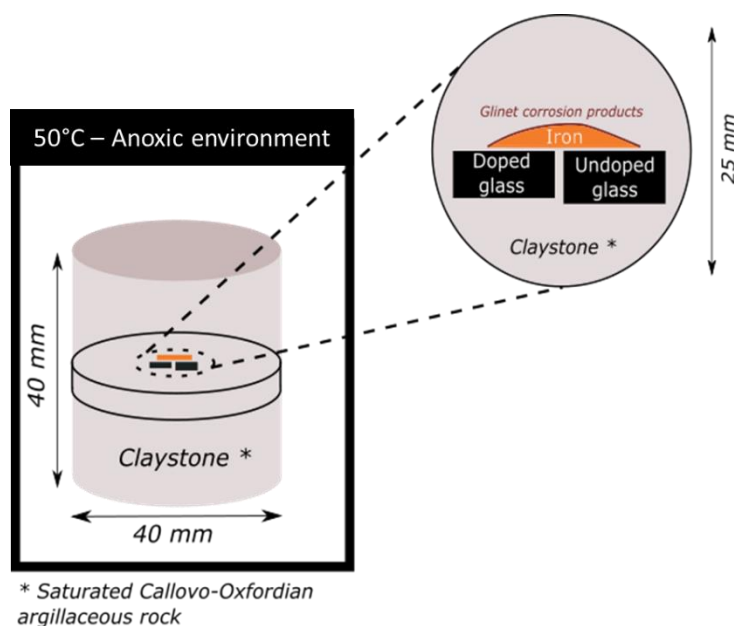


Figure 2-1 – Schematic representation of the experiment

2.3 Materials involved: Chemical composition

2.3.1 COx claystone:

The Callovo-Oxfordian claystone was provided by Andra, and comes from EST43482 drill of the Bure URL. No characterization was performed on the starting materials.

2.3.2 Synthetic pore water:

The claystone cylinder was saturated with synthetic groundwater. The theoretical composition of pore water in equilibrium with COx claystone (at 50°C) is presented in Table 2-1. The solution was not analysed, but pH and Eh were measured before the claystone core was saturated (Table 2-2).

Table 2-1 – Theoretical composition of synthetic groundwater used for the experiment

	Na	K	Ca	Mg	Sr	Si	Cl	SO ₄	HCO ₃
mg/L	966	39.1	397	99.6	17.5	9.8	1453	1345	232

Table 2-2 – pH and Eh of the synthetic groundwater used for the experiment

	pH (at 25°C)	Eh (at 25°C)
Theoretical	6.87	-140 mV/ENH
Measured	6.7	-190 mV/ENH

2.3.3 SON68 glasses coupons:

The doped glass coupons (10 mm x 10 mm x 2 mm) were made with 100% of ⁵⁷Fe and 50% of ²⁹Si (wt. %). The undoped coupon dimensions are 20 mm x 10 mm x 5 mm. The SON68 glass composition is presented in Table 2-3.

Table 2-3 – Composition of the SON68 glasses coupons

Oxides	SON68	Oxides	SON68
SiO ₂	45.85	NiO	0.74
B ₂ O ₃	14.02	MnO ₂	0.72
Na ₂ O	9.86	BaO	0.60
Al ₂ O ₃	4.91	Cr ₂ O ₃	0.51
CaO	4.04	Pr ₂ O ₃	0.44
Fe ₂ O ₃	2.91	SrO	0.33
ZrO ₂	2.65	P ₂ O ₅	0.28
ZnO	2.50	TeO ₂	0.23
Li ₂ O	1.98	Y ₂ O ₃	0.20
MoO ₃	1.70	Ag ₂ O	0.03
Nd ₂ O ₃	1.59	CdO	0.03
Cs ₂ O	1.42	SnO	0.02
Ce ₂ O ₃	0.93	Other	0.61
La ₂ O ₃	0.90		

2.3.4 Iron piece

The iron piece came from an archeological artefact recovered at the Glinet archaeological site (Normandy, France) (Saheb et al., 2010). This 450 years old nail is a low alloyed piece of steel (mainly ferritic) covered with corrosion products, which measures roughly 8 mm x 0.6 mm. The piece was cut

and the pristine face was placed at the vicinity of the glass coupons, while the aged face contacted the claystone (Figure 2-1).

2.4 Solid or interface characterization

2.4.1 Methods

A multi-scale approach was used to characterize the samples. The experimental method is described in Carriere et al. (2019). The analytical techniques used in this study are the same (SEM, SEM-EDS, μ -Raman spectroscopy, ToF-SIMS, FIB, HRTEM and STXM). LA-ICP-MS characterizations were also performed to determine ^{29}Si and ^{57}Fe migration into the surrounding claystone.

Note:

- ToF-SIMS characterizations were performed at Université de Lille (France)
- LA-ICP-MS characterizations were performed at Subatech laboratory (Nantes, France).
- FIB and high resolution TEM characterizations were performed at CIMAP laboratory (Caen, France).
- STXM characterizations were performed at Canadian Light Source

2.4.2 Results

The two mock-ups show many similarities. A schematic representation of the alteration pattern is presented on the Figure 2-2.

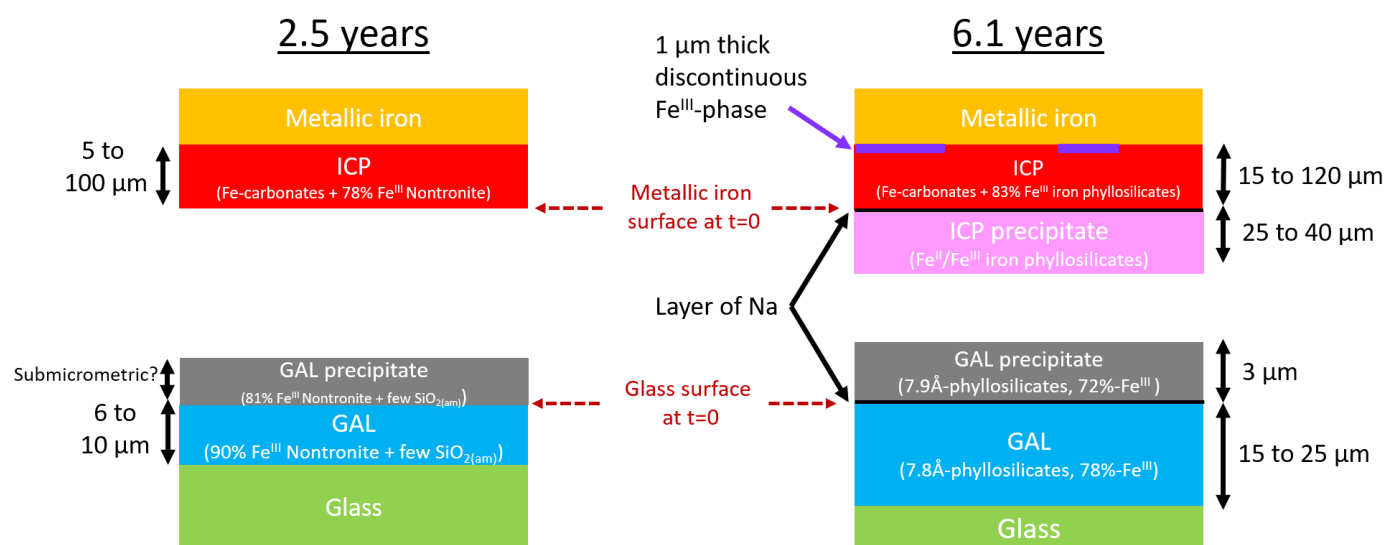


Figure 2-2 – Schematic representation of the glass/iron interface characterizations

2.4.2.1 Glass Alteration Layer

A glass alteration layer (GAL) is observed on the surface of the material. GAL thickness ranges from 6 to 10 μm after 2.5 years, and 15 to 25 μm after 6.1 years at the glass/iron interface. The GALs are composed of iron phyllosilicates, and $\text{SiO}_{2(\text{am})}$ as a minor phase according to STXM analysis (Carriere et al., 2021). Besides, a stack of sublayers was observed in the GAL (Figure 2-7), suggesting that a cyclic mechanism occurred during GAL formation.

Interestingly, phyllosilicates inter-reticular distances differ between the two experiments. After 2.5 years, 10.4 \AA -phases were observed (dehydrated smectite, assimilated to nontronite), while 7.8 \AA -phyllosilicates were observed in the longer experiment (could be serpentine phase). No smectite was detected after 6.1 years, which indicates serpentine is the only phase in the GAL. The Fe valence of the phyllosilicates was determined using STXM: smectite are mainly Fe^{II} -phase, while the serpentine like

phase valence is 22% Fe^{II} and 78% Fe^{III}. This Fe valence evolution associated with inter-reticular distance change could be in agreement with smectite destabilization mechanism published in the literature (Lantenois et al., 2005).

On the 6.1 years sample, neoformed phyllosilicates were identified on the GAL surface. The composition of this 3 µm thick layer is close to the GAL one (7.9 Å-phases, 28% Fe^{II} and 72% Fe^{III}) and is called hereafter “GAL precipitate”. Contrary to the GAL, the GAL precipitate is composed of a homogenous layer without a stack of sublayers (Figure 2-7). This GAL precipitate was not clearly detected on the 2.5 years system by SEM-EDX due to its small thickness, a submicrometric thick layer could be present.

Note: the GAL morphology depends on local conditions that certainly differ from one location to another. The GAL thickness is highly dependent on the glass/iron distance (Figure 2-4). The GAL thickness is higher at the glass/iron interface (15-25 µm as mentioned before), while at the glass/CO_x interface (i.e. far from iron coupon), the GAL is smaller (up to few micrometers). Nonetheless, the latter seems also to be composed of iron phyllosilicates as it was described for the GAL at the glass/iron interface.

2.4.2.2 Glass alteration rate

Based on the GAL thickness (GAL thickness corresponds to the altered glass thickness), glass alteration rate estimations are similar in both experiments: from $1.8 \cdot 10^{-2}$ to $3.0 \cdot 10^{-2}$ g.m⁻².d⁻¹ after 2.5 years and from $1.8 \cdot 10^{-2}$ to $2.5 \cdot 10^{-2}$ g.m⁻².d⁻¹ for the 6.1 years experiment. It corresponds to $r_0/5$ to $r_0/3$, where r_0 represents the initial dissolution rate at 50°C in CO_x groundwater (maximum dissolution rate in these conditions, $r_0 = 9.3 \cdot 10^{-2}$ g.m⁻².d⁻¹ (Jollivet et al., 2012)). This result strongly suggests that the GAL composed of iron phyllosilicates is not passivating, compared to SiO_{2(am)} passivating layer which residual alteration rate which is close to $r_0/1000$.

Due to the iron corrosion by pore water, glass alteration is influenced by the Fe-containing solution. Glass alteration released Si into the solution leading to the formation of iron phyllosilicates in the GAL, preventing the formation of a passivating amorphous silica gel.

2.4.2.3 Iron corrosion products

The iron corrosion products (ICP) thickness ranges from 5 µm to 100 µm after 2.5 years, and 15 to 120 µm after 6.1 years. They are formed at the expense of the iron piece. Two types of ICP are observed: (1) Si-free phases, and (2) Si-bearing phases. The Si-free phases are identified as iron carbonates, such as chukanovite (Fe₂(OH)₂CO₃) crystallized in a needle shape and siderite (FeCO₃) close to the metallic iron. The Si-bearing phases are poorly crystallized iron phyllosilicates, identified as smectite (nontronite, 22% Fe^{II} and 78% Fe^{III}) after 2.5 years. They are not clearly identified after 6.1 years (17% Fe^{II} and 83% Fe^{III}) but could be a serpentine-like phase like the ones characterized in the GAL.

Furthermore, a 25 µm to 40 µm thick neo-formed precipitate is characterized on the ICP surface after 6.1 years, and is called hereafter “ICP precipitate”. It is composed of iron phyllosilicates. ICP precipitate is not reported after 2.5 years.

At the metallic iron/ICP interface, a 1 µm discontinuous thick layer is observed on the 6.1 years experiment. This layer is an Fe^{III}-rich iron oxide (2% Fe^{II} and 98% Fe^{III} according to STXM at Fe L-edge, Figure 2-13. It could be maghemite (γ-Fe₂O₃), magnetite (Fe₃O₄) or a maghemite/magnetite phase, as it was already reported in other experiments (Leon et al. 2017, Michelin et al. 2013). Such layer was not reported after 2.5 years by Carriere et al. (2021) as it could be submicrometric and thus not detectable by SEM-EDX.

2.4.2.4 Fate of Si and Fe

The fate of Fe and Si released from the glass is investigated by monitoring the distribution of ⁵⁷Fe and ²⁹Si using ToF-SIMS. Globally the results obtained for the 2.5 yr experiment are close for GAL and ICP: 91% of the Fe in the phyllosilicates comes from the corrosion of the iron piece. In the same way, around 1/3 of the Si contained in the phyllosilicates comes from the glass, while the remaining 2/3 is supplied by the silicate minerals present in the Cox. Similar results are evidenced by ToF-SIMS in the 6.1 years

system. Further investigations of ^{29}Si migration in the claystone using LA-ICP-MS demonstrated that even after 6.1 years some Si from the glass remains in the GAL. However, other elements from the glass, such as Mo, Nd, La, Zr, Li, and Zn migrated in the claystone up to a few hundreds of micrometres. (Figure 2-11, Figure 2-16).

Overall, these results suggest that the GAL is formed by the dissolution of the glass triggered by the precipitation of phyllosilicates, instead of in situ reorganization of the glassy network. In this case, neoformation of Si-Fe bearing phases prevents the reorganisation of the silicate network and thus the formation of a passivating film.

2.4.3 Details of the characterizations

The samples were investigated with a multi-scale approach, relying on different characterization techniques: SEM, SEM-EDX, Tof-SIMS, LA-ICP-MS, HRTEM, STXM at Si K-edge and STXM at Fe L-edge. The analytical method is detailed in Carriere 2021. The characterizations were mainly focused on the glass/iron interface. For each ageing duration (2.5 and 6.1 years), two area of interest are detailed in this report: the ICP and the GAL.

2.4.3.1 Evolution of the GAL along the glass surface

Figure 2-3 shows the 6.1 years altered sample after resin embedding, cross section cutting and polishing. The black area corresponds to the resin. The glass coupons are fractured probably due to the sample preparation (cutting or polishing step). The GAL and ICP are easily visible on this micrograph.

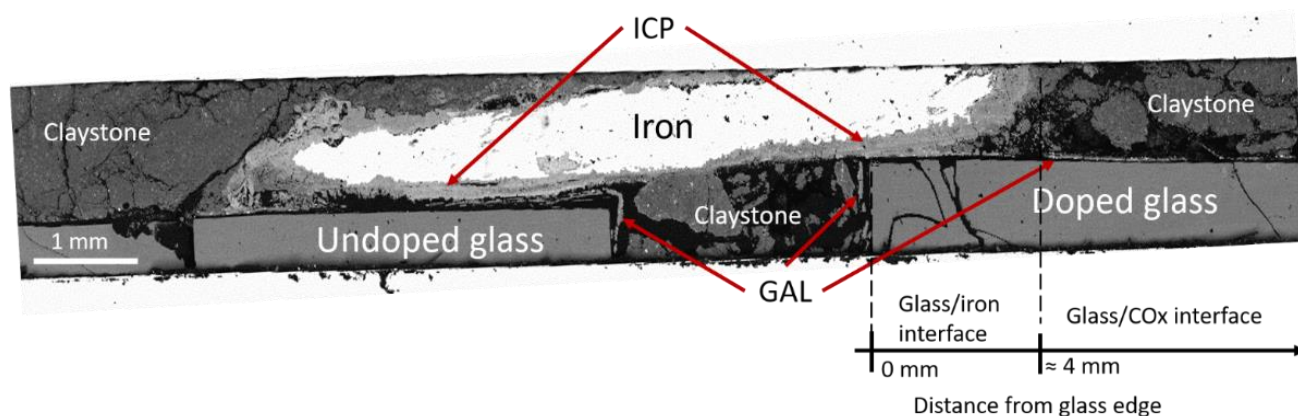


Figure 2-3– Backscattered electron micrograph of the sample after 6.1 years. Profile along which several variables are measured (Figure 2-4) is indicated as well.

The GAL was investigated along the glass surface, and the GAL thickness was measured considering Zr as a glass marker. A thickness change was evidenced (Figure 2-4), the GAL is thicker at the glass/iron interface than at the glass/COx interface (far from the iron piece).

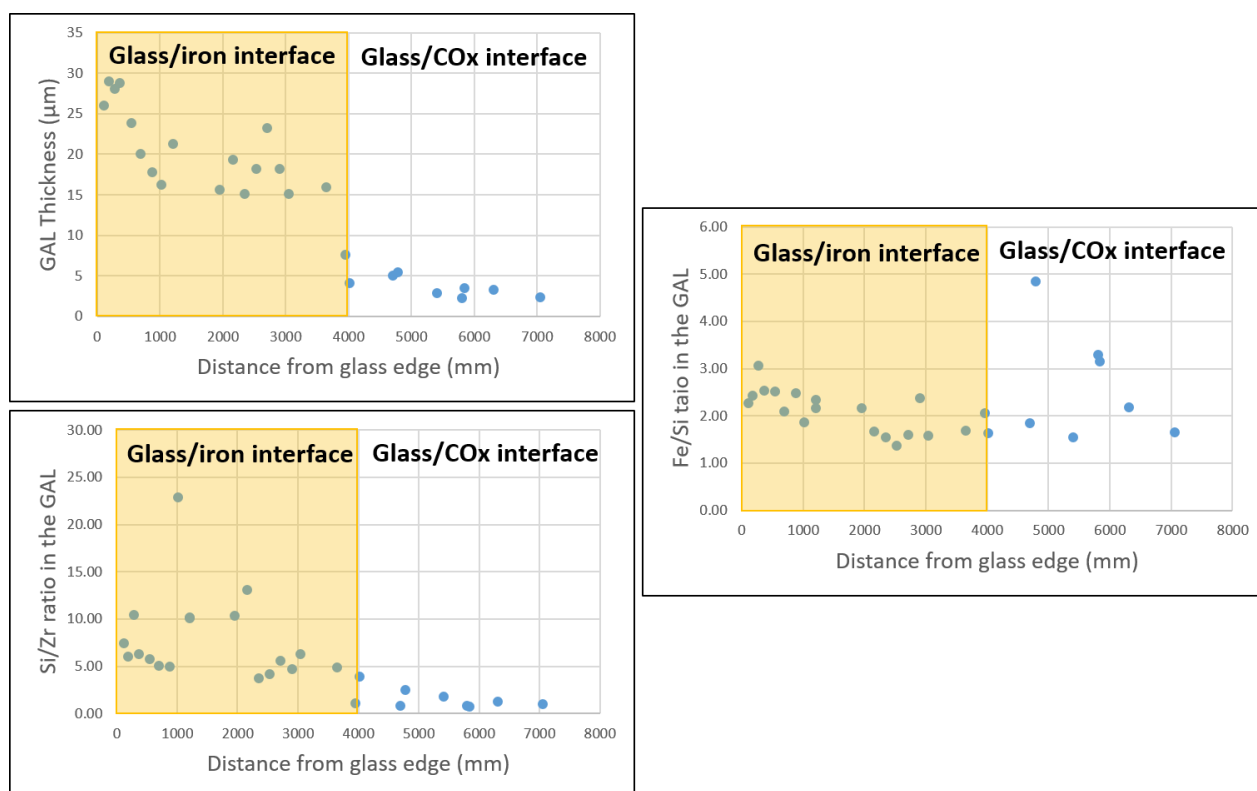


Figure 2-4 – GAL thickness, Si/Zr ratio and Fe/Si ratio along the glass surface (Figure 2-3) after 6.1 years. The orange zone indicates the contact length between the glass and the iron; the white zone indicates direct contact with COx.

The Fe/Si ratio remains constant along the whole surface, at around 2. It might indicate that the iron phyllosilicates are the same at the glass/iron and glass/COx interfaces. Nevertheless, the Si/Zr ratio change is observed between the two interfaces, from 5 to 1, respectively. This indicates that there is less Si in the GAL at the glass/COx interface. Once again, these results suggest that the mechanisms of GAL formation is strongly impacted by the precipitation of Fe-Si bearing minerals.

2.4.3.2 GAL and ICP thickness at glass/iron interface

The GAL thickness is estimated using SEM-EDX micrographs using Na and Zr elements as described below (section 2.4.3.3). The ICP thickness is determined using SEM backscattered images. The pristine steel piece contains cementite phases (Fe_3C), which are easily distinctive using SEM backscattered micrograph. Their presence in corroded steel allows ICP thickness determination. Cementite is considered in this experiment as a steel marker and allow to visualise the original interface between the steel foil and the glass (Figure 2-12).

Table 2-4 – GAL and ICP thickness

	2.5 years (from Carriere et al. 2021)	6.1 years
ICP	From 5 µm to 100 µm	From 15 µm to 120 µm

ICP precipitate	Not reported	25 μm to 40 μm
GAL precipitate	Unknown. Sub-micrometric?	3 μm
GAL	6 μm to 10 μm	15 μm to 25 μm

2.4.3.3 SEM-EDX characterizations in the GAL at glass/iron interface

The GAL is detected using Zr and Na elements. Zr is considered as a GAL marker in these experiments, as Zr is a glass component that is extremely insoluble during glass alteration, it remains in the GAL and allow to show the initial thickness of the glass. Al is not considered as a specific glass marker in this experiment, as Al is very common in COx. In addition, Na depletion is characteristic of the GAL, it is usually associated to ion-exchange between alkali and protons from the solution (Bouakkaz et al., 2016). Using this method, the GALs measure from 6 μm to 10 μm after 2.5 years, and from 15 μm to 25 μm after 6.1 years. SEM-EDX micrographs (Figure 2-6) suggest that GALs are composed of Si-O-Fe phases. The comparison of Fe/Zr ratios in the GAL and pristine glass (PG) evidenced an Fe enrichment in the GAL (Table 2-4).

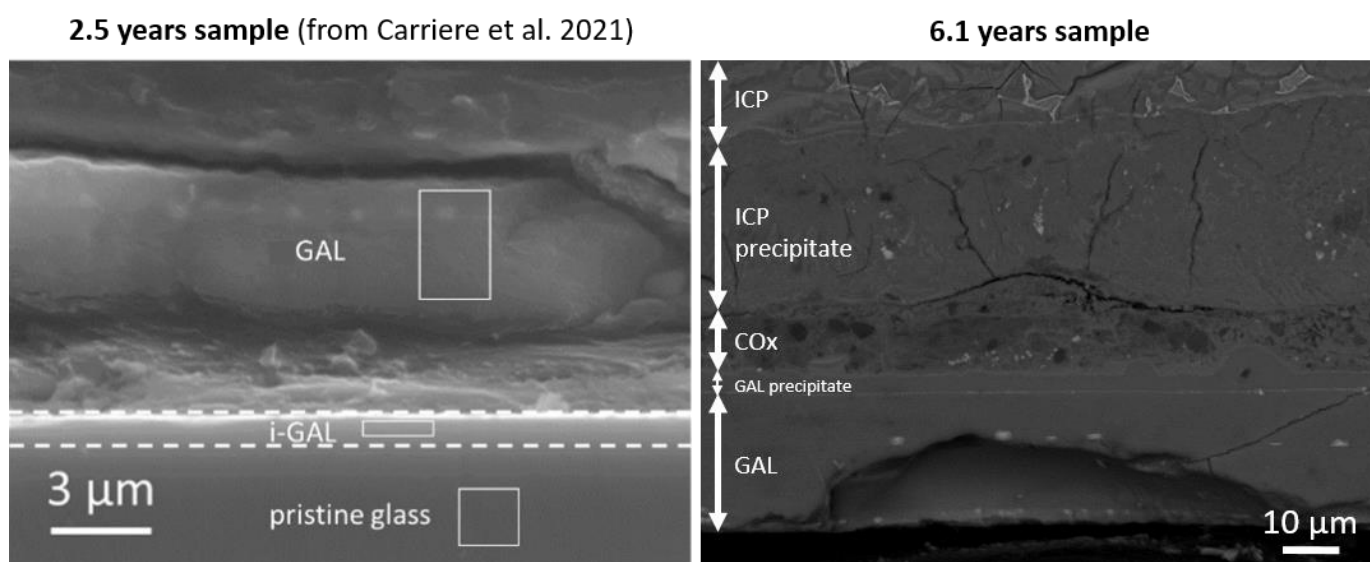


Figure 2-5 – SEM micrograph of the GAL (secondary electron for the 2.5 years sample, and backscattered electron for the 6.1 image). Note: The characteristics of the inner-GAL (i-GAL) evidenced on the image is not described in the present report).

GAL after 2.5 years (from Carriere et al. 2021)

GAL after 6.1 years

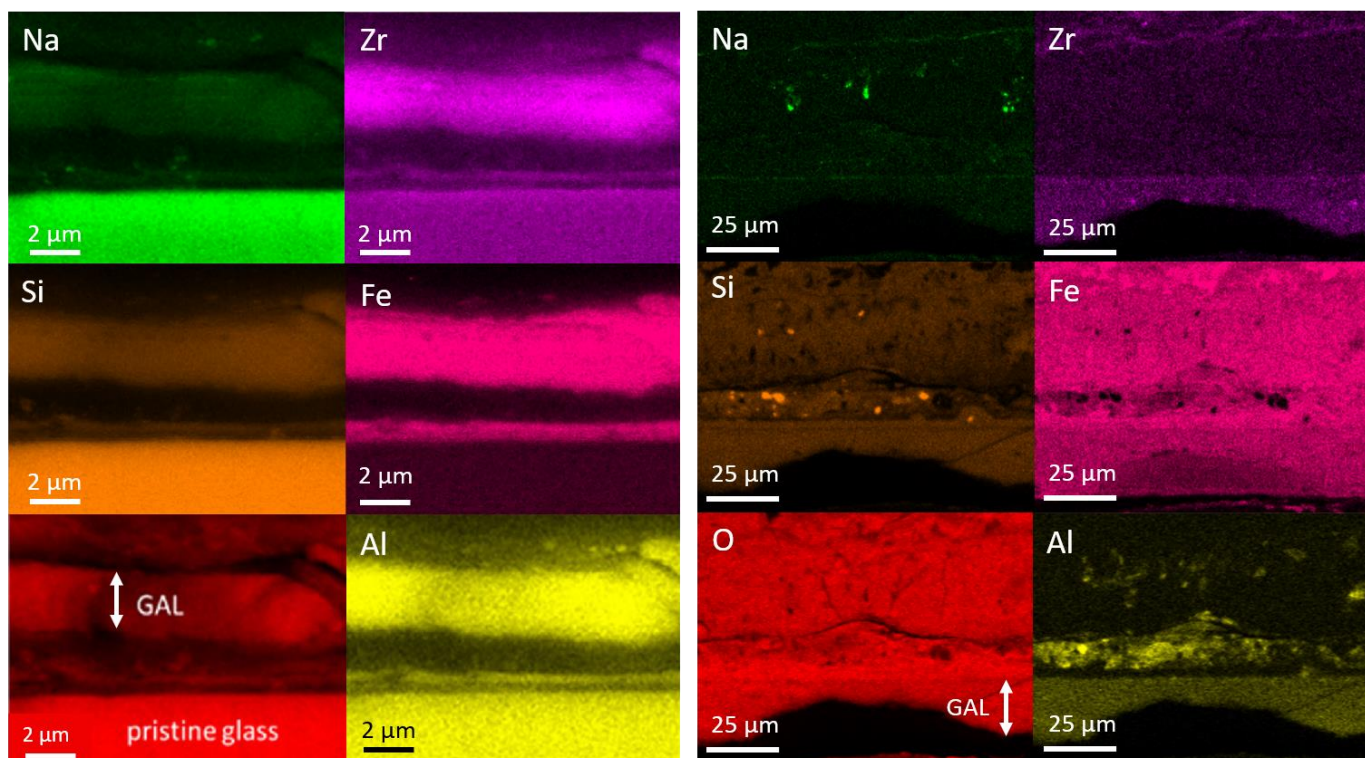


Figure 2-6 – SEM-EDX micrograph of the GAL after 2.5 years and 6.1 years. These EDX refer to SEM micrograph presented on Figure 2-5.

Table 2-5 – SEM-EDX composition in the Pristine Glass (PG), GAL and GAL precipitate in wt. %

	2.5 years (from Carriere et al. 2021)		6.1 years		
	PG	GAL	PG	GAL	GAL precipitate
O	44	36	51	42	42
Si	26	18	25	15	15
Fe	3.2	35	2.5	36	41
Na	4.5	n.d.	8.9	0.7	0.6
Al	3.2	5.5	3.2	3.0	0.5
Ca	3.2	1	3.2	0.4	0.2
Zr	2.7	4.1	2.6	2.0	0.1
Mo+Cs+Ba+La+Ce+Pr+Nd	10.5	n.d.	3.1	n.d.	0.2
Other elements	2.7	0.4	0.5	0.9	0.4
Si/Zr	9.6	4.4	9.6	7.5	-
Fe/Zr	1.2	8.6	1.0	18	-
Fe/Si	0.1	1.9	0.1	2.4	2.7

A 3 μm precipitate is observed on the GAL surface after 6.1 years (Figure 2-5). The SEM-EDX micrographs (Figure 2-6) and Table 2-4 show the absence of Zr. This indicates that this layer does not

originates from the glass, but is a neoformed iron silicates phase. This GAL precipitate is not clearly identified for the 2.5 years sample, as the phase thickness might be sub-micrometric which is below the SEM-EDX detection limit.

A thin layer of Na is observed on the SEM-EDX micrographs between the GAL and the GAL precipitate (Figure 2-6). As this layer is only observed for the 6.1 years old samples, it could be a marker of the original pristine glass surface. Na from the solution could be sorbed on the original glass surface to create a nanometric layer. Note that $K_{\alpha}(\text{Na})$ and $L_{\alpha}(\text{Zn})$ peaks overlap on EDX spectra. This layer need further investigations to identify the chemical composition of this nanometric layer.

Na spots/aggregates are visible on the SEM-EDX micrographs, between the GAL and the ICP. These Na spots correspond to pyrite particles/aggregates from claystone. Cox claystone particles could have migrated between glass coupon and iron coupon, during the settling of the experiment due to water resaturation (Figure 2-5, right image).

2.4.3.4 STEM DF images of the FIB thin foil in the GAL after 6.1 years at glass/iron interface

STEM DF images performed on thin foils prepared with FIB (100 nm thickness) strengthen the difference in composition between the GAL and the GAL precipitate identified by SEM-EDX. Figure 2-7 shows that the GAL is composed of different layers while the GAL precipitate is a homogenous phase. This difference discloses distinct mechanisms of formation between the two phases.

The FIB, STEM and HRTEM characterizations are a collaborative work with the CIMAP laboratory (Caen, France).

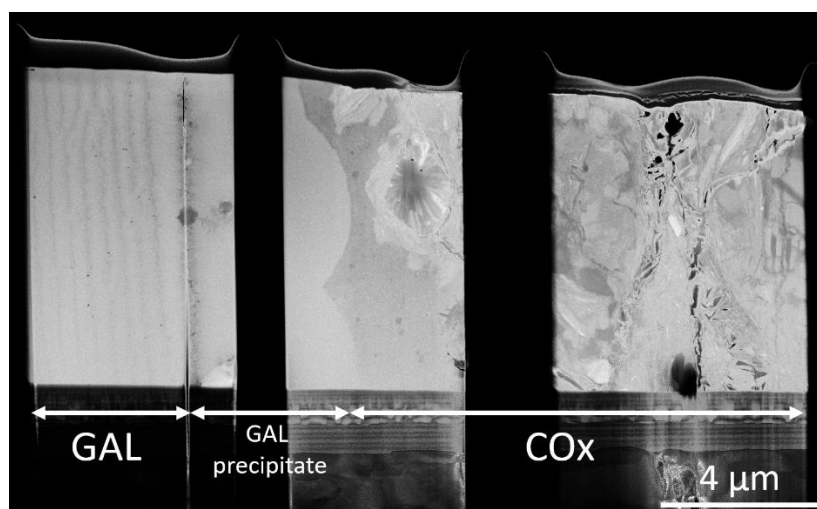


Figure 2-7 – FIB thin foil of the GAL after the 6.1 years

2.4.3.5 HRTEM characterizations in the GAL

HRTEM characterizations were performed to determine the inter-reticular distance of the iron phyllosilicates in the GAL and GAL precipitate. On the 2.5 years sample, the 10.4 Å distance is compatible with non-hydrated smectite phase (Carriere et al., 2021). After 6.1 years of alteration, the 7.8 Å-phases in the GAL can be assimilated to serpentine. Same distances are measured in the GAL precipitate (7.9 Å).

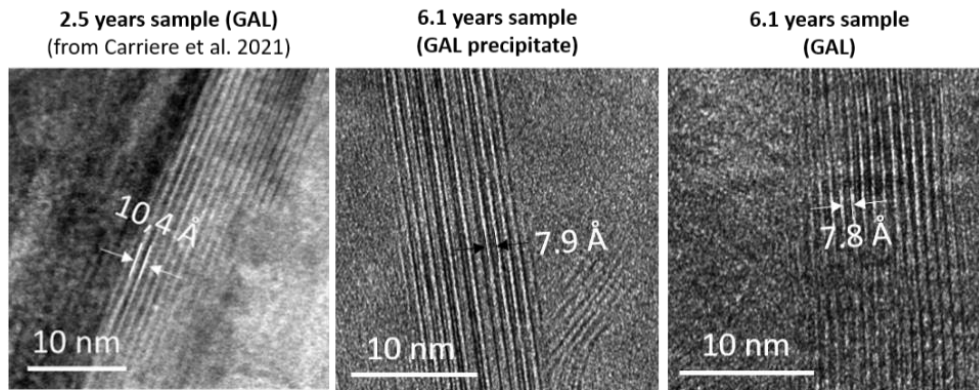


Figure 2-8 – HRTEM characterizations of the GAL iron phyllosilicates

2.4.3.6 STXM characterizations in the GAL

STXM measurements were carried out at CLS (Canadian Light Source) on SM beamline. This synchrotron radiation based technique at the Fe L-edge (Figure 2-9) is a useful tool to determine the valence of Fe, using reference spectra of iron oxide (siderite and maghemite) (Bourdelle et al., 2013). In addition, STXM analysis at the Si K-edge (Figure 2-10) is sensitive to the chemical environment of the Si, up to 5 Å or 6 Å distance (Carrière et al. 2021). The comparison of reference phyllosilicates spectra with spectra obtained in the region of interest allows phyllosilicates identification (Carriere et al., 2019).

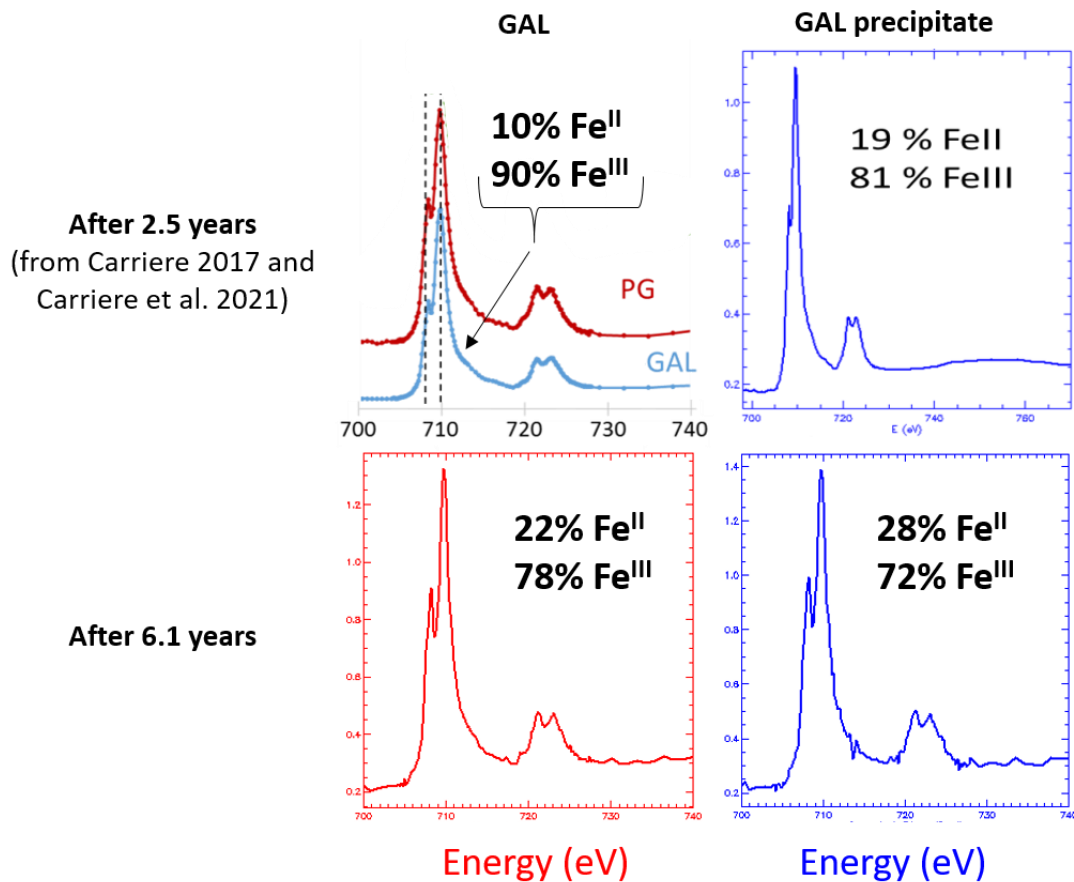


Figure 2-9 – STXM Fe L-edge spectra in the GAL and GAL precipitate

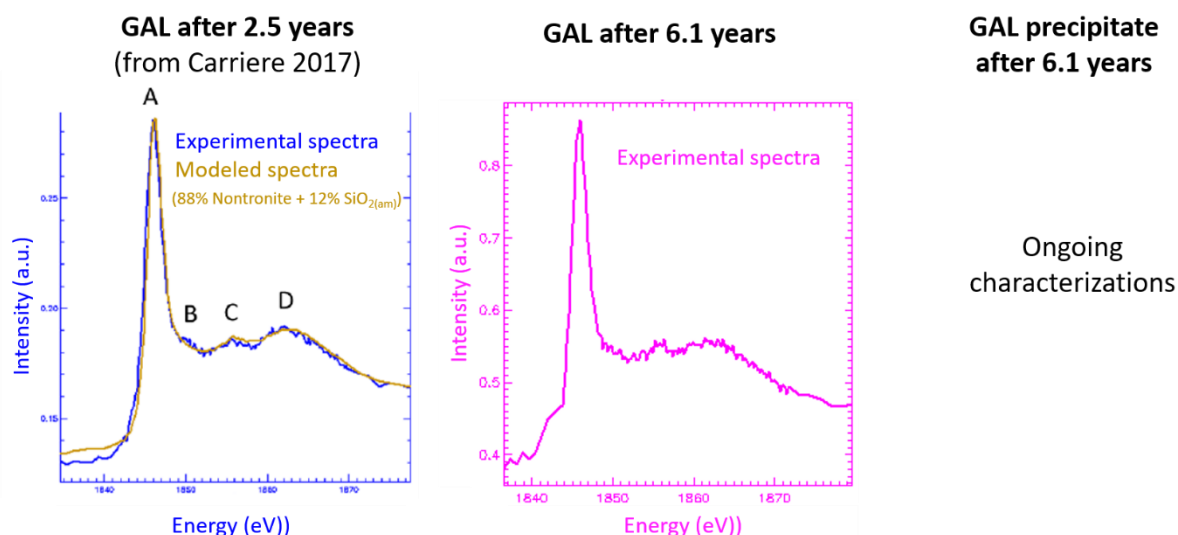


Figure 2-10 – STXM spectra at Si K-edge in the GAL and GAL precipitate

After 2.5 years of alteration, phyllosilicates in the GAL are mainly Fe^{III}-phases (90% Fe^{III} and 10% Fe^{II}), according to the fit of STXM spectra at Fe L-edge. Analysis at Si K-edge suggest that the GAL and GAL precipitate is composed of nontronite, a Fe^{III}-smectite, and a few SiO_{2(am)} (Carriere et al., 2021).

A Fe valence change is observed after 6.1 years: 72% Fe^{III} and 78% Fe^{III}, in the GAL and GAL precipitate, respectively. STXM at Si K-edge are not analyzed yet¹. Nevertheless, HRTEM measurements indicate iron phyllosilicates could be 7.8Å-phase (serpentine like phase) even though STXM spectra looks the same.

Lantenais et al. (2005) reported that dioctahedral Fe³⁺-rich smectite are destabilized in alkaline conditions for the benefit of 1:1 phyllosilicates (odinite and crondstedtite). The Fe valence change and inter-reticular distance evolution are indications in agreement with this transformation.

2.4.3.7 LA-ICP-MS in the COx at the glass/COx interface, Isotopic Analysis

As SON68 glass is doped (50% in ²⁹Si and 100% in ⁵⁷Fe), LA-ICP-MS (collaboration with Subatech laboratory (Nantes, France)) was used to determine the migration of ²⁹Si into the COx cylinder in the 6.1 years old sample. In order to investigate the ²⁹Si/ΣSi ratio, the laser dug circular spots (diameter ≈ 30 μm) in the COx at different distances from the glass surface. The vaporized excavated claystone was analysed by ICP-MS. The results, presented in Figure 2-11, show a ²⁹Si enrichment at the glass surface up to a distance of 50 μm. This result suggests that ²⁹Si from the glass remains in the vicinity of the glass. Beyond 50 μm of the glass, Si isotopes corresponds to the natural abundance. Note that the 30 μm laser spot does not allow precise analysis at the glass/COx interface, as its spatial size is higher than the GAL thickness. ToF-SIMS results are presented below in the GAL and ICP (Table 2-7).

Other elements are more mobile into the COx (Figure 2-16): Mo enrichment was detected in the COx up to 400 μm distance from the glass, while most of the elements migration does not exceed 200 μm (Nd, La, Zr, Li, Zn).

¹ These results will be published in Alexis Delanoë's thesis in 2023 and future papers.

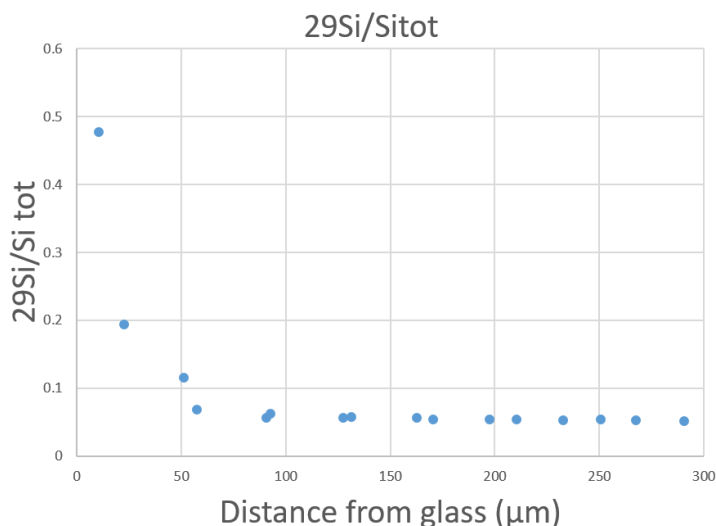
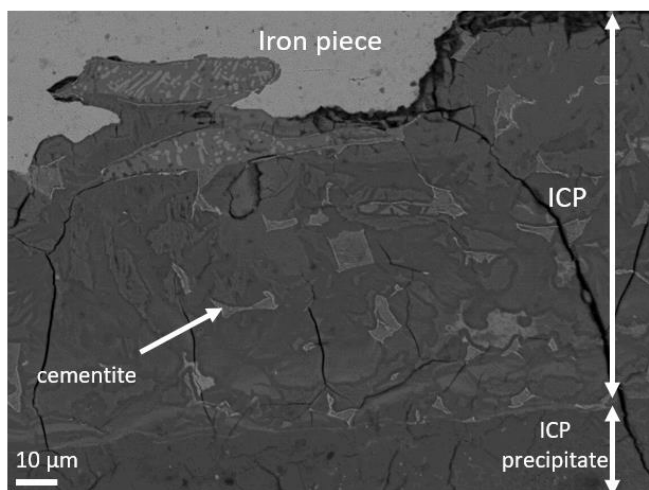


Figure 2-11 – Isotopic ^{29}Si enrichment in the COx at the glass/COx interface after 6.1 years

2.4.3.8 SEM-EDX characterizations in the ICP

On the backscattered electron image (Figure 2-12), white aggregates are observed within the corroded layer. These phases are iron slag or cementite phases (Fe_3C) which are components of the pristine steel. The presence of these phases allows us to determine the initial surface of the steel coupon (repolished archaeological nail). Further we note iron corrosion products (ICP) the phase formed beneath the initial surface of the coupon, and ICP precipitates the phases formed on the top of the initial surface of the coupon (Figure 2-5 after 6.1 years, and Figure 2-12).

Backscattered electron micrograph of ICP after 6.1 years



SEM-EDX micrograph of ICP after 6.1 years

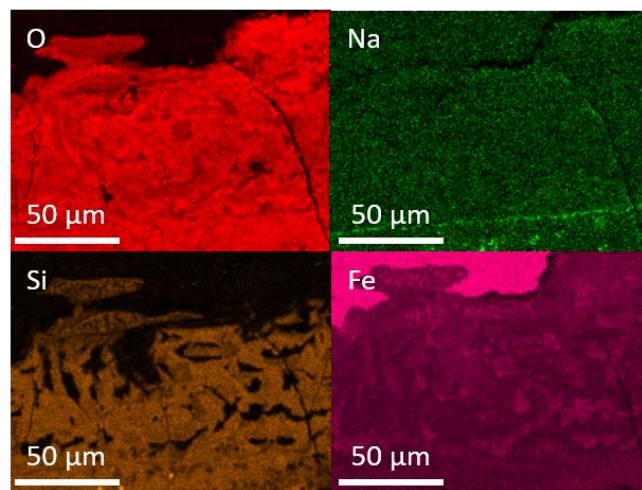


Figure 2-12 – ICP after 6.1 years: backscattered micrograph (left) and SEM-EDX micrographs (right)

Table 2-6 – SEM-EDX composition in the Si-free ICP and ICP with Si in wt. %

	After 2.5 years	After 6.1 years

	(Carriere et al. 2021)				
	Si-free ICP	ICP needle shape	ICP with Si	Si-free ICP	ICP with Si
Fe	54	63	47	65	45
O	33	32	33	35	38
Si	n.d.	4	18	n.d.	17
Ca	13	1	1	n.d.	n.d.
Na	n.d.	n.d.	1	n.d.	n.d.

According to the SEM analyses, ICP thickness ranges from 5 μm to 120 μm . Precise measurements are presented in Table 2-4. Two kinds of ICP are identified in the two mock-ups: (1) Si-free ICP and (2) Si-containing ICP. The Si-containing ICP are evidenced on the Si micrograph in Figure 2-12, and are composed of Si, O and Fe which is characteristic of iron silicates. No HRTEM inter-reticular measurement was performed due to the low crystallinity of iron silicates. On the same micrograph, the top right corner is a Si-free area: these Fe-O phases are iron carbonates and were identified by Raman spectroscopy (chukanovite). Siderite was observed, too.

ICP precipitate thickness ranges from 25 to 40 μm after 6.1 years. These phases were not reported in the 2.5 years mockup. According to SEM-EDX analysis, only iron silicates were identified in this precipitate (Figure 2-6 after 6.1 years).

SEM-EDX analysis on the 6.1 years sample evidenced a nanometric Na layer at the ICP/ICP precipitate interface (Figure 2-12, right), as was already observed at the GAL/GAL precipitate interface. Formation mechanism needs further investigation, but Na from the synthetic pore water could have reacted with the iron and glass surfaces at the beginning of the experiment to create this thin layer. Note that $K_{\alpha}(\text{Na})$ and $L_{\alpha}(\text{Zn})$ peaks overlap on EDX spectra. Further investigations needs to be performed to certify the presence of Na, and the absence of Zn.

A Fe^{III} -rich 1 μm -thick layer was detected at the iron/ICP interface (Figure 2-12). It could be magnetite (Fe_3O_4), maghemite ($\gamma\text{-Fe}_2\text{O}_3$) or maghemite/magnetite spinel phase as observed in previous experiments (Leon et al., 2017; Michelin et al., 2013).

2.4.3.9 Raman spectroscopy in ICP

Raman spectroscopy inside Si-free ICP evidenced the presence of chukanovite ($\text{Fe}_2(\text{CO}_3)(\text{OH})_2$) and siderite (FeCO_3) after 2.5 years (Carriere et al., 2021) and 6.1 years (results not shown here). Such phases were already reported in literature during iron corrosion experiments in anoxic and carbonated environment (Leon et al., 2017; Michelin et al., 2013; Saheb et al., 2010). The identification of iron silicates using 532 nm laser was not successful, as iron phyllosilicates are difficult to characterize with Raman spectroscopy (Gates et al., 2017; Wang et al., 2015).

2.4.3.10 STXM in the ICP

Due to their low crystallinity, inter-reticular distance of Si-containing ICP were not determined by HRTEM. STXM spectra suggest that Fe^{III} -rich nontronite were formed after 2.5 years in the ICP (78% Fe^{III} , Figure 2-13 and Figure 2-14). As a reminder, the same phase was observed in the GAL, nevertheless ICP are deprived of $\text{SiO}_{2(\text{am})}$. The 3% of $\text{SiO}_{2(\text{am})}$ suggested by the modelled spectra might have been generated during FIB thin foil preparation, as beam can induce amorphization of the thin foil. After 6.1 years of alteration, ICP silicates valence remains constant (83% Fe^{III}) but the nature of phyllosilicates was not determined yet.

STXM at Fe L-edge in carbonate indicates that carbonates phases are 1/3 Fe^{III} . Analysis of the 1 μm thick iron/ICP interfacial layer indicates is Fe^{III} -rich phase.

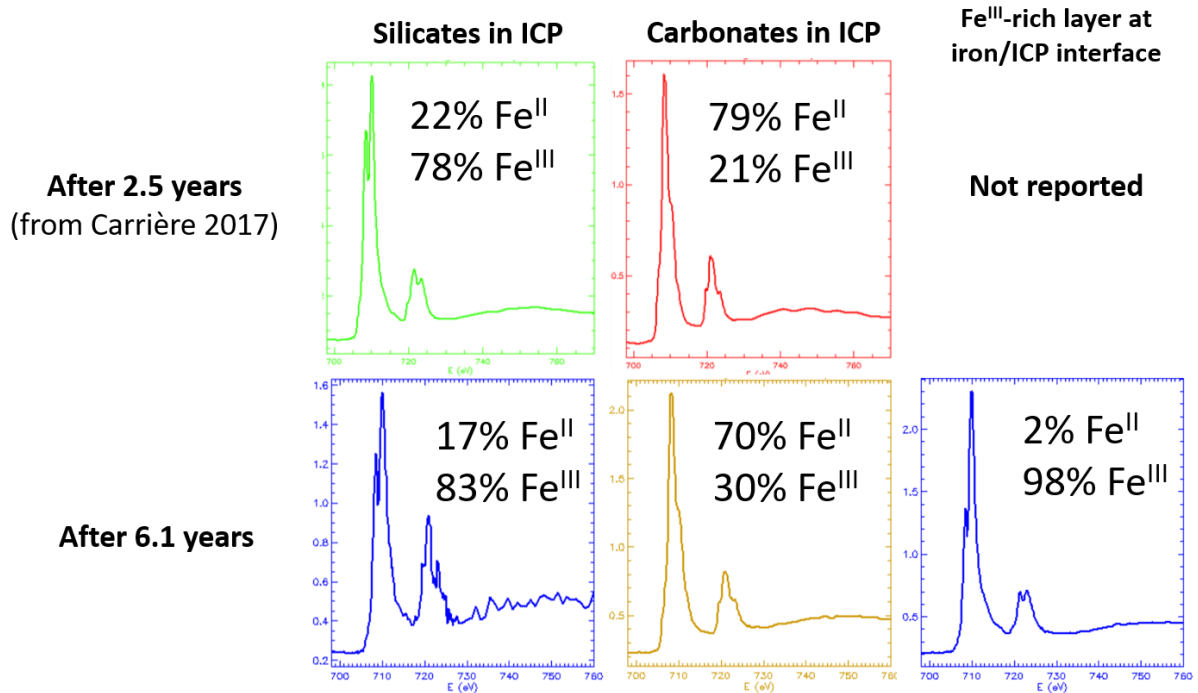


Figure 2-13 – STXM spectra at Fe L-edge in ICP

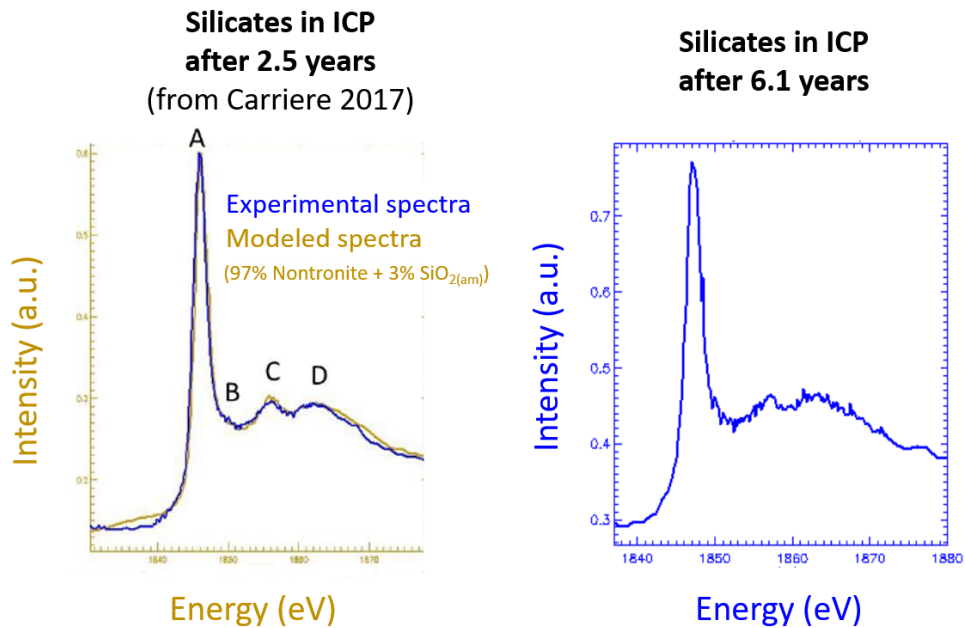


Figure 2-14 – STXM spectra at Si K-edge in ICP silicates

2.4.3.11 ToF-SIMS analysis: the fate of Si and Fe

As the glass was doped with ²⁹Si and ⁵⁷Fe, ToF-SIMS analysis provided Si and Fe enrichment in the PG, GAL, and ICP with Si. The fate of Si in the mock-up can be estimated with a system of equations described in Carrière et al. (2021). The calculation in the GAL indicated that:

- **after 2.5 years:**

- 32% of Si in the GAL comes from glass alteration (and thus 68% comes from the solution)
- **after 6.1 years:**
 - 41% of Si in the GAL comes from glass alteration (and thus 58% comes from the solution)
 - 25% of Si in the GAL precipitate come from glass alteration (and thus 75% come from the solution)

Similar calculation in the ICP with Si shows that:

- 19% of Si in ICP with Si comes from glass alteration after 2.5 and 6.1 years (and thus 81% comes from the solution)

The fate of Fe in the mock-up indicates that 91% or 92% of Fe is ⁵⁶Fe in the GAL, GAL precipitate or ICP with Si. It means that the main provider of Fe is the corrosion of iron piece, as the glass iron content is very low.

Table 2-7 – Si and Fe enrichment determined by Tof-SIMS

Isotope content	After 2.5 years (from Carriere et al. 2021)			After 6.1 years			
	PG	GAL	ICP with Si	PG	GAL	GAL precipitate	ICP with Si
²⁸ Si ⁺ /∑Si	45	78	78	44	72	80	81
²⁹ Si ⁺ /∑Si	52	20	19	54	25	17	17
³⁰ Si ⁺ /∑Si	3	2	3	2	3	3	2
⁵⁴ Fe ⁺ /∑Fe ⁺	1	6	5	1	6	6	6
⁵⁶ Fe ⁺ /∑Fe ⁺	3	91	92	5	91	91	91
⁵⁷ Fe ⁺ /∑Fe ⁺	96	3	3	94	3	3	3

2.5 Analysis of the leaching solution

An attempt was performed to extract the pore water from the COx claystone of the 6.1 years aged mock-up. Synthetic deuterated pore water (with iodine tracer) was prepared and injected in the mock-up to flush out the pore water from the claystone (Figure 2-15). The collected pore water was analysed with ICP-MS and ICP-AES. The results are not presented here as they are not considered as reliable, as it is suspected that the injected water followed preferential pathways within the mock-up.

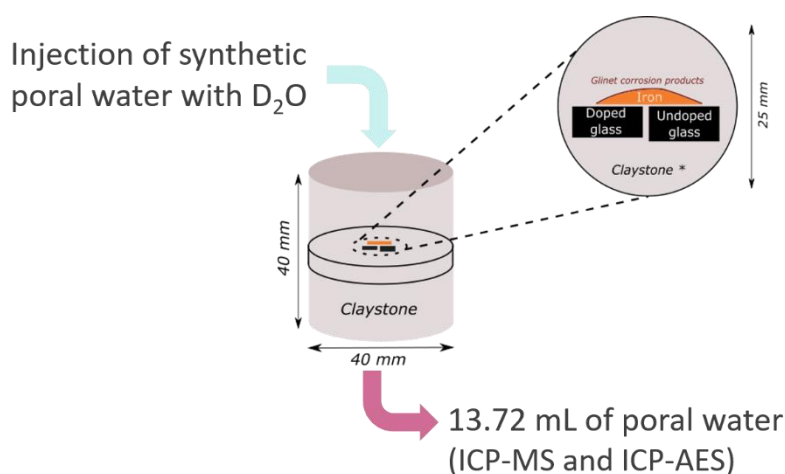


Figure 2-15 – Schematic representation of the pore water collection

2.6 Other tests and characterization

The 6.1 years aged mock-up was investigated using LA-ICP-MS (collaboration with Subatech) to investigate the migration of glass elements into the COx. Figure 2-16 to Figure 2-18 present these results as complementary information. It appears that Zr, Nd, Zn, La, which mostly come from the glass diffuse beyond the GAL, up to 200 μm from the glass. Moreover one can note that Mo, also a glass element diffuses further, up to 400 μm from the glass. The behaviour of the other elements is not easy to interpret as they come from various sources.

2.6.1 LA-ICP-MS in the COx, Elementary Analysis

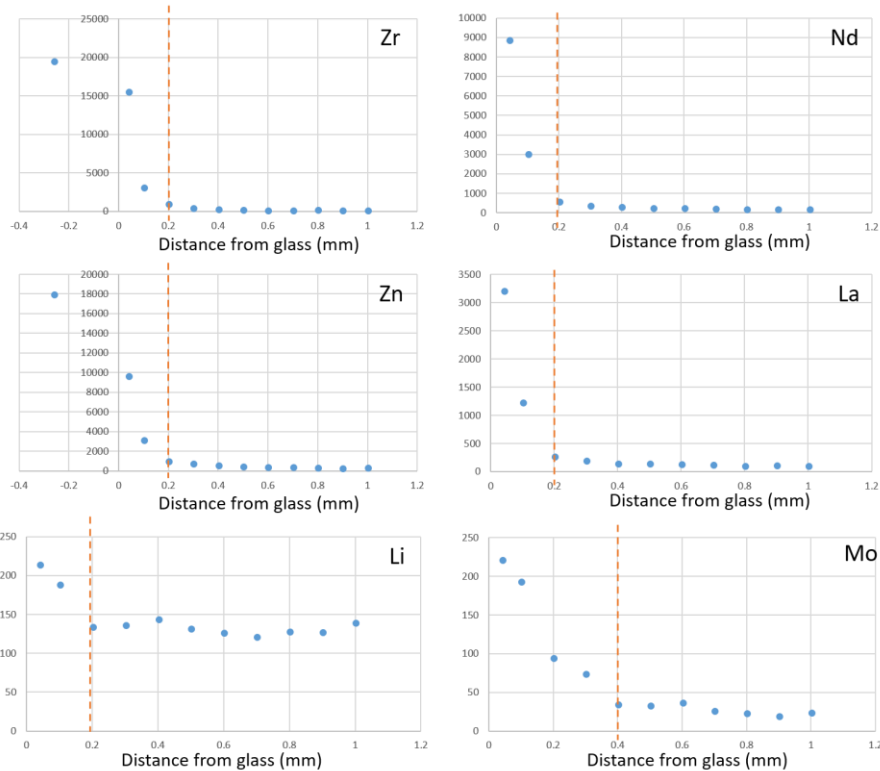


Figure 2-16 – LA-ICP-MS characterizations at the glass/COx interface for Zr, Nd, Zn, La, Li and Mo

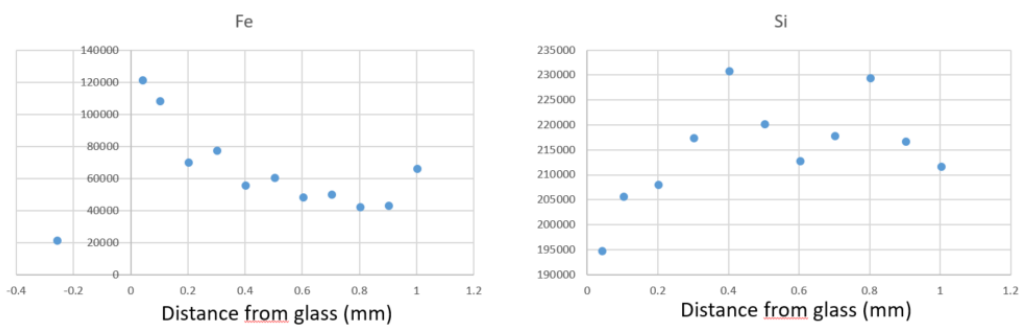


Figure 2-17 – LA-ICP-MS characterizations at the glass/COx interface for Fe and Si

EURAD Deliverable D2.12 – High level radioactive waste package – Characterization of glass/steel/buffer interaction experiments

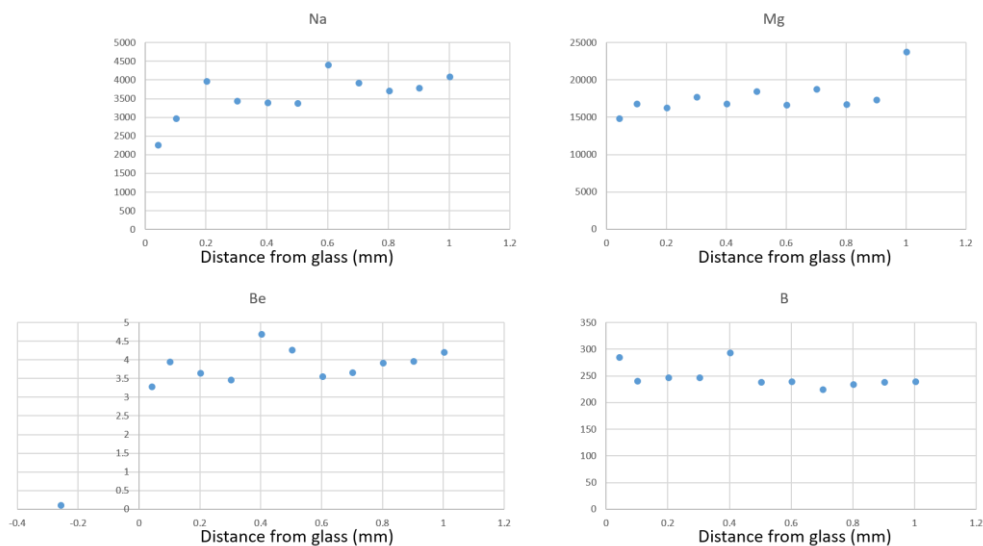


Figure 2-18 – LA-ICP-MS characterizations at the glass/CO_x interface for Na, Mg, Be and B

3 Experiment 2: Glass/Steel/Clay system, 80°C

3.1 Background

Partner: MTA EK

Contact person: M. Fabian

The aim of this work was to conduct a limited series of specific experiments to study the chemical evolution of a borosilicate glass/steel/Boda claystone system for conditions similar to those can be found in a deep geological repository (temperature, groundwater) and compare it with other characteristic systems.

Long-term exposure to repository-like conditions could result in significant alterations in materials during their service life. The repository's host media can be a source of oxygen, ions, and other species that can be aggressive towards the materials used for waste containment. Due to these stresses, various forms of degradation can be expected.

We built a scale model system where conditions were as close as possible to the real conditions. The main goal was to understand the characteristics, applicability and stability of the whole system, from the structural properties of the vitrified waste (in borosilicate glasses) to the clay response in the repository.

3.2 Description

The glass/steel/clay system in the experimental setup was kept at 80°C. After 3, 7 and 12 months, the containers were removed, and in all three cases, the 'samples' were fully saturated with porewater.

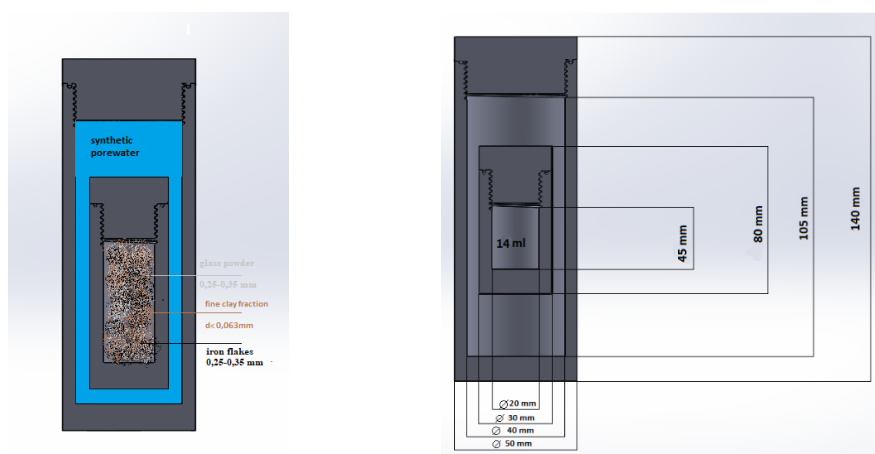


Figure 3-1 – Schematic view (gray areas: internal and external Teflon vessel, blue area: synthetic pore water, brown area (middle) clay-iron-glass mixture) and physical dimensions of the experiments.

We completed three glass/steel/clay experiment set-up using synthetic Boda pore water (SBPW) for saturation. Double Teflon containers were built (Figure 3-1): an internal vessel containing the mixture of 1.4 g of powdered glass (borosilicate powder, 50-86 μm , 0.083 m^2 surface area), 0.7 g of steel (Fe powder, 50-86 μm , 0.008 m^2 surface area) and 27.9 g of claystone (crushed Boda claystone, <100 μm fraction), and an external vessel containing the internal vessel surrounded by 75.36 ml of SBPW. During the experiments, the shape of the glass grains was assumed to be cubic, so that the calculated SA/V was 1108 m^{-1} . The system is static which means that the porewater is only introduced at the start of the

experiment. To ensure the saturation of the studied media, holes were drilled on the wall of the internal vessels. All containers were filled with the same glass/Fe/Boda clay mixture and kept in an incubator at 80 °C. After 3, 7 and 12 months (M) a container, named as respectively, 3M, 7M and 12M throughout this report, was opened and were polished before characterization. A portion of the initial media was preserved and kept dry for reference.



Figure 3-2 - Experimental setup of the glass/steel/clay systems.

3.3 Materials involved: Chemical composition

3.3.1 Glass - borosilicate glass

The composition of the glass specimen was 55%SiO₂-10%B₂O₃-25%Na₂O-5%BaO-5%ZrO₂, the density was 2.67 g/cm³. The sample has been prepared by a conventional melt-quench technique using a high temperature electrical furnace with a platinum crucible under atmospheric conditions. We have performed a neutron- and X-ray diffraction structure study on borosilicate glasses. Several first neighbour distances were determined from the total distribution function due to the high r-space resolution. These input data were applied for Reverse Monte Carlo simulation. The most important partial distribution functions have been revealed including the first neighbour distances and coordination numbers. We concluded that the Si–O network consisting of tetrahedral SiO₄ units is highly stable, even in the multicomponent glasses. The B–O correlations show two distinct distances at 1.40 and 1.60 Å. These findings are consistent with a structure model where a part of boron atoms form a mixed continuous network with several different ^[4]B–O–Si^[4] and ^[3]B–O–Si^[4] linkages (Fábián et al., 2007). We have prepared and performed neutron- and high-energy X-ray diffraction measurements on borosilicate host glass (55%SiO₂-10%B₂O₃-25%Na₂O-5%BaO-5%ZrO₂) loaded with 30 wt% UO₃ in order to get structural information on the basic network structure and on the uranium surroundings. The diffraction datasets were simulated by Reverse Monte Carlo (RMC) modelling to obtain a possible three-dimensional atomic configuration. It was established that the basic network structure consists of tetrahedral SiO₄ units and of mixed tetrahedral BO₄ and trigonal BO₃ units, being rather similar to the network structure of the corresponding host glass as reported in our previous study (Fábián et al., 2007). Slight changes, however, have been observed in the oxygen surroundings of the Na and Zr cation modifier ions. Both the Na–O and Zr–O distances decrease, and a more compact short-range structure has been obtained compared to the host glass. For the U–O correlations two distinct peaks were resolved at 1.84 and 2.24 Å, and for higher distances well-pronounced correlations are present at ~4.3 Å and at ~6.4 Å. Furthermore, significant atomic pair correlations have been revealed between uranium and the network former Si and B atoms centred at 3.4 Å and 3 Å, respectively. From these observations we concluded that uranium ions take part in the network forming. This may be the reason for the observed good glassy stability and hydrolytic properties (Fábián et al., 2010; Fábián et al., 2013). Based on these results we have recommended to use this matrix glassy composition in the glass/steel/clay experiments.

3.3.2 Steel: Fe powder (99%, from Acros Organics, CAS Nr. 7439-89-6)

Purchased Fe flakes were sieved on a laboratory cascade sieve and particle diameter (d_p) of 50-86 μm fraction was applied for the experiment. This size range was selected so that all 3 component's size are commensurable.

3.3.3 Clay: crushed claystone from Boda Claystone Formation (BCF)

The Boda Block of the BCF forms an anticline structure. The axis of the anticline plunges to the east, therefore the Boda Claystone has been eroded in the west. It crops out around the village of Boda. Its depth increases towards the north, east and south. The northern and eastern limits of its distribution are unknown.

In this block the maximum thickness of the BCF varies between 700-1000 meters in the central region. This thickness gives considerable flexibility when seeking the optimal site for a repository. During the sedimentation, the catagenetic stage was finally reached under high temperature (200-250 °C) and pressure (120-150 MPa). BCF beds were covered by sediments of up to 3.5-4.5 km thickness. The over consolidated, highly indurated character of BCF is a result of this situation.

Based on mineralogical investigations (XRD, DTA, EPMA), main minerals of the BCF are clay minerals (absolute dominant are illite-muscovite and chlorite; smectite, kaolinite, vermiculite and mixed-layer clay minerals were identified in inconsiderable amounts), authigenic albite, quartz, carbonate minerals (calcite and dolomite) and hematite. In addition, barite, anhydrite, authigenic K-feldspar and detrital constituents (muscovite, biotite, chlorite, zircon, rutile, apatite, ilmenite, Ca-bearing plagioclase, K-feldspar) were also identified in trace amounts. The authigenic albite is present as albite cement (typical of all rock types of the formation), albite and carbonate-lined disseminated irregular white voids (typical of albitic claystone) and albite replacement of detrital feldspars in sandstone beds. Six main rock types of BCF can be defined based on mineralogical, geochemical, and textural considerations: albitic claystone, albitolite, „true” siltstone, dolomite interbeddings, sandstone and conglomerate (Table 3-1).

Table 3-1 – Mineral composition of the rock types.

Rock types	clay minerals (wt %)	authigenic albite (wt %)	quartz (wt %)	carbonates (wt %)	hematite (wt %)
albitic claystone	20-50	20-50	5-10	~10	7-10
albitolite	<25	>50	<10	10	5-6
„true” siltstone	approx. 10	>35	>25	approx. 10	5
dolomite interbeddings	10	30-40	5	35-50	5
sandstone	5-trace	25-40 (feldspar)	20-30	5-20	5-trace

This mineralogical composition is typical of a perianticlinal structure of the W Mecsek Mountains (Lázár et al. 2012). The absolute dominant rock type of the formation is albitic claystone. For this reason, a core section of albitic claystone was selected for the present study. During the experiments the crushed BCF claystone was steeped with synthetic pore water resulting in a saturation of 100%. The initial BCF porewater considered in the experiment was a modelled synthetic pore water.

The calculations of the Boda porewater chemistries were performed with the geochemical speciation code MINSORB and the Nagra/PSI 01/01 thermodynamic database (Bradbury and Baeyens, 1997a; Bradbury and Baeyens, 1997b). The chemical composition of the Boda porewater was calculated at fixed $p\text{CO}_2$ ($= 10^{-3.5}$ bar) and fixed pH ($= 8.0$) i.e., in equilibrium with atmospheric $p\text{CO}_2$, and under the constraint of calcite, dolomite and quartz saturation (Lázár et al., 2012). Na^+ or Cl^- concentration was then adjusted to maintain charge neutrality, while Ca, Mg, Si and C(IV) concentrations were defined by the above constrains. The modelled Boda porewater composition is given in Table 3-2.

Table 3-2 – The chemical composition of synthetic pore water (SBPW).

Element	mol/L
Na	1.7×10^{-2}
K	1.8×10^{-4}
Mg	2.3×10^{-3}
Ca	3.1×10^{-3}
Sr	1.5×10^{-5}
Cl	2.3×10^{-2}
SO ₄	1.9×10^{-3}
HCO ₃ ⁻ /CO ₃ ²⁻	6.1×10^{-4}
Ionic strength	3.3×10^{-2}
pH	8.1
I(M)	0.02 M
Eh	-300 mV

3.4 Solid or interface characterization

3.4.1 Laboratory micro X-ray fluorescence (μ-XRF)

The applied voltage and current to the Rh-anode X-ray tube were 50 kV, 600 mA. The beam is focused to ~ 30 μm using a polycapillary. The spectrum were collected by a 10 mm² Ketek AXAS-D SDD (silicon drift detector).

The μ-XRF measurements were performed on pressed pellets of the studied mixture. The pellets were pressed with a 10-ton laboratory hydraulic press. No binder compound was needed since the mixture was wet while being pressed. The spatial resolution of the system was not fine enough for identifying newly formed phases. The measurements were performed before scanning electron microscopy (SEM) measurements to locate points where glass and iron flakes situated close on the pellet's surface.

Elemental maps show a 230(H)×280(V) μm² area scanned with 10 μm steps (maps are max/min normalized, the highest intensity is shown in white).

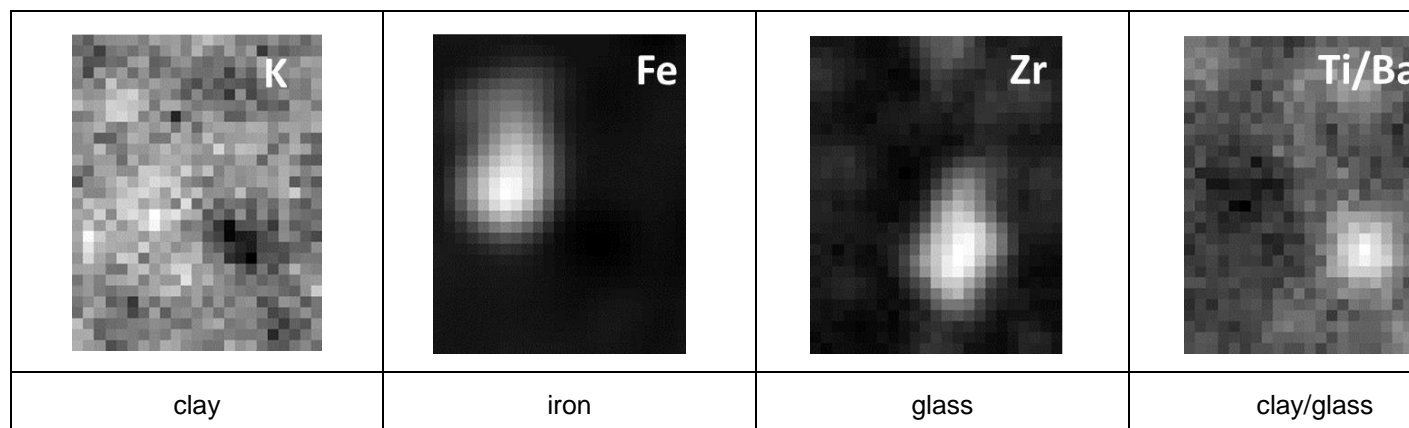


Figure 3-3 – Elemental maps of glass/Fe/clay sample after 3 months experiment

After 7 months the elemental maps show a 450(H)×450(V) μm² area scanned with 5 μm steps.

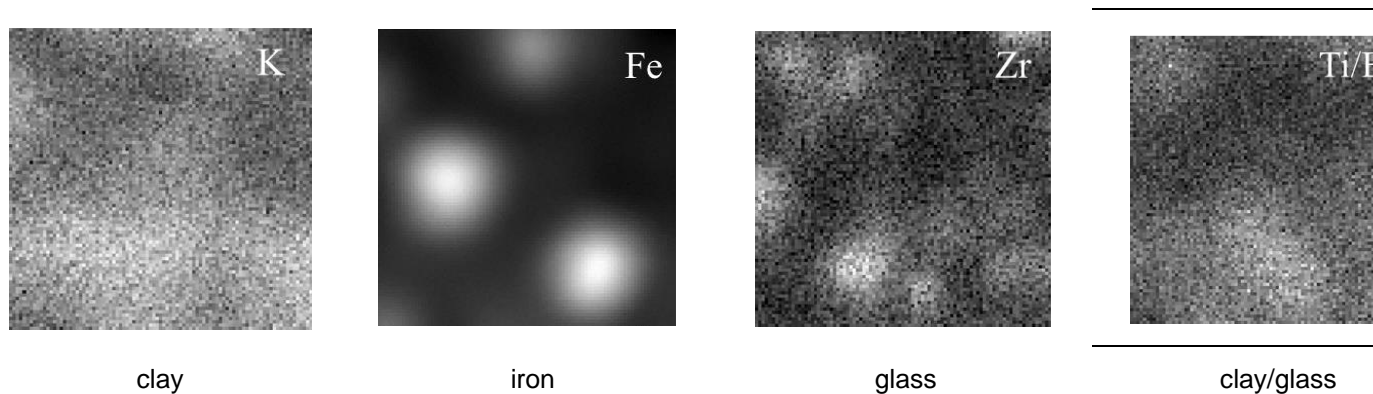


Figure 3-4 – Elemental maps of glass/Fe/clay sample after 7 months experiment.

After 12 months elemental maps show a 400(H)×400(V) μm² area scanned with 5 μm steps.

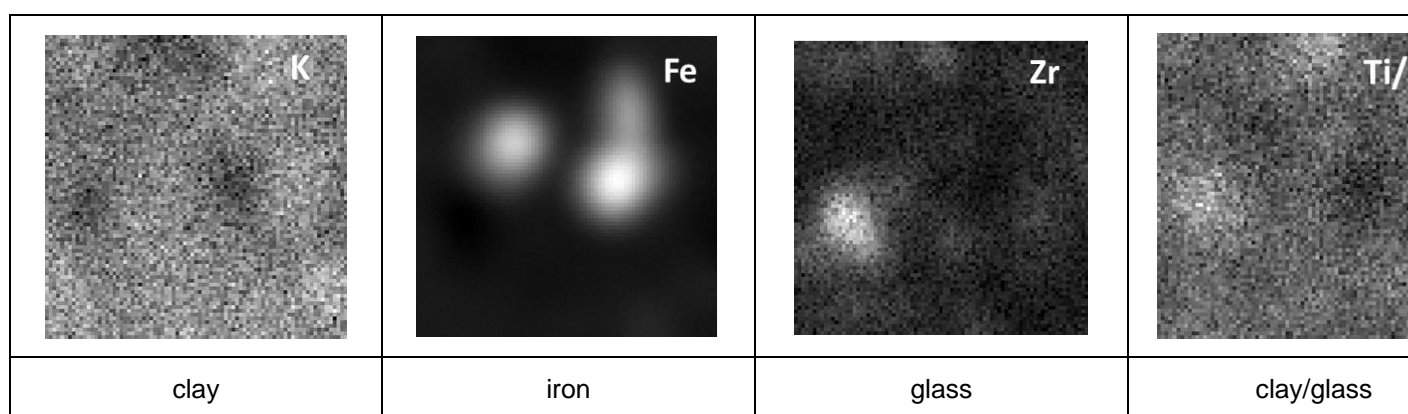


Figure 3-5 – Elemental maps of glass/Fe/clay sample after 12 months experiment

3.4.2 SEM and Energy Dispersive X-ray (EDX) spectrometry

On the solid sample SEM/EDX measurements were performed (20 kV, 1.6 nA) using a Thermo Scientific Scios2 dual beam microscope, Oxford X-max 20 SDD EDX. SEM investigations of all three polished glass/steel/clay samples revealed that the glass and steel grains were well isolated in the clay matrix.

With SEM/EDX investigations we focused on the composition and nature of alteration products formed on the borosilicate glass surface, on the Fe and within the clay. Here we present the SEM/EDX observations of the 3M, 7M and 12M samples. No alteration layer has been found on the borosilicate glass powder samples in any case within the resolution of backscattered electron imaging at 20 keV (~1 μm).

Detailed SEM/EDX results contain images and major elemental composition for selected positions are shown in Figure 3-6 and Table 3-3 after 3M, in Figure 3-7 and Table 3-4 after 7M and in Figure 3-10 and Table 3-5 after 12M. SEM/EDX elemental maps were also collected on the 7M samples at two areas, one of 150×50 μm² including all three types of materials (Figure 3-8) and a smaller area zoomed on Fe-clay boundaries (Figure 3-9).

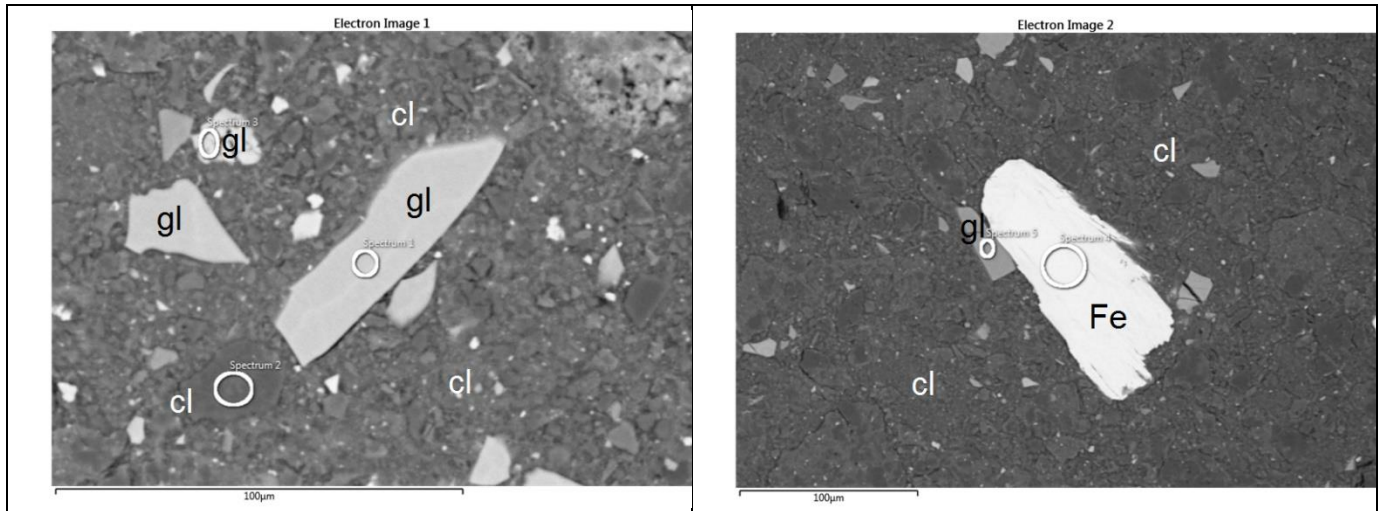


Figure 3-6 – SEM backscattered electron images on glass/Fe/clay sample after 3M treatment (solids of interest are marked as gl: glass, cl: clay and Fe)

Table 3-3 – SEM/EDX results: elemental composition after 3M (wt.%)

Elements	Spec1 (gl)	Spec2 (cl)	Spec3 (gl)	Spec4 (Fe)	Spec5 (gl)
O	43.89	50.18	44.82		43.27
Na	4.84	5.69	4.53		3.87
Mg		0.42			
Al		11.70	0.37		
Si	26.79	28.45	25.01		29.38
K		2.48	0.30		
Fe				100	0.67
Zr	8.15		9.23		7.57
Ba	16.33		15.73		15.24
Total	100	100	100	100	100

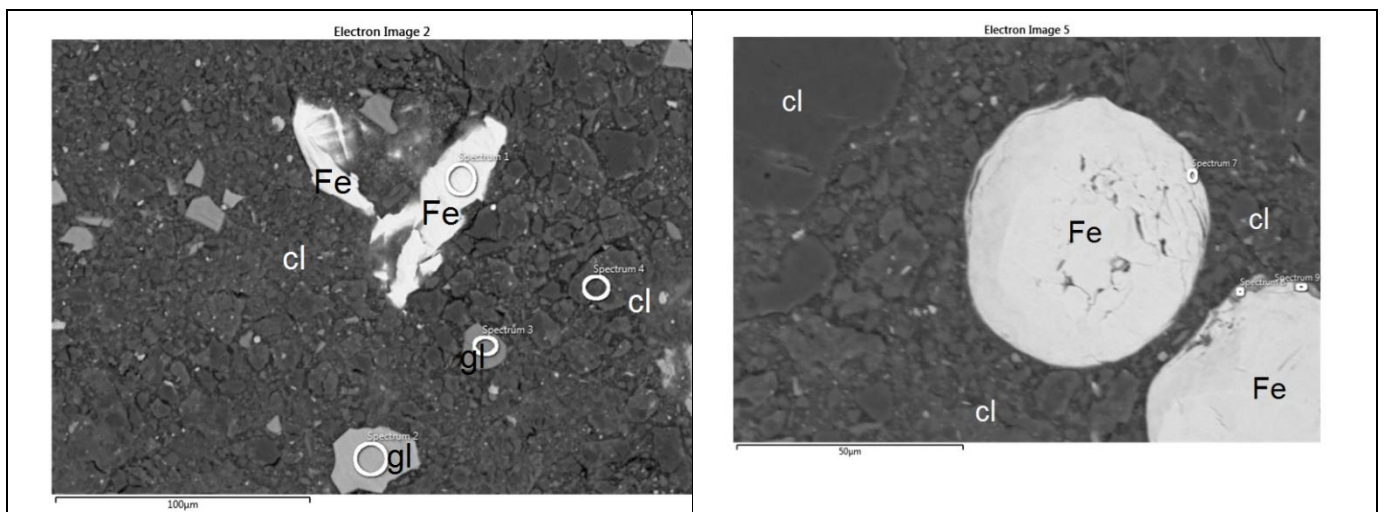
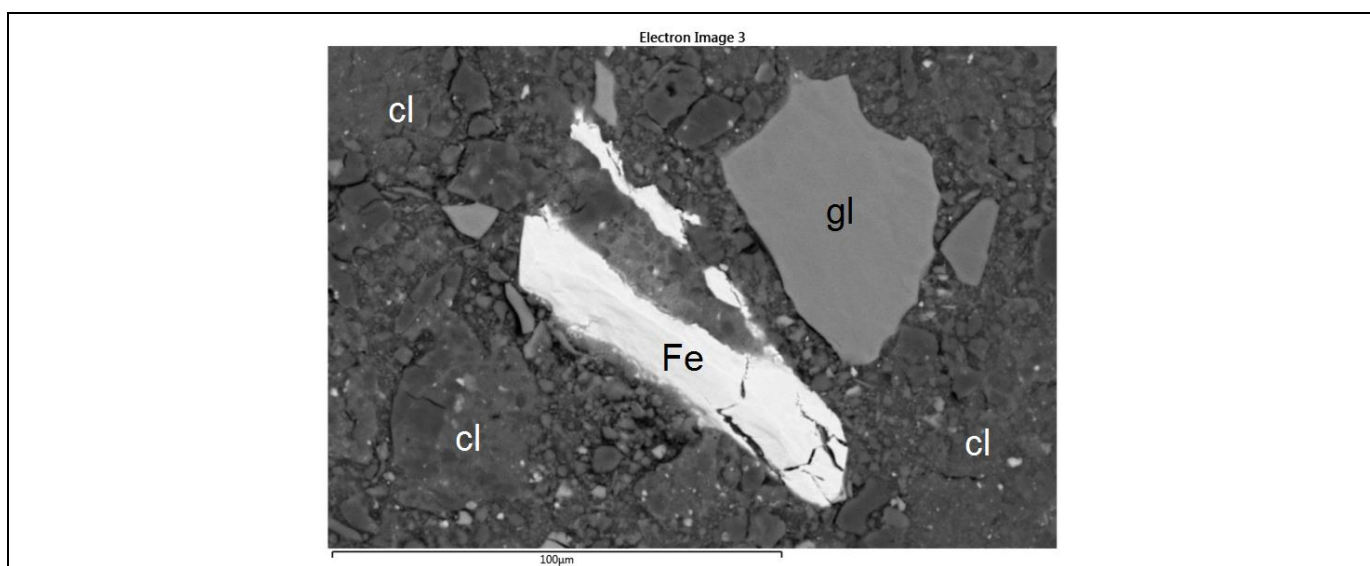


Figure 3-7 – SEM backscattered electron images on glass/Fe/clay sample after 7M treatment

Table 3-4 – SEM/EDX results: elemental composition after 7M (wt.%)

Elements	Spec1 (Fe)	Spec2 (gl)	Spec3 (gl)	Spec4 (cl)	Spec7 (Fe)	Spec8 (Fe*)	Spec9 (Fe)
O	0.44	38.02	43.63	44.66	1.26	29.12	5.82
Na		4.65	5.07	2.24			
Mg				1.96			
Al	0.02	0.03		9.21		3.74	0.40
Si	0.13	23.04	31.59	27.85	0.21	8.30	0.85
P				0.15			
K		2.48		4.21		0.69	
Ca						0.85	
Fe	99.39			6.59	98.53	57.30	92.93
Zr		9.35	7.17				
Ba		20.39	12.04				
N	0.02	0.14					
B		4.37					
Total	100	100	100	100	100	100	100

* Spectrum 8 shows that Fe and clay are simultaneously present at the measured position, no sign of Fe-oxide formation



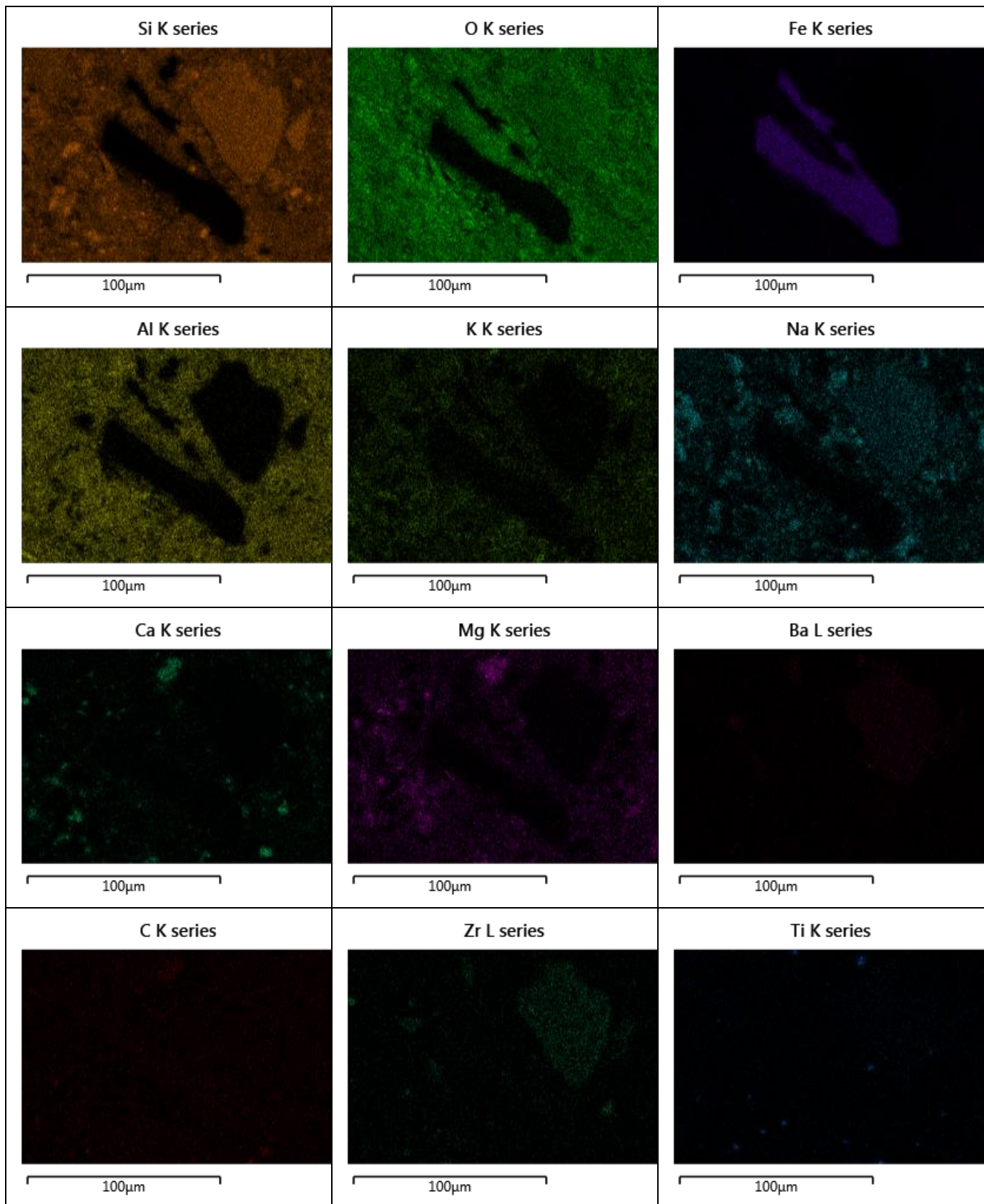


Figure 3-8 – SEM backscattered electron image and the corresponding EDX elemental maps on sample 7M

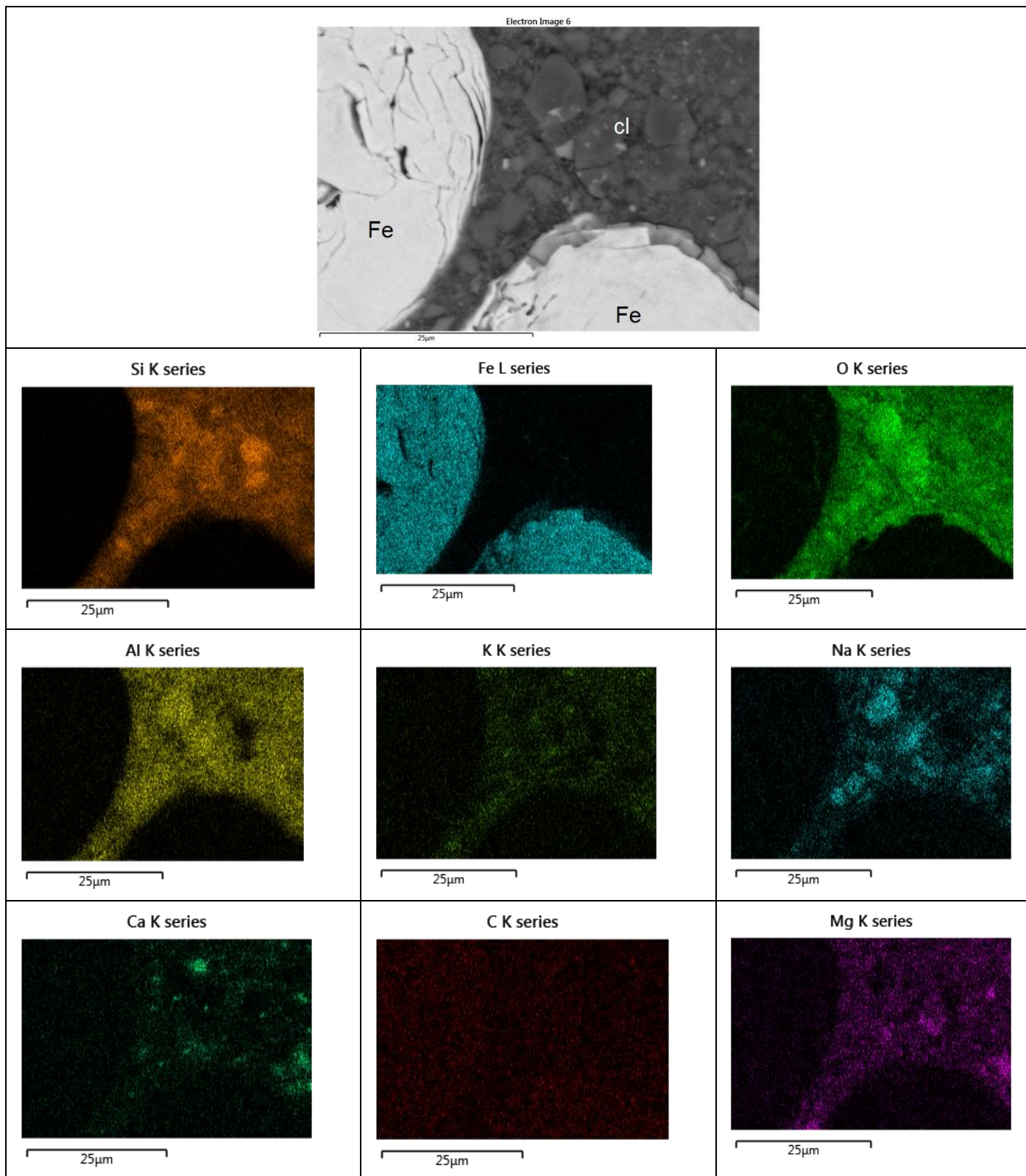


Figure 3-9 – SEM backscattered electron image and the corresponding EDX elemental maps on sample 7M

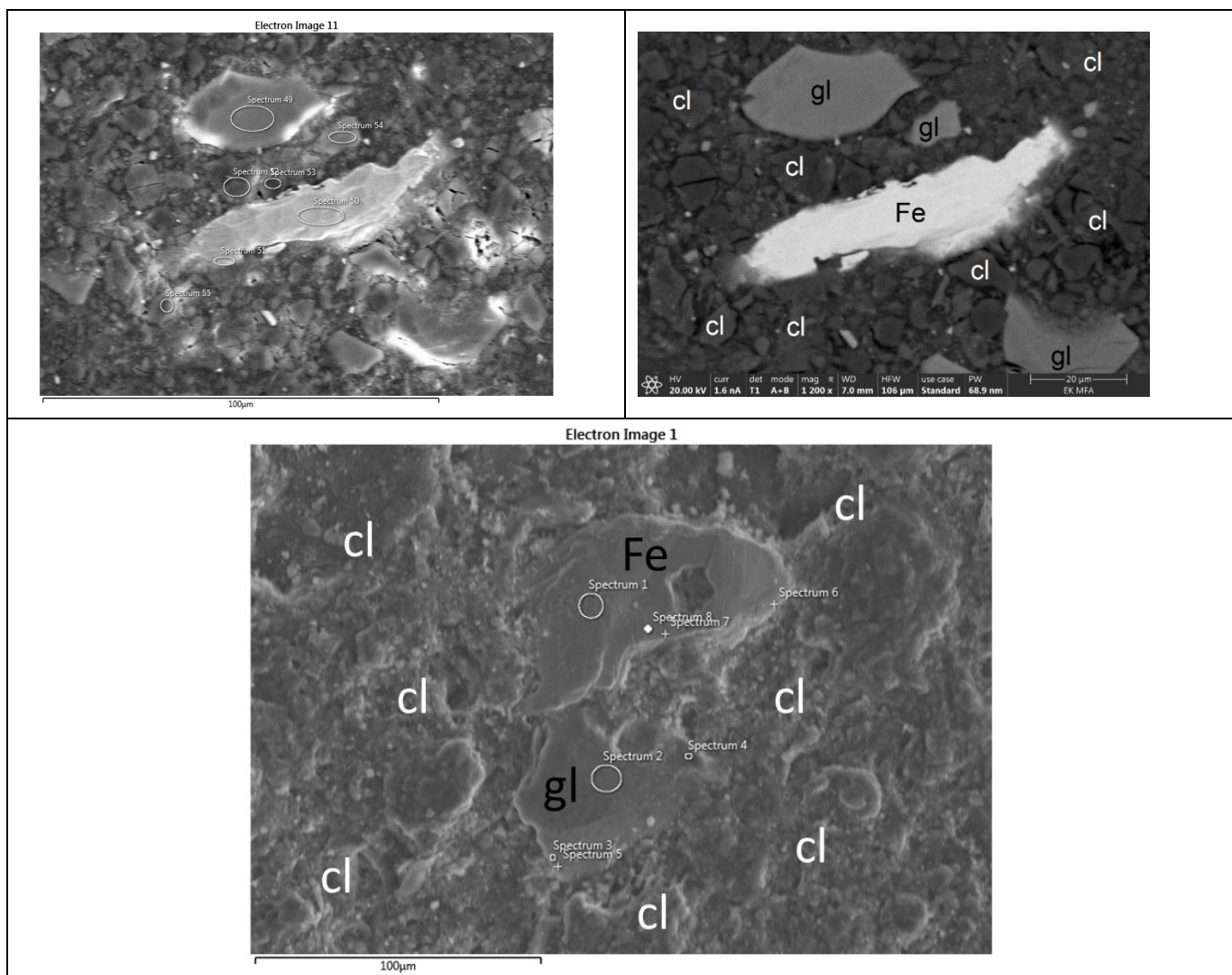


Figure 3-10 – SEM results after 12M, secondary (left, bottom) and backscattered electron image (right) of characteristic areas.

Table 3-5 – SEM/EDX results: elemental composition after 12M (wt.%)

Elements	Spec1 (Fe)	Spec2 (gl)	Spec3 (gl)	Spec4 (gl)	Spec5 (gl)	Spec6* (Fe/cl)	Spec7* (Fe/cl)	Spec8 (Fe)	Spec49 (gl)	Spec50 (Fe)	Spec51 (Fe/cl)	Spec52 (cl)	Spec53 (cl)	Spec54 (glass)	Spec55 (cl)
O	1.01	47.23	43.79	42.81	45.82	47.96	10.79		44.31		3.12	46.69	50.45	42.66	46.82
Na		5.87	4.21	3.55	3.39	2.57	0.82		5.02			5.21		4.59	1.65
Mg			0.21		0.25	2.41	1.01					0.76			
Al			0.72	0.74	1.10	7.90	3.26				1.12	9.23	0.63	0.62	10.06
Si		26.04	27.25	28.06	26.81	21.49	6.48		28.85		1.31	29.70	46.61	28.00	30.44
K			0.33	0.50	0.45	2.19	1.23				0.25	1.78	0.38	0.29	10.36
Ca			0.26	0.55	0.26	0.72	1.33					0.78	0.14	0.15	
Ti												0.34			
Fe	98.99		0.64	0.58	0.53	14.15	75.07	100	0.60	100	94.21	3.46	1.80	1.18	0.68
Rb												0.51		1.69	
Zr		8.41	8.90	10.12	8.38				8.45					8.27	
Ba		12.44	13.70	13.08	13.01	0.60			12.78					12.56	
Total	100	100	100	100	100	100	100	100	100	100	100	100	100	100	100

*Spectra 6,7 show that Fe and clay are simultaneously present at the measured position

In each sample, the three different types of materials could be identified separately. Along the glass, no significant change was detected on the surface and borders. The main elements contained in borosilicate glass are silicon, oxygen, sodium, zirconium, barium and all of them were identified after 3, 7 and 12 months experiments. No secondary phases were identified.

In the case of the glass, the results measured at the edges do not differ significantly from the composition of the bulk phase. In the case of edges positions of iron grains, clay is also present in the excitation volume of SEM/EDX. Similar as 7M, no significant iron oxide formation was detected.

The SEM images do not show alteration layer on the borosilicate glass powder samples in any case within the resolution of backscattered electron imaging at 20 keV (~1 μm). SEM/FIB investigations with higher lateral resolution were made in order to elucidate the influence of the presence of Fe or clay on the alteration layer thickness of the glass particles. All three solid components, the glass particles, the Fe, and clay it was not difficult to quantify.

Focused ion beam (FIB) is a technique used in the materials science for site-specific analysis. A FIB setup is a scientific instrument that resembles a scanning electron microscope (SEM). The SEM uses a focused beam of electrons to image the sample in the chamber.

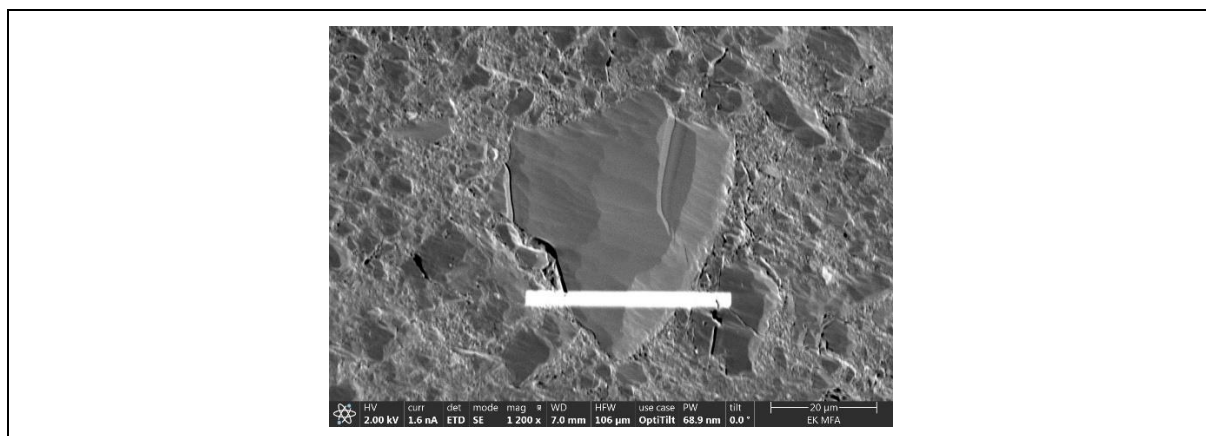
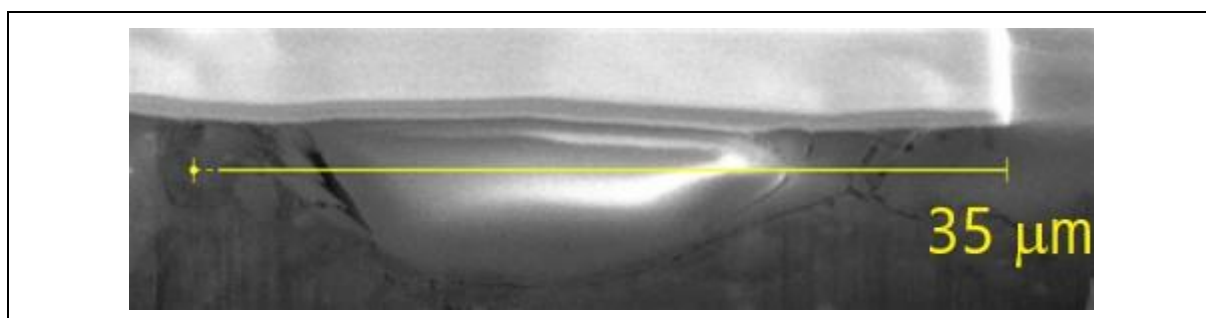


Figure 3-11 – SEM image of a focused ion-beam cross-section of the glass parts, on 7M sample.



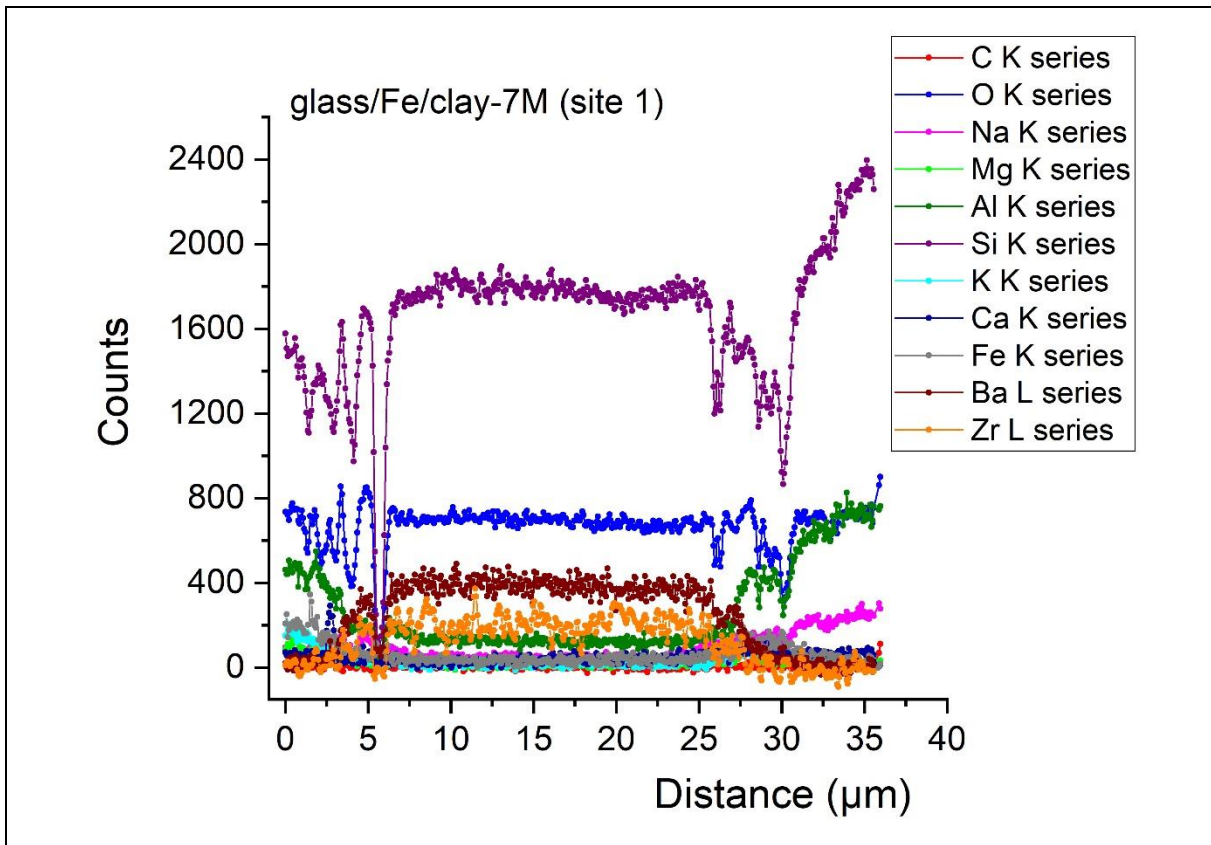
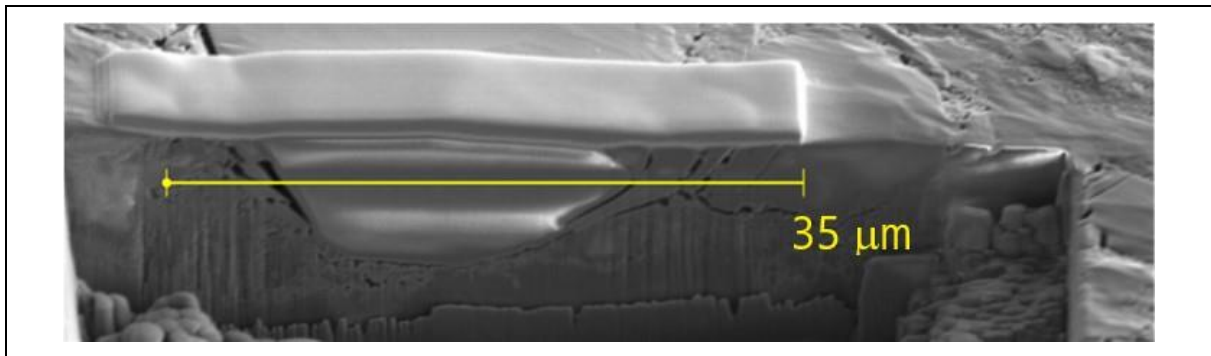


Figure 3-12 – SEM image (top) and the line profile of the EDS signals (bottom) of the 7M sample, investigated on site 1, measured on 20 kV.

The Na, Mg, K, Ca, Fe remained rather uniformly distributed, redistribution of Ba and Zr but also Al took place in a complementary way. Grains with surplus of Si and O are formed.



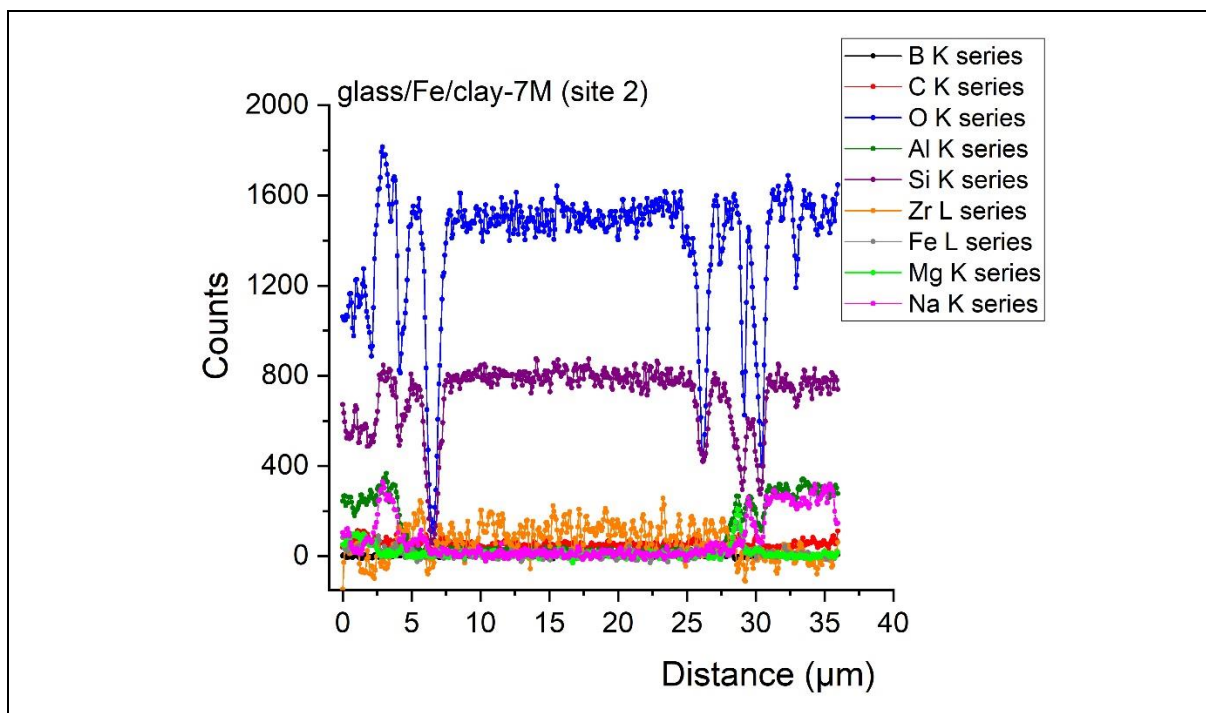


Figure 3-13 - SEM image and the line profile of the EDS signals of the 7M sample, investigated on site 2, measured on 5 kV.

The elemental maps recorded on 5 kV show that redistribution of the Si and O components occurred (Fig 3-13). The B, Mg, Fe remained rather uniformly distributed, relocation of Na and Al but also Zr took place in a complementary way. Grains with surplus of O and Si are formed.

3.5 Analysis of leaching solution

For inductively coupled plasma optical emission spectroscopy (ICP-OES), samples were acidified with 1 m/m% HNO₃ to determine their chemical composition. The ICP-OES measurements were performed on a *Perkin Elmer Avio 200 apparatus*. All elements were tested in radial view, using Y as the internal standard. The leachates were filtered through a cellulose acetate membrane and then were acidified with 1 m/m% nitric acid. The power of the generator was set to 1200 W during the measurements and the use of plasma argon was 12 l/min. The uncertainty was 5%.

To perform ionic chromatography (IC), the Thermo Scientific Dionex Aquion apparatus was used with AS23 column using 5 ml from the soaking liquid. The repeatability of measurements was within an acceptable range, standard deviation of 3 repetition was below 2% in all cases

We were able to sample 5 ml from the soaking liquid of which ICP-OES/IC investigations were performed after 3, 7 and 12 months. B, Ca, K, Mg, Na and Si were measured using ICP-OES instrument, while IC was used for Cl⁻ and SO₄²⁻. The pH values indicate a slight increase with time, 8.12 (3M), 8.25 (7M) and 8.27 (12M).

The ICP-OES and IC results on the dissolution of borosilicate glass/Fe/BCF samples are presented in Table 3-6.

Table 3-6 – ICP-OES and IC results, compared the 3-7-12 months sampling

	B	Ca	K	Mg	Na	Si	Cl ⁻	SO ₄ ²⁻
--	---	----	---	----	----	----	-----------------	-------------------------------

	[mg/l]							
SBPW recipe	-	125	7	57	380	-	817	182
SBPW conditioned	n.a.	108	22	49	492	5.9	823	182
3M	n.a.	59.4	232.2	28	610.7	101.8	830	234
7M	39.72	64.71	163.45	27.01	713.6	29.83	841	246
12M	45.52	64.48	162.58	23.83	673.01	40.79	891	280

Higher Si, Na and K concentrations were found in the final pore water of the glass/Fe/clay system compared to the initial conditioned one. The conditioning of Boda Claystone with the applied synthetic porewater was carried out at room temperature. The temperature effect could not be ruled out when experiencing elevated concentrations. However, as our experimental setup contains not only argillaceous rocks, leaching from the other components (Fe, glass) should also be considered. Elevated Si, B and Na concentrations can be traced back to glass content as in our previous glass studies (Fabian et al, Scientific Reports 11, 13272 (2021)) the dissolution rate of these three elements followed the same tendency (larger dissolution at the beginning of the tests and the rate decreased over time) as in current experiment. Concentration of bivalent cations (Mg and Ca) decreased, while the concentration of K increased by one order of magnitude. Elevated Si concentration originating from glass dissolution could trigger K release from the clay fraction. A large decrease in silicate and potassium was observed between 3M and 7 M, while the concentration of K and Si unchanged between 7M and 12M. A potential precipitation of potassium silicate species could be one explanation for the decreased concentration, but as a triplicate setup was applied, differences between containers can occur. Mg and Na concentrations remained in the same order of magnitude.

The boron concentration measured in the samples increases with time from 39.72 mg/l up to 45.54 mg/l, from 7M to 12M. High silicon concentration was measured after 3 months but decreased from 3M to 7M, after that increased from 7M to 12M. The Na concentration increases until the 7th month, after which it begins to decrease, maximum concentration was 713.6 mg/l. A low Mg concentration was measured, which slowly decrease with time from 28 mg/l to 23.83 mg/l.

Concentrations of Cl⁻ and SO₄²⁻ ions in the final pore water are close to the initial/conditioned concentration, but an increase was observed over time. The increase was less than 10% for chloride but higher for sulfate.

Table 3-6 indicates the concentrations determined after 3-7-12 months, it allows drawing the following conclusions:

- the concentrations (Ca, K, Na, Si) changed with time, and it was not linear with time. The composition of the leaching solution is determined predominantly by the dissolving of glass and clay particles.
- the dissolution rate calculated from the boron release after 7M and 12M (Table 3-7) indicates a very little change in dissolution rate with time.

Table 3-7 – Normalized mass loss and glass dissolution rate for boron

	C(B)	f(B)	NC(B)	NL(B)	d _{eq} (B)	r
	[mg/l]	-	[mg/l]	[mg/m ²]	[μm]	[mg/(m ² d)]
7M	39.72	0.032	1.251	1.14	0.43	0.0054
12M	45.52	0.032	1.434	1.31	0.49	0.0011

The obtained dissolution rates (Table 3-7) show a decreasing tendency between 7M and 12M. Boron is usually assumed to provide the best measure of the extent of glass reaction as a consequence of its high solubility. The release of boron occurred at an average rate of 0.0054 g/(m²d) until 7M and 0.0011 g/(m²d) from 7M to 12M. This extremely low value is due to the fact that in this composition the glassy sample does not come into direct contact with the leaching fluid as in most product consistency test (Gin et al., 2015; Music et al., 1988). The boron concentration in the 12M sample is only 45.52 ppm which suggests that there was no significant change in the structure of the glass during the long experimental period. The thickness of the alteration layer of glass grains can be estimated as $d_{eq}(B) \approx 0.5 \mu\text{m}$ which is below the resolution limit of backscattered electron imaging and EDX.

3.6 Other tests and characterizations

3.6.1 X-ray diffraction (XRD) analysis

X-ray diffraction (XRD) analysis was carried out on each sample (3M, 7M and 12M) but did not allow the identification of crystalline phases connected to iron-oxide. XRD measurements were performed using a Bruker AXS D8 Discover diffractometer equipped with Göbel-mirror and a scintillation detector with Cu K α radiation. The X-ray beam dimensions were 1 mm \times 5 mm, the 2 θ step size was 0.02°, scan speed 0.1°/min, at room temperature (25°C). We used the Diffrac.EVA program and the ICDD PDF database.

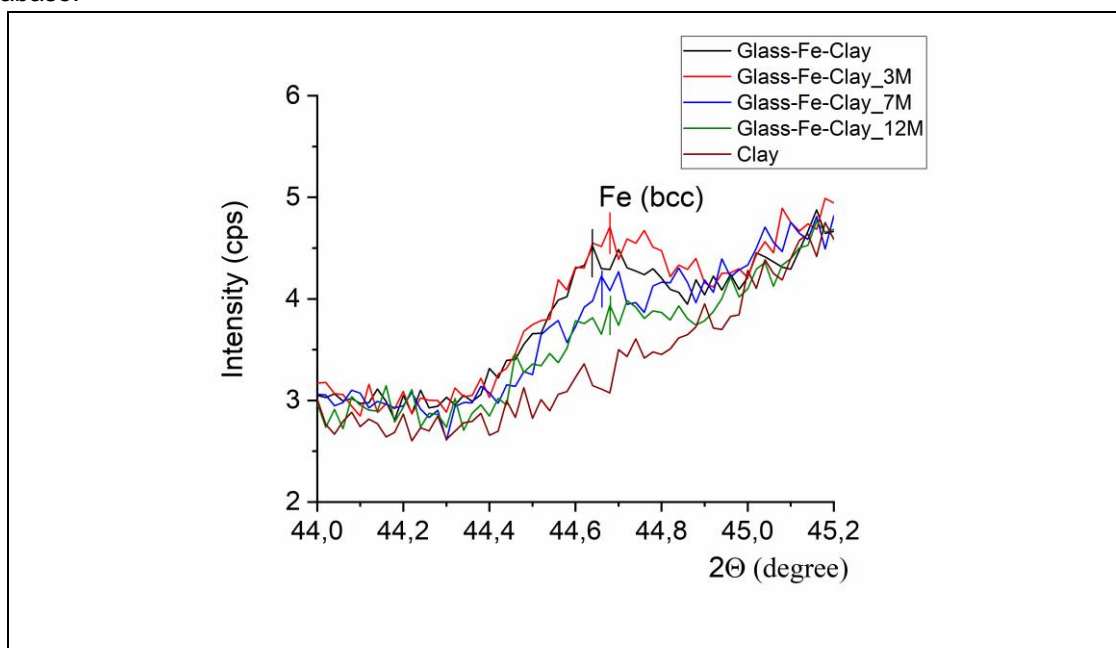


Figure 3-11 – Diffraction pattern of glass/Fe/clay mixture in function of treatment time.

No iron-oxide was detected in the glass/Fe/clay mixture. The strongest line of iron has been trapped, but it is also very weak. On the other hand, it appears that as treatment time progresses the Fe line decreases. The Fe line is the highest in the initial mixture without heating called Glass-Fe-Clay (black line) and 3M sample, then the 7M sample is smaller, the 12M sample is even smaller, and finally there is no signal in the pure claystone (Clay) sample. No corrosion products could be identified by the methods used.

4 Experiment 3: Glass/Steel/Cement-bentonite/Clay system, 70°C

4.1 Background

Partner: EDF/ ANDRA

Contact Person: Dr. Florent Tocino (florent.tocino@edf.fr)

The main objective of these experiments is to determine glass dissolution rate when it is surrounded by various materials (clay, steel, corrosion products, cement-bentonite). Two glasses were studied. Experiments were conducted at 70°C in static mode up to 3 years.

4.2 Description

To reduce any chemical disturbances, experiments were carried out in watertight reactors in stainless steel (Figure 4-1).



Figure 4-1 – Stainless steel reactors

Samples were placed in the clay coming directly from the Meuse/Haute-Marne URL. The reactors contain an anoxic leaching solution. The system was static which means the leaching solution was only introduced at the start of the experiment to saturate the clay. All the reactors were kept in a stove at 70°C, and the experiments lasted 3 years (ended in July 2021). The experiments were performed with two types of glass, SON68 glass (R7T7 surrogate) and AVM V₄ representative of the whole French AVM production² average behaviour.

Each reactor contained 3 types of samples (Figure 4-2). The first one was glass powder inside a pierced steel canister: this sample dimensioning has been done to observe a decrease in leaching rate during the experiment. In other words, the experiment will capture the transition between initial and residual dissolution rates.

Each setting was tested with and without a cementitious buffer between the different samples and the clay.

The second one was the same, but the canister were coated with magnetite in order to observe the impact of corrosion products.

The last one was composed of two glass monoliths squeezed between a stainless steel plate on one side and a steel plate on the other (making a “sandwich” sample).

² AVM glasses result from vitrification campaigns at the Marcoule vitrification facility (AVM).

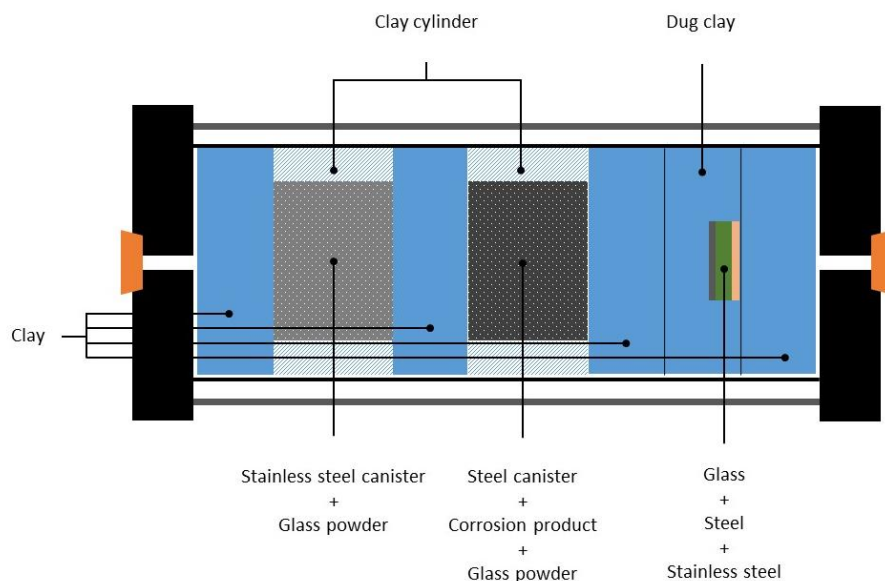


Figure 4-2 – Stainless steel reactor schematic representation (without buffer)

For each configuration, four durations were considered: 6, 12, 24 or 36 months, meaning we had a total of 16 reactors (Table 4-1 and Table 4-2) with 3 samples per reactor. A total of 48 samples have been characterized by the end of 2021.

Table 4-1 – Configurations tested

Configurations	Names	End (months)			
		6	12	24	36
SON68_cement buffer	S_C	S_C_6	S_C_12	S_C_24	S_C_36
SON68	S	S_6	S_12	S_24	S_36
AVMv4_cement buffer	A_C	A_C_6	A_C_12	A_C_24	A_C_36
AVMv4	A	A_6	A_12	A_24	A_36

Table 4-2 – Schedule

n						n+1						n+2																							
1	2	3	4	5	6	7	8	9	10	11	12	13	14	15	16	17	18	19	20	21	22	23	24	25	26	27	28	29	30	31	32	33	34	35	36
23/05/2018						23/11/2018						23/05/2019						23/05/2020						22/07/2021											
S_6						S_C_6						S_C_24																							
S_12												S_24																							
A_6						A_C_6						A_C_24																							
A_12												A_24																							
A_C_12						S_C_12																													
						A_C_36																													
						A_36																													
						S_36																													
						S_C_36																													

EURAD Deliverable D2.12 – High level radioactive waste package – Characterization of glass/steel/buffer interaction experiments

At the end of the test, reactors are opened. Samples are cut, freeze-dried and coated to be kept weeks or even months if needed, they are only polished minutes before characterisation.

SEM observations and EDS analysis are then carried out to determine the alteration layer thickness and its composition.

Experiments started in May 2018 and ended in July 2021 (Table 4-2). After 3 years we have successfully opened all 16 reactors and analysed 48 samples

4.3 Materials involved: Chemical composition

Host rock: Host clay (CIGEO site)

Buffer material: Cement-Bentonite grout

Canister: stainless steel, steel

Waste: nuclear glass surrogates (SON68, AVM V₄)

Leaching solution (Table 4-3).

Table 4-3 – Mass of reagents for 1 kg of solution

<u>Reagents</u>	<u>Quantities</u>
Al (10 mg/L)	638 µL
CaSO ₄ ,7H ₂ O	1.6452 g
MgSO ₄ ,7H ₂ O	1.0120 g
KCl	0.0526 g
NaCl	1.8611 g
Na ₂ SO ₄	0.1775 g
SrCl ₂ ,6H ₂ O	0.0555 g
FeSO ₄ ,7H ₂ O	0.0141 g
Na ₂ SiO ₃ ,5H ₂ O	0.0746 g
NaHCO ₃	0.4815 g
CaCO ₃	~ 1 g

4.4 Solid or interface characterization

4.4.1 SEM

SEM images have been obtained using an FEI SEL QUANTA 650 in environmental mode ($P_{\text{water}} = 140$ Pa).

Acceleration voltage: 10 kV

Working Distance: 10 mm

Detector: BSE GAD

During the interface characterization the main information we seek is the alteration layer thickness, as it gives us direct information about glass dissolution rate. This report will not present all the SEM observations we carried out on the 48 samples. SEM observations showed the presence of an alteration layer on every sample of AVM glass after 6, 12, 24 and 36 months. Figure 4-3 presents a typical alteration layer observed after 6 months on an AVM glass monolith facing steel. On the contrary, no

layer has been found on any of the SON 68 glass powder samples, only one on the monolith samples (sandwich samples).

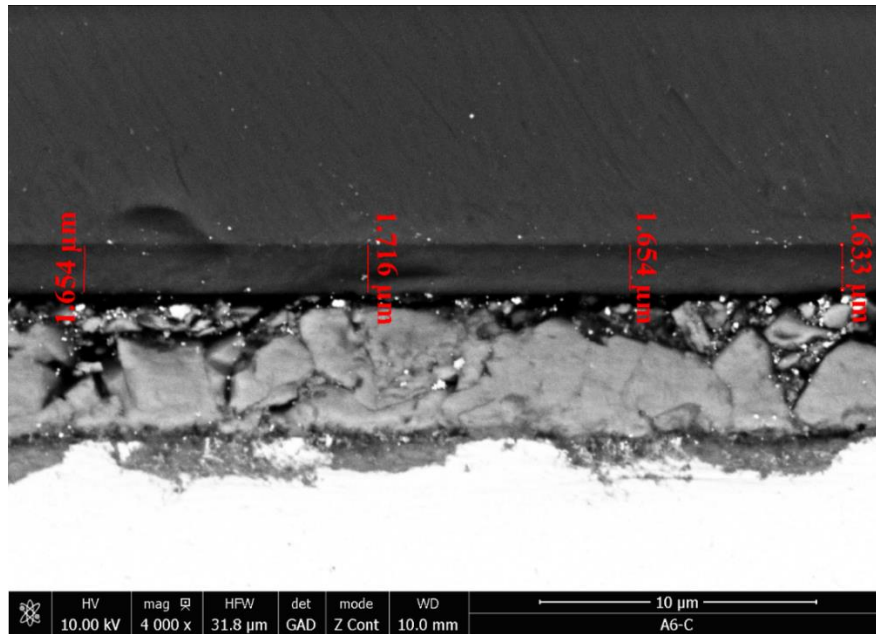


Figure 4-3 – AVM glass sample monolith facing steel after being dissolved for 6 months

We measured the layer thickness at least 20 times for each sample to obtain an average measure and the associated uncertainty. All measurements of the alteration layer thickness we obtained are presented in the figures below.



Figure 4-4 – Alteration layer thickness measured on AVM glass after 6, 12, 24 and 36 months. Steel canister (A), steel canister coated with magnetite (B) and “Sandwich” (C).

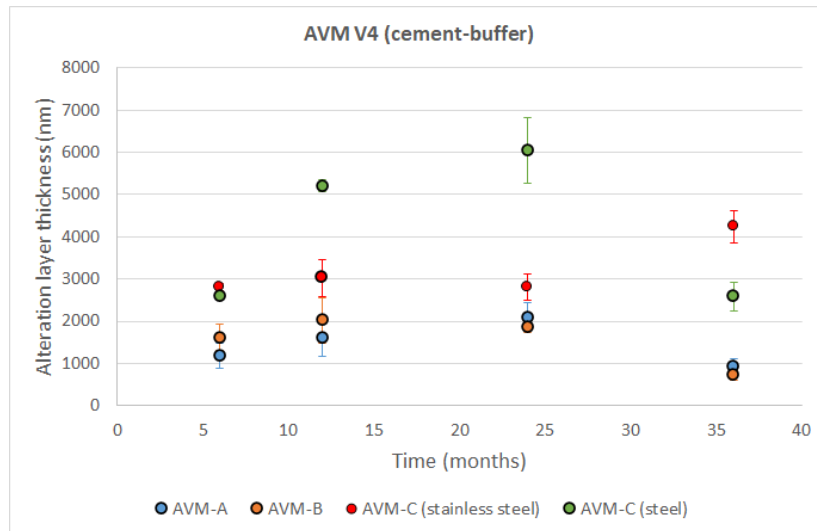


Figure 4-5 – Alteration layer thickness measured on AVM glass (with buffer) after 6, 12, 24 and 36 months. Steel canister (A), steel canister coated with magnetite (B) and “Sandwich” (C).



Figure 4-6 – Alteration layer thickness measured on SON 68 glass after 6, 12, 24 and 36 months. Steel canister (A), steel canister coated with magnetite (B) and “Sandwich” (C).

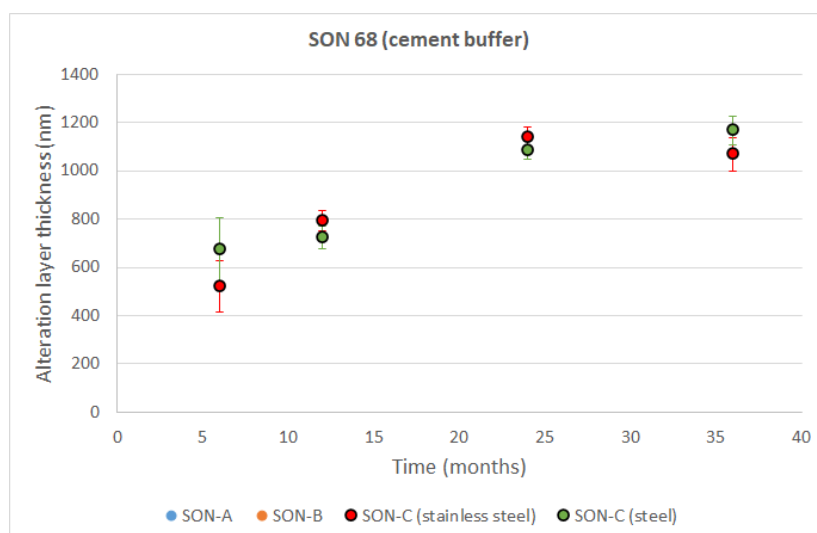


Figure 4-7 – Alteration layer thickness measured on SON 68 glass (with buffer) after 6, 12, 24 and 36 months. Steel canister (A), steel canister coated with magnetite (B) and “Sandwich” (C).

These results do not show a clear effect of the buffer on the alteration layer thickness and on the dissolution rate as the differences between Figure 4-4 and Figure 4-5 on one hand, and Figure 4-6 and Figure 4-7 on the other hand are not significant.

As expected, AVM V4 glass dissolves faster than SON 68 and the measured initial and residual rates are in good agreement with the literature.

SEM observations carried on SON 68 Samples showed a very heterogeneous alteration in the iron and clay vicinity. The buffer presence do not amplify this effect event with the increase of the alteration layer thickness.

4.5 Analysis of leaching solution

Leaching solution can not be carried out on these experiments because each reactor contains 3 samples. If we were able to recover enough solution (which would be very difficult), the information obtained would be an average concentration not very helpful.

4.6 Other tests and characterization

TOF-SIMS characterisations have been carried out on the 36 months lasting experiments, in collaboration with CEA. According to the resolution of ToF-SIMS, no valuable information were obtained from these analyses. It was then decided to not include them in the report. The results will be completed in 2022.

5 Experiment 4: Glass/Steel/Cement system, 25°C

5.1 Background

Partner: SCK CEN, SUBATECH, University of Lorraine

Contact person: Jules Goethals (goethals@subatech.in2p3.fr), Jérôme Sterpenich (Jerome.sterpenich@univ-lorraine.fr), Karine Ferrand (karine.ferrand@sckcen.be), Karel Lemmens (karel.lemmens@sckcen.be), Sanheng Liu (Sanheng.liu@sckcen.be)

5.2 Description

The integrated tests were performed at room temperature in stainless steel cells (length = 135 mm; internal diameter = 80 mm), which were filled with hydrated ordinary Portland cement paste (water to cement ratio (W/C) = 0.4) and a layer of glass powder (SON68 glass or SM539 glass with a size fraction between 125 and 250 µm) separated by a 2.5 mm thick stainless steel filter with a 10 µm average pore diameter. In order to perform sampling of the leaching solution, four holes were drilled in the cement plug (diameter = 6 mm, height = 75 mm), whereas in the glass compartment a tubular stainless steel filter (110 µm average pore diameter) was placed. The theoretical volume available for sampling was very low, *i.e.* 2.12 mL in the drilled holes and 3.7 mL in the glass compartment. Based on the amount of glass powder and the density of the glass (Table 4-3), the glass compartment porosity is equal to 48% for the cell with SM539 glass and 54% for the cell with SON68 glass. This means that the glass compartment, having a total volume of 88 cm³, contains 43 mL of water for the cell with SM539 glass and 48 mL of water for the cell with SON68 glass. A cross section of the cell is presented in Figure 5-1, and material specifications are given in Table 5-1.

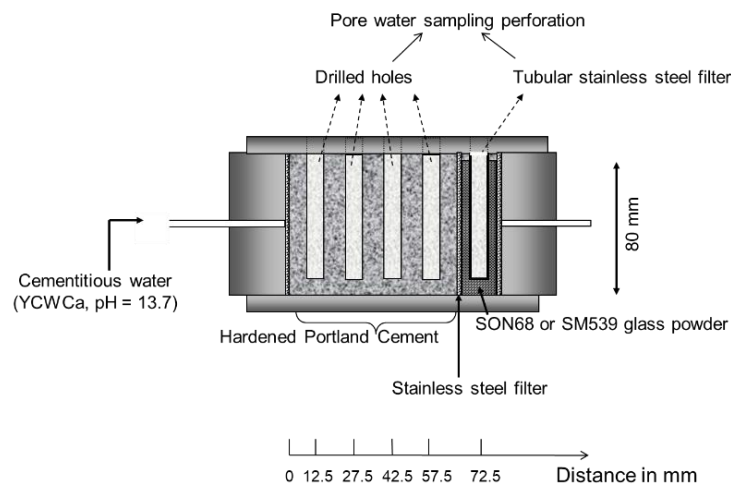


Figure 5-1 – Experimental setup for the integrated tests (hardened ordinary Portland cement paste/stainless steel filter/glass powder).

Table 5-1 – Material specifications for the integrated tests (uncertainties are given at 95 % confidence interval).

Glass	SM539	SON68
Glass (125-250 µm) weight (g)	110 ± 0.005	110 ± 0.005
Glass layer (mm)	17.5 ± 0.02	17.5 ± 0.02

Glass density (g.cm ⁻³)	2.45 ± 0.01	2.75 ± 0.01
Glass specific surface area (m ² .g ⁻¹)*	0.0310 ± 0.0002	0.0310 ± 0.0002
CEM I 42.5 R HSR LA CCB cement height (mm)	64 ± 0.02	64 ± 0.02
CEM I 42.5 R HSR LA CCB cement weight (g)	637.6 ± 1.2	648.6 ± 1.2

The drilled sampling holes were filled with a synthetic cementitious solution referred to as Young Cement Water with Ca (YCWCa; Table 5-2), and an increasing Ar pressure from 2 to 15 bar was applied to accelerate the saturation of the cement plug. The holes were regularly checked and refilled when it was necessary. After 1 year, the cell reached a constant weight after addition of a cumulated total volume of ~44 mL YCWCa. When the volume of the glass compartment was completely filled with YCWCa, Ar pressure application was stopped to leave the system under static conditions. After different periods of time (Table 5-3), 1 mL of solution was taken to measure the pH, and then diluted with 2 mL of Milli-Q® water, ultrafiltered at 10 000 D, and analysed by ICP-AES or ICP-MS and IC (see section 5.5).

Table 5-2 – Composition of the synthetic cementitious water referred to as YCWCa in mg/L.

Element	Al	Ca	K	Na	Si	SO ₄ ²⁻	TIC	pH
YCWCa	0.10	13.8	12300	3200	4.8	183	89	13.7

Table 5-3 – Schedule of the integrated test

Glass	Starting date	Sampling date	Dismantling
SM539	2009-10-28	2010-04-26 (180 days)	2016-06-21 (2428 days)
SM539		2010-10-28 (365 days)	
SM539		2011-04-05 (524 days ¹)	
SM539		2011-10-05 (707 days)	
SM539		2012-04-13 (898 days)	
SON68	2009-08-27	2010-02-24 (182 days)	2016-06-21 (2490 days)
SON68		2010-09-14 (383 days)	
SON68		2011-04-05 (586 days ²)	
SON68		2011-10-05 (769 days)	
SON68		2012-04-13 (960 days)	

¹ Sampling followed by refilling with YCWCa containing 30 mg/L si

²No sampling in the glass compartment, only refilling with YCWCa

Note that after 586 days, in the cell with SON68 glass, there was not enough solution in the tubular stainless steel filter (glass compartment) and in the first two cement sampling holes. Consequently, to allow sampling for longer durations, all sampling holes were refilled with YCWCa for the cell with SON68 glass, and with YCWCa containing 30 mg/L of Si, *i.e.* the same Si concentration as the one determined after 365 days, for the cell with SM539 glass.

After the last sampling, there was an unknown remaining amount of cement water in the glass compartment, so the alteration of the glass particles continued until the cells were dismantled. The tests were dismantled 1530 days after the last sampling (total duration = 2428 days for SM39 glass and 2490 days for SON68 glass). In a first instance, water was removed by applying Ar pressure until a constant

weight was reached, then a lyophilisation was done and the whole system was embedded under vacuum with an epoxy resin. Note that during this operation, the resin has not penetrated completely into the cement paste. Afterwards, cores were drilled in the cells at CRITT (Alsace, France) to perform some preliminary characterizations. Then, cells were totally dismantled at SUBATECH with a lathe milling machine in order to collect additional material for the solid characterizations. During the operation, the exposed surfaces (top and bottom of the cell) were protected with silicone paste to avoid contamination from water cooling fluid used for cutting. The interfaces between the different materials were totally preserved after this process. The interior of the cell was then embedded in an epoxy resin (Struers® Specifix), and cut prior to the different analyses. The different cutting operations were realized using a diamond wheel and a diamond wire saw. The embedded cross sections were ground with 600, 1200, 2400 and 4000 SiC grit papers and polished with 1 µm diamond suspension. All the cutting and polishing operations were realized with ethanol or without any lubricating fluid to preserve the samples from carbonation and other alteration processes.

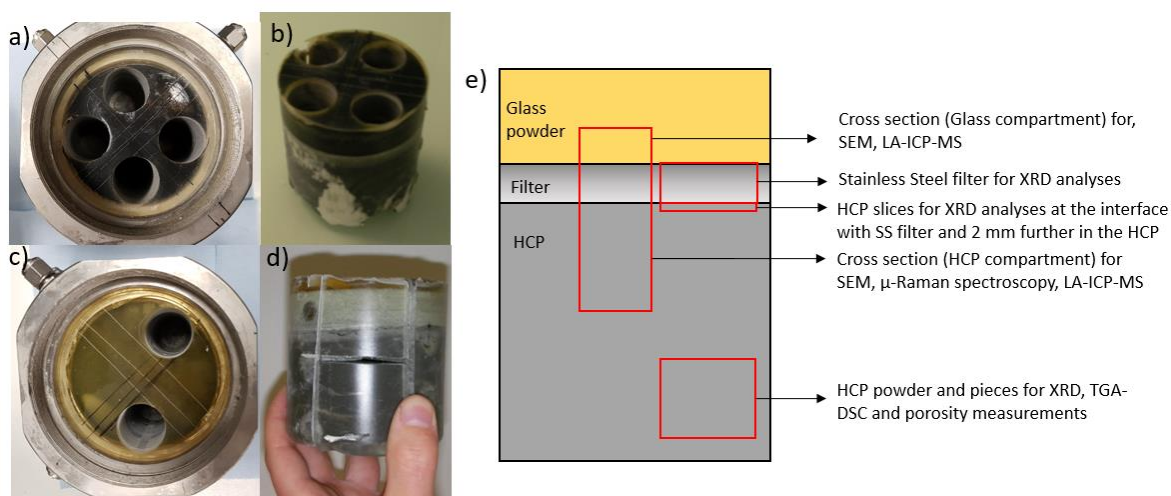


Figure 5-2: Pictures of SON68 with filter cell prior (a) and after dismantling (b) and of the SM539 with filter cell prior (c) and after dismantling following embedding in epoxy resin and cutting (d), as well as, a sketch in cross section view of the cell describing the solid samplings realized for the different solid characterizations (e).

5.3 Materials involved

5.3.1 Hardened ordinary Portland cement

The hardened ordinary Portland cement paste (HCP, hardened cement paste) was prepared by mixing 1000 g of Cement CEM I 42.5 R HSR LA CCB (Table 5-4) with 400 g of tap water (*i.e.* W/C = 0.4) directly in the stainless steel cells, removing air bubbles by stirring with a spoon. The mixing was allowed to harden at room temperature during 20 days.

Table 5-4 – Average analytical composition in weight % of CEM I 42.5 HSR5R LA CCB Portland cement provided by CIBELCOR®

SiO₂	21.4
Al₂O₃	3.3
Fe₂O₃	4.0
CaO	63.3
MgO	2.4

SO₃	2.8
K₂O	0.57
Na₂O	0.15
Cl⁻	0.03
% Na₂O eq	0.53
C3A (tricalcium aluminate)	2
Fire loss	1
Insoluble residues	0.1

5.3.2 Stainless Steel

A stainless steel filter (316L) from GKN (diameter = 80 mm ; thickness = 2.5 mm ; average pore size = 10 µm ; mass = 65.8 g) was used to separate the glass from the cement plug.

5.3.3 Glass

Two inactive aluminoborosilicate glasses were used: SON68 glass (inactive French borosilicate reference glass) and SM539 HE 540-12 glass (PAMELA Belgian reference glass); their nominal composition is given in Table 5-5.

Table 5-5 – Nominal composition of SON68 and SM539 HE 540-12 glasses in weight %.

Oxide	SON68	SM539
SiO₂	45.48	35.27
B₂O₃	14.02	25.57
Na₂O	9.86	8.77
Al₂O₃	4.91	20.23
CaO	4.04	5.04
Li₂O	1.98	3.49
Fe₂O₃	2.91	0.45
TiO₂	0	0.003
NiO	0.74	0.011
Cr₂O₃	0.51	0.033
ZnO	2.50	0
P₂O₅	0.28	0
SrO	0.33	0.005
ZrO₂	2.65	0.046
MoO₃	1.70	0.017
MgO	0	0.130
MnO₂	0.72	0.035
CoO	0.12	0
Cs₂O	1.42	0
BaO	0.60	0
Y₂O₃	0.20	0
La₂O₃	0.90	0.007

5.4 Solid or interface characterization

5.4.1 Methods

5.4.1.1 SEM-EDXS

EDXS-Mapping and analyses were performed at the Service Commun de Microscopie Electronique et de Microanalyses (SCMEM) of GeoResources Laboratory in Nancy on a TESCAN VEGA3 with a counting time of 60 s, 20 kV, 1.5 nA for EDXS analyses and 1 ms per pixel, 15 kV and 10 nA for mapping. BESEM images were also collected with a JEOL 7600F microscope operating at 15 KeV and 0.5 nA at IMN (Institut des Matériaux de Nantes). Phase quantifications were assessed at the interface between HCP and the stainless steel filters by gray level analyses using Jmicrovision© (Roudit, 2007). Images were collected at different magnification (x500, x800, x1000, x1500), adapted to the analysed area. The total covered surface area was chosen high enough to be representative of the cement paste heterogeneity. The images contain pixels with different shades of grey ranging from 0 (black) to 255 (white), which are linked to the contrast of the phase and its BE (backscattered electron) coefficient η . The fractional volume of a phase is proportional to its image area (Scrivener, 2004) and was determined by integrating the histogram in the interval of grey level corresponding to a phase or a group of phases (typically C2S, C3S, C4AF, C3A together in the group Unreacted Cement phases). The gray level boundaries were adjusted manually in the histograms to fit the BE-SEM images.

5.4.1.2 XRD

After the dismantling of the cells, cement paste slices were cut with a diamond wire saw in order to preserve the interface, and the slices were directly scanned in a Bragg-Brentano geometry both at the interface and approximately 2 mm further in the cement paste. The stainless steel filter pieces coming from both cells were taken off from the HCP and the resin and analysed in the same geometry. A D5000 Bruker AXS diffractometer equipped with a Cu anticathode ($\lambda = 1.5406 \text{ \AA}$) operating at 40 kV and 25 mA was used. The scans were collected with a knife in the range $2\theta = 5^\circ$ to 70° with a step size of 0.01° and 3 sec/step.

5.4.1.3 TG-DSC

The analyses were carried out using a Setaram TG-DSC 111 thermo-gravimetric analyser. Approximately 16 mg of ground powders, dried under Ar with silica gel for at least 24 hours, were placed in a Pt-Rh crucible and heated to 1000°C under a nitrogen flow of 70ml/min at a rate of $10^\circ\text{C}/\text{min}$. Blank measurements were subtracted from the scans to correct for the buoyancy effect. The analyses were conducted in duplicate in order to assess the standard deviation of the results.

5.4.1.4 μ -Raman spectroscopy

The Raman experiments were conducted at LPG (Laboratoire Planétologie et Géodynamique, Nantes) using a Jobin-Yvon Labram© HR800 Evolution spectrometer equipped with a 1200 lines/mm grating. The Raman excitation was applied using a solid-state 633 nm wavelength laser set at low power ($<1 \text{ mW}$) to avoid phase degradation under the beam. The laser beam was focussed using a 100x Olympus objective leading to a theoretical spot size of $0.90 \mu\text{m}$. The acquisition time on a given sample was typically between 20 and 60 s and 10 accumulations. Calibration on a silicon standard using the 520.5 cm^{-1} band was performed prior to measurements. The spectra were acquired using the Labspec 6 © software package, and the RRUFF database (Lafuente et al., 2015) was used for phases identification.

EURAD Deliverable D2.12 – High level radioactive waste package – Characterization of glass/steel/buffer interaction experiments

5.4.1.5 LA-ICP-MS

LA-ICP-MS quantitative analyses were performed at the GeoRessources laboratory (Nancy, France) and at SUBATECH (Nantes, France) in spot and line mode analyses, respectively. The sample acquisition parameters are reported in Table 5-6.

For the spot analyses, Si and Al and Ca data were used as internal standards depending on the analysed phase. The data reduction (quantification and limits of detection) was carried out using Iolite software (Paton et al., 2011) based on the equations developed by (Longerich et al., 1996).

For the profile analyses, as the concentration of the major constituting elements of the cement paste (i.e.: Ca, Si, Al, Fe, Na, K) were potentially varying at the interface, it was not possible to use such elements as internal standard. Instead, the sum normalisation process was used to calculate the concentrations of the 58 elements measured (Gagnon et al., 2008; Liu et al., 2008; van Elteren et al., 2009).

Table 5-6 – Operating conditions for the LA-ICP-MS measurements.

Laboratory	SUBATECH	GEORESSOURCES
Laser ablation device	NWR UP 213	Excimer laser (ESI NW193)
Wavelength	213 nm	193 nm
Pulse energy	0.5 mJ (50%)	
Fluence	22 J cm ⁻²	5,00 Jcm ⁻²
Repetition rate	10 Hz	5Hz
Spot size diameter	55 µm	10,20,60 µm
Scanning speed	5 µm s ⁻¹	-
Ablation mode	Line (550 µm)	Spot
Washout time	80 s	20 s
Warmup time	110 s	30 s
Carrier gas flow rate (He)	0.67 L min ⁻¹	0.62 L min ⁻¹
Make-up gas flow rate (Ar)	0.73 L min ⁻¹	0.67 L min ⁻¹
ICP-MS device	Thermo Scientific Element XR, single collector high resolution ICP-MS	Agilent 8900 triple quadrupole IC-PMS
RF power	1250 W	1550 W
Auxiliary gas flow rate (Ar)	0.90 L min ⁻¹ (LA mode)	0.87 L min ⁻¹
Cool gas flow rate (Ar)	16 L min ⁻¹	12 L min ⁻¹
Sampler and skimmer cones	Ni	Ni
External standard	NIST 610 SRM, NIST 612 SRM (Babaei et al., 2021)	
Analysed Isotopes	⁷ Li, ⁹ Be, ¹¹ B, ²³ Na, ²⁵ Mg, ²⁷ Al, ² ⁹ Si, ³¹ P, ³⁹ K, ⁴³ Ca, ⁴⁵ Sc, ⁴⁷ Ti, ⁵¹ V, ⁵³ Cr, ⁵⁵ Mn, ⁵⁷ Fe, ⁵⁹ Co, ⁶⁰ Ni, ⁶³ Cu, ⁶⁶ Zn, ⁶⁹ Ga, ⁷⁵ As, ⁷⁷ Se, ⁸⁵ Rb, ⁸⁸ Sr, ⁸⁹ Y, ⁹⁰ Zr, ⁹³ Nb, ⁹⁵ Mo, ¹⁰⁷ Ag, ¹¹¹ Cd, ¹¹⁵ In, ¹¹⁸ Sn, ¹²¹ Sb, ¹³ ³ Cs, ¹³⁷ Ba, ¹³⁹ La, ¹⁴⁰ Ce, ¹⁴¹ Pr, ¹ ⁴⁶ Nd, ¹⁴⁷ Sm, ¹⁵³ Eu, ¹⁵⁷ Gd, ¹⁵⁹ Tb, ¹⁶³ Dy, ¹⁶⁵ Ho, ¹⁶⁶ Er, ¹⁶⁹ Tm,	⁷ Li, ¹¹ B, ²³ Na, ²⁵ Mg, ²⁷ Al, ²⁹ Si, ³⁴ S, ³⁹ K, ⁴³ Ca, ⁴⁴ Ca, ⁴⁷ Ti, ⁵² Cr, ⁵⁵ Mn, ⁵⁶ Fe, ⁵⁹ Co, ⁶⁰ Ni, ⁶⁶ Zn, ⁷⁸ Se, ⁸⁸ Sr, ⁸⁹ Y, ⁹⁰ Zr, ⁹⁵ Mo, ¹⁰³ Rh, ¹⁰⁵ Pd, ¹⁰⁷ Ag, ¹¹¹ Cd, ¹¹⁸ Sn, ¹²¹ Sb, ¹³³ Cs, ¹³⁷ Ba, ¹ ³⁹ La, ¹⁴⁰ Ce, ¹⁴¹ Pr, ¹⁴⁶ Nd, ²³² Th, ²³⁸ U

	¹⁷² Yb, ¹⁷⁵ Lu, ¹⁷⁸ Hf, ¹⁸¹ Ta, ¹⁸² W, ¹⁹⁷ Au, ²⁰⁸ Pb, ²⁰⁹ Bi, ²³² Th, ²³⁸ U	
Acquisition/counting time	180 s	Li, B : 20 ms/Other elements: 10 ms
Detector Mode	Triple	Triple
Mass resolution mode	300	-
Mass window	⁷ Li, ⁹ Be, ¹¹ B 50%, others 20%	-
Runs × passes	50 × 1	-

5.4.2 Results

Preliminary characterizations of both cells by SEM-EDXS were reported in Gin et al. (2019) as well as in Ferrand et al. (2018). In this report, a combination of techniques including SEM-EDXS, ATG-DSC, XRD, μ -Raman spectroscopy and LA-ICP-MS were used to further investigate (1) the impact of glass on the mineralogical and microstructural evolution of the HCP and (2) the alteration of glass in highly alkaline media. First, the initial material involved in this study was more deeply characterized, including measurements of the HCP porosity, chemical and mineralogical analyses. These latter data can be further compared with a HCP hydration geochemical model. Secondly, the interface between glass and HCP (separated by a stainless steel filter) was characterized in both compartments (glass and HCP).

In the two cells, the alteration of the glass grains is heterogeneous depending on their location. It seems that the grains located in the first 400 μ m close to the stainless steel filter are more altered. For SM539 glass, grains at the vicinity of the stainless steel filter show a multilayer alteration at their rim. According to Li and B contents, the core of some glass grains can be considered as still protected from leaching, but in the alteration layers, Na, Li, B, and Mo depletions are noticed. SON68 glass rather seems leached up to the core of each grain, as confirmed by the depletions of Li, B, Zn, Zr, Mo, Cs, Ce, La, and Mn. In this glass, Mg, K and S (from the cement and the leaching solution) enrichments are observed. Consequently, a different process of alteration and/or rate of dissolution of these two glasses may occurred during the experiments.

In the presence of SM539 and SON68 glass, the HCP is altered over a distance of approximately 80 μ m and 200 μ m, respectively. The altered layer is characterized by a porosity increase, and by mineralogical and chemical changes. The leaching of portlandite and the Si input from glass dissolution lead to the precipitation of C-S-H with low Ca/Si ratio in both cases. This C-S-H phase is enriched in alkalis coming from the HCP interstitial pore solution and partly fill the porosity created by the portlandite leaching. The interface is also characterized by a decrease in the unreacted cement (UC) phases (i.e. C2S, C3S, C3A, C4AF) content, due to the continuous leaching of hydrated products forming around the UC grains. Even if the tests were conducted in carbon-free atmosphere, the presence of important amount of calcite at the interface reveals the carbonation of this latter in both cases. A partial quantification of these microstructural and mineralogical changes were realized in this study.

In the test with SON68 glass, the formation of a dense phase, edging the HCP, with a very low Ca/Si ratio is depicted. This phase is enriched in element coming either from glass Li, Cs, B, from the HCP (K) or from both (Na) is depicted. This phase is also present in the filter pores close to the HCP. As it is poorly crystalline or amorphous, it is difficult to determine its exact nature. It can be either a C-S-H phase with a very low Ca/Si ratio that incorporate alkalis and B, or an alkali-silica gel similar to the one formed during Alkali Silica Reaction (ASR). Minor amounts of monocarboaluminate, that can incorporate boron and sulfur, are coexisting with this phase.

In the test involving SM539 glass, secondary alteration products also precipitate in much lower amount at the edge of the HCP. This Al-enriched phase presents a collomorph texture and is possibly a mixture

of glassy component with C-A-S-H or Al- containing alkali silica reaction gel. Minor amounts of zeolite were also observed in the same area.

In addition to these mineralogical, microstructural and chemical characterizations, the use of LA-ICP-MS allowed for determining the profile of 58 elements across the cement paste. Especially, the lithium and boron diffusion profiles³ were used in geochemical models that take into account cement alteration, glass dissolution and diffusion processes.

Finally, the corrosion of the stainless steel filter was not evidenced by the detection of corrosion products, at least at the studied scale (i.e. micrometer scale). However, enrichment of the secondary alteration products in Ni, Cr, and Mn were noticed. This suggests either that these elements were released by glass dissolution or that a slight corrosion of the stainless steel filter occurred.

5.4.2.1 SEM-EDXS

5.4.2.1.1 HCP compartment

SEM-EDXS analyses were conducted in order to assess the mineralogical, geochemical and microstructural changes in the unaltered cement paste and at the interface between the stainless steel filter and the HCP. EDXS analyses were also realized in order to attribute a grey level to the different cement phases observed, to further quantify them.

For both cells, analyses in the unaltered hardened cement paste coming from both cells reveal the presence of unhydrated cement clinkers such as brownmillerite (C4AF), larnite/belite (C2S) and alite (C3S). The matrix surrounding these UC grains consists in hydrated cement paste principally of a mixture of C-S-H and portlandite (Figure 5-2 to Figure 5-5). This latter phase is also present as large platy crystals in the unaltered HCP (Figure 5-2b). Some porous areas presenting needles enriched in sulphur (identified as a mixture between monosulfoaluminate and ettringite by EDXS) are also observed (see Figure 5-2 and Figure 5-3). Note that these phases are generally intricately mixed together, and thus the EDXS analyses plotted in the ternary diagram are often integrating several phases together. Eventually, some large grains containing Mg and O are also present, dispersed in the unaltered HCP. The TGA-DSC measurements revealed the presence of magnesite in both cells, indicating that a large fraction of the magnesium can be incorporated into this latter phase (see sections 5.4.2.3 and 5.6.2).

Some changes in the microstructure and in the mineralogy occur at the interface between the stainless steel filter and the HCP. An heterogeneous altered layer with a thickness of approximately 80 µm (that can reach up to 100 µm) is observed in the SM539 cell. This layer is characterized by an important porosity increase and an alkalis enrichment. However, this porosity is partly filled with a very porous phase, that is particularly rich in alkalis (see Figure 5-2). The mean Ca/Si ratio of this phase is below 1, and thus this phase was associated to a tobermorite like C-S-H. Note that this phase is also filling cracks, that probably formed during the curing time of the HCP at the vicinity of the interface (see Figure 5-2). Precipitation of C-S-H phase with low Ca/Si ratio is expected in this environment, due to the Ca leaching from portlandite and the Si input from glass leaching, leading to the pozzolanic reaction. Moreover, a high alkali uptake is revealed in this phase. This is in agreement with a literature data which showed that alkali uptake is favored in low Ca/Si C-S-H (Hong and Glasser, 1999; L'Hopital et al., 2016a; L'Hopital et al., 2016b; Labbez et al., 2011; Stade, 1989). The altered area also still contains UC phases such as C4AF and C2S/C3S. However, the C2S and C3S grains are replaced by inner HP (hydration products) in this area (see Figure 5-2b). In addition, a thin layer of approximately 5 to 10 µm thick is observed at the bottom edge of the HCP as well as in the stainless steel filter pores at the vicinity of the HCP (Figure 5-2b). This layer can present a collomorph texture with a Ca/Si close to 1, and a high content in aluminium and alkalis (see Figure 5-3). It can correspond to a layered Si gel more or less enriched in Ca, Al and alkalis that might reflect some local changes of the solution composition with

³ Li and B are typically considered as good glass dissolution tracers

time. It was identified as a C-A-S-H phase in Ferrand et al. (2018). More details about this phase are given in section 5.4.2.4.

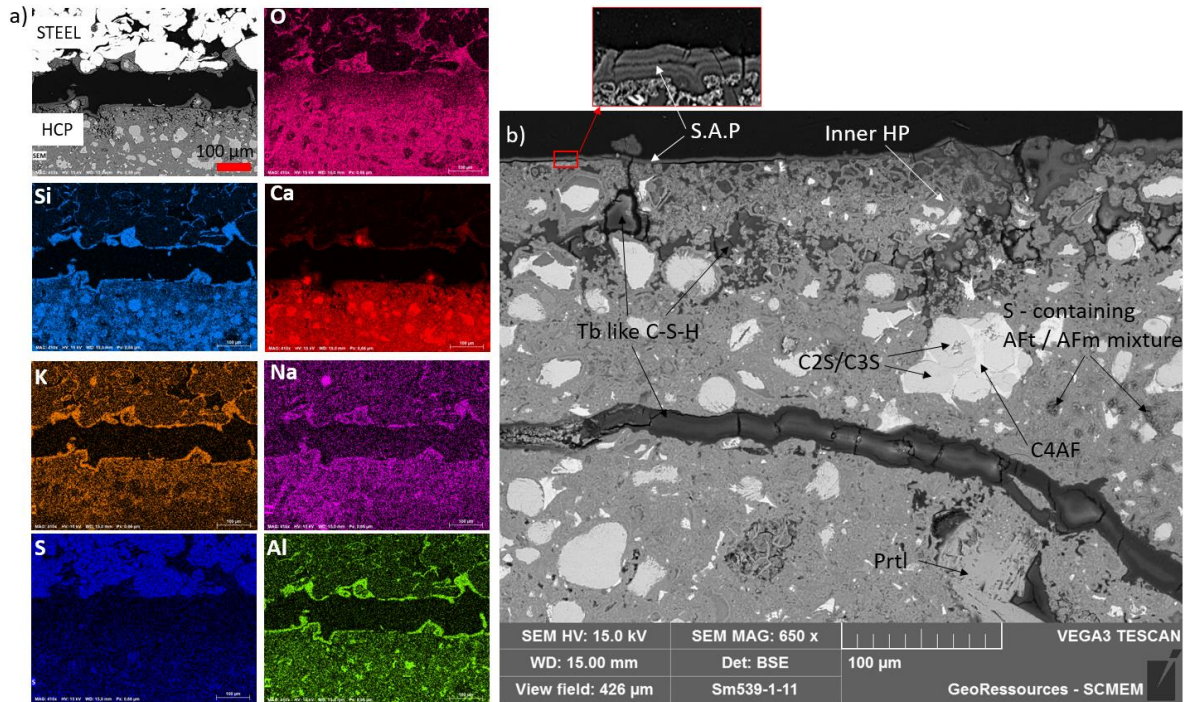


Figure 5-2 – EDXS mapping (a) and SEM micrograph (b) of the interface between SS filter and HCP in the SM539 cell. Identified phases are brownmillerite (C4AF), alite (C3S), belite (C2S), Inner hydration products (Inner HP), tobermorite like C-S-H (Tb like C-S-H), Prtl (portlandite), monosulfoaluminate and ettringite mixture (S-containing AFt/AFm mixture), and Secondary alteration products (S.A.P).

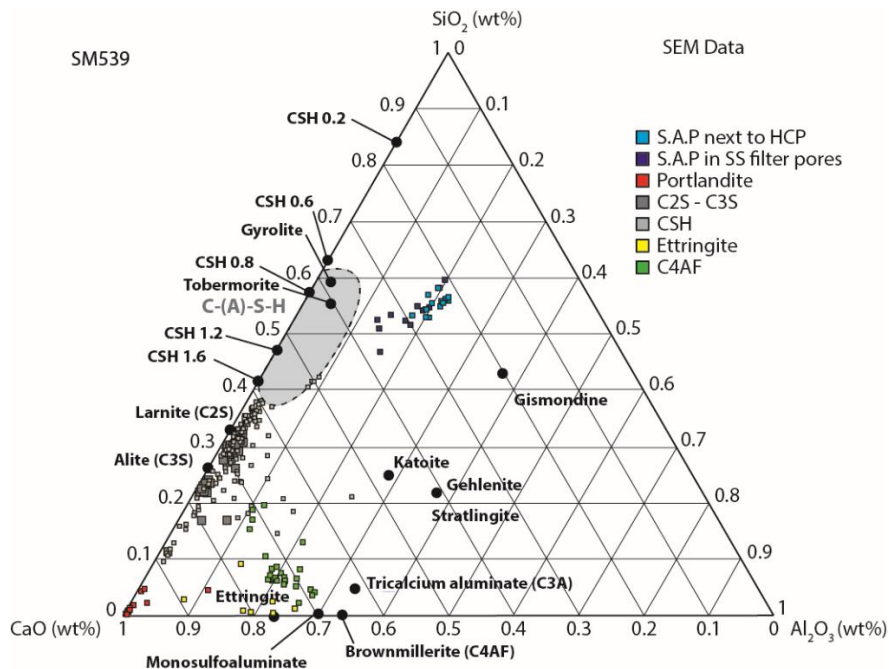


Figure 5-3 – Ternary diagram $CaO-SiO_2-Al_2O_3$ of SEM-EDXS analyses showing the plots of the chemical analyses of the OPC phases (C2S, C3S, portlandite, CSH, fibrous cement phase), the SON68 glass, the Secondary Alteration Phases (S.A.P.) next to glass grains (at the rim of grains), next to OPC paste. Reference minerals: tricalcium aluminate $Ca_3Al_2O_6$; ettringite $Ca_6Al_2(SO_4)_3(OH)_{12-26}H_2O$; alite Ca_3SiO_5 ; larnite Ca_2SiO_4 ; katoite $Ca_3Al_2(SiO_4)_{3-x}(OH)_{4x}$ $x=1.5-3$; gehlenite $Ca_2Al(AISi)O_7$;

tobermorite $Ca_5Si_6O_{16}(OH)_2 \cdot 4(H_2O)$; *stratlingite* $(Ca_2Al_2SiO_3(OH)_8 \cdot 4H_2O)$; *gismondite* $(Ca_2Al_4Si_4O_{16} \cdot 9H_2O)$; *brownmillerite* $(Ca_2(Al, Fe^{3+})_2O_5)$, *gyrolite* $NaCa_{16}Si_{23}AlO_{60}(OH)_{8-14}(H_2O)$.

In the cell with SON68 glass, the interface between the stainless steel filter and the HCP is also characterized by microstructural and mineralogical changes. The altered layer is also heterogeneous but thicker than in the cell with SM539 glass (approximately 200 μm). Again, this layer is characterized by an important porosity increase and an alkali enrichment with a partial filling of the porosity by Tobermorite like C-S-H (see Figure 5-4). In this cell, the UC content at the interface is very low, as the C2S and C3S grains are almost entirely replaced by inner HP (see Figure 5-4b). This can be related to the more important release of Si from the SON68 glass+. As in the cell with SM539 glass, the precipitation of S.A.P edging the HCP and in the stainless steel filter pores is depicted in this cell. This S.A.P layer is denser, thicker and more homogeneous than the alteration layer observed in the cell containing SM539 glass (see Figure 5-4). Mostly, it presents a very low Ca/Si ratio (<0.6) (see Figure 5-5), and incorporates a large amount of alkalis. It was identified as a C-S-H phase incorporating very little amount of Al and large amount of alkalis in Ferrand et al. (2018). Again, more details about this S.A.P layer characterization are obtained with the μ -Raman spectroscopy (section 5.4.2.4). Even if the interface seems to be depleted in S, we can observe the local presence of a S, Al, Ca and Si containing phase (see Figure 5-4a). This result indicates that AFt (such as ettringite) and/or AFm (such as monosulfoaluminate) phases remain at the interface.

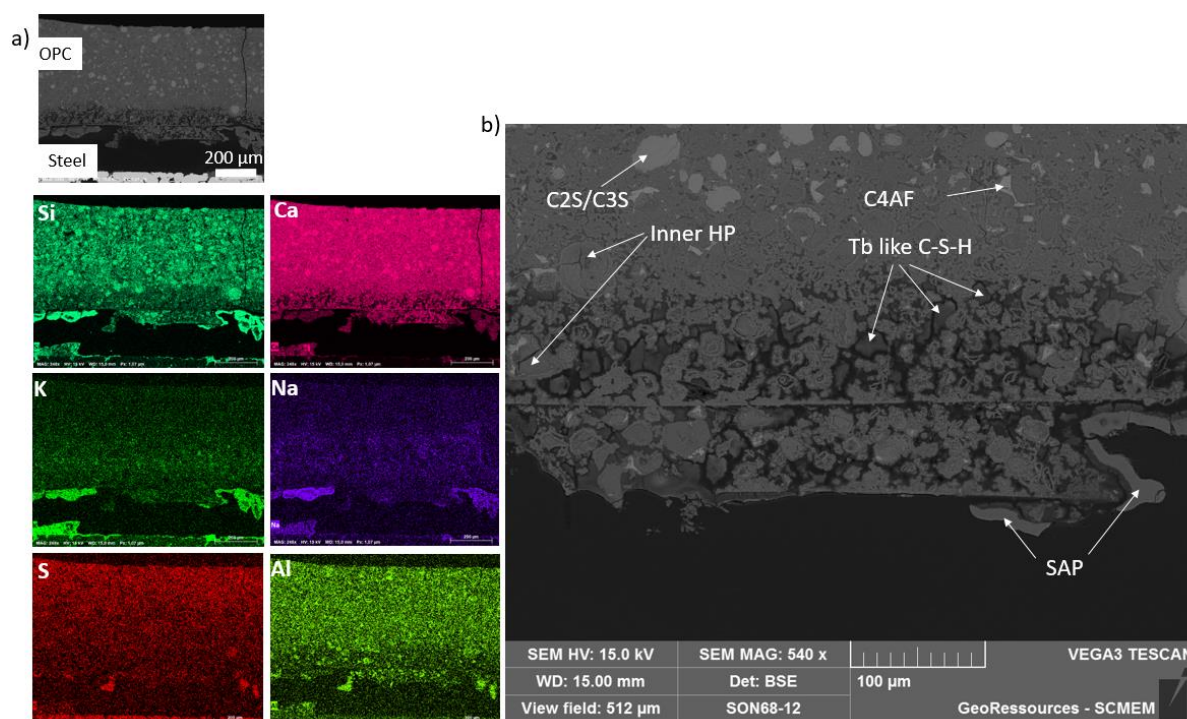


Figure 5-4 – EDXS mapping (a) and SEM micrograph (b) of the interface between SS filter and HCP in the SON68 cell. Identified phases are brownmillerite (C4AF), alite (C3S), belite (C2S), Inner hydration products (Inner HP), tobermorite like C-S-H (Tb like C-S-H), Secondary alteration products (S.A.P).

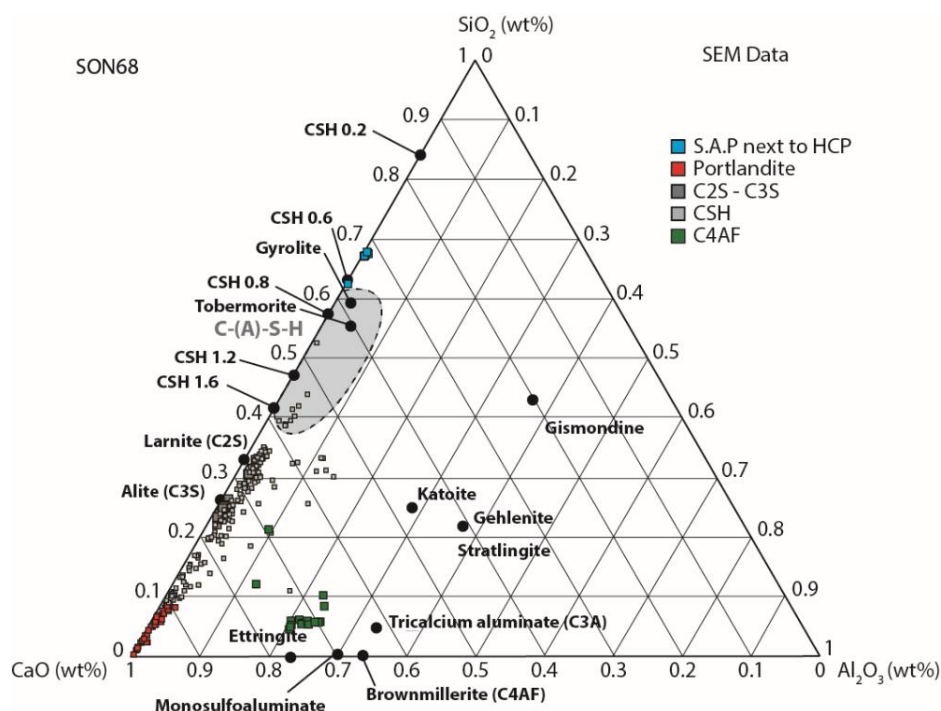


Figure 5-5 – Ternary diagram CaO- SiO₂-Al₂O₃ of SEM-EDXS analyses showing the plots of the chemical analyses of the OPC phases (C2S, C3S, portlandite, CSH, fibrous cement phase), the SON68 glass, the Secondary Alteration Phases (S.A.P.) next to glass grains (at the rim of grains), next to OPC paste. Reference minerals: tricalcium aluminate Ca₃Al₂O₆; ettringite Ca₆Al₂(SO₄)₃(OH)_{12.26}H₂O; alite Ca₃SiO₅; larnite Ca₂SiO₄; katoite Ca₃Al₂(SiO₄)_{3-x}(OH)_{4x} x=1.5-3; gehlenite Ca₂Al(AlSi)O₇; tobermorite Ca₅Si₆O₁₆(OH)₂•4(H₂O); stratlingite (Ca₂Al₂SiO₃(OH)₈:4H₂O); gismondite (Ca₂Al₄Si₄O₁₆:9H₂O); brownmillerite (Ca₂(Al,Fe³⁺)₂O₅), gyrolite NaCa₁₆Si₂₃AlO₆₀(OH)₈₋₁₄(H₂O).

5.4.2.1.2 Glass compartment

SEM-EDXS analyses were conducted in the glass compartment for both cells. The results obtained by this technique are in agreement with the data already reported in Ferrand et al. (2018). For this reason, only a short summary of the major findings are given here. However, additional characterizations were performed in this study, in order to gain information about the alteration of the SON68 and SM539 glass in alkaline medium. These additional results are presented in section 5.4.2.5.

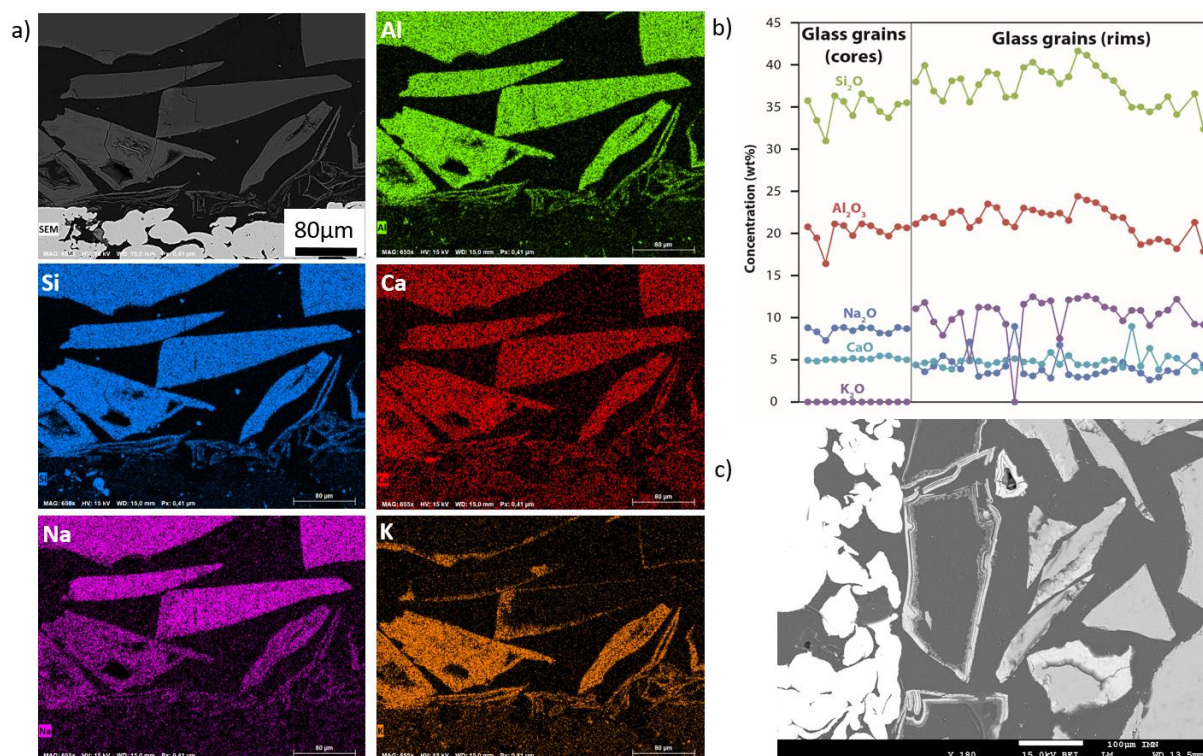


Figure 5-6 – SEM-EDXS mapping of the SM539 glass grains at the vicinity of the stainless steel filter (a) together with quantitative EDXS analyses of the rim and cores of the grains (b) and a BSE picture displaying the different alteration patterns of SM539 glass grains located at the contact with the stainless steel filters (c).

In the study of Ferrand et al. (2018), it was shown that the alteration of the glass grains was depending on their location in the glass compartment. For both cells, the glass grains located at the vicinity of the stainless steel filters (*i.e.*, in the first 300-400 μm) seem to be more altered than those further in the glass compartment. For this reason, the present study focuses on this area. However, a reminder of the observations made by Ferrand et al. (2018) further away in the glass compartment is given in this report as well.

In the SM539 cell, the glass grains located at the interface with the stainless steel filter present a multilayer alteration rim, with variable thickness (from 20 up to 35 μm). This multilayer rim is enriched in K (coming from the leaching solution) and depleted in Na, whereas Al, Si and Ca contents are close to those of the pristine glass (see Figure 5-6). These typical multi-layered structures were also observed in archaeological glass or silica glass altered in very acidic media (Dohmen et al., 2013; Verney-Carron et al., 2010) and more recently, in glass altered in alkaline media (Mann et al., 2019). It was suggested that these layers are formed by a process involving the congruent dissolution of glass network which is spatially and temporally coupled to the deposition of amorphous silica at an inwardly moving reaction interface (Geisler et al., 2015). Some grains also present hemispherical layers, enriched in K and depleted in Na, generally forming at protruding angle of the grains or at the contact between two grains. These grains are located in the whole glass compartment. The coalescence of these layers followed by their dissolution can induce the formation of pits in some glass grains (see Ferrand et al. (2018)). Other glass grains are also altered up to the core, as revealed by the K and Na mapping, or by the presence of grain relic with a surrounding multilayer rim (see Figure 5-6c).

In the SON68 cell, the glass grain alteration shows a different pattern. The alteration rim of the grains located close to the interface is much thinner than for the SM539 glass. These layers measuring only a few micrometers are enriched in K, Fe and depleted in Na and Ca (see Figure 5-7). As observed in the SM539 cell, grain showing hemispherical layers or pits are present in the whole glass compartment. Some inhomogeneously altered particles are also observed (see Figure 5-7 and Ferrand et al. (2018)).

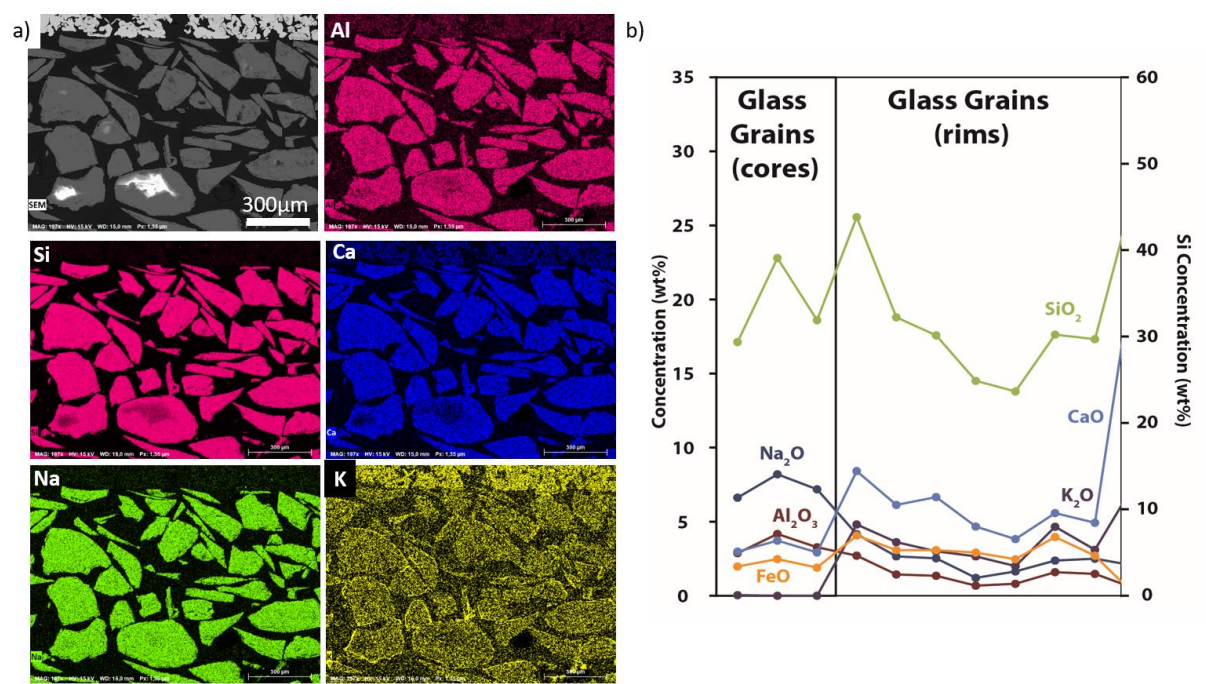


Figure 5-7 – SEM-EDXS mapping of the SON68 glass grains at the vicinity of the SS filter (a) together with quantitative EDXS analyses of the rim and cores of the grains (b) and the location of the SEM EDXS mapping (c)

5.4.2.2 XRD analysis

XRD patterns of the cement slices collected at the interface with the stainless steel filters and 2 mm further in the cement paste for both cells containing SON68 and SM539 glass are presented in Figure 5-8 and Figure 5-9. These XRD patterns are compared with the XRD pattern collected on a CIBELCOR® cement paste cured for 20 days.

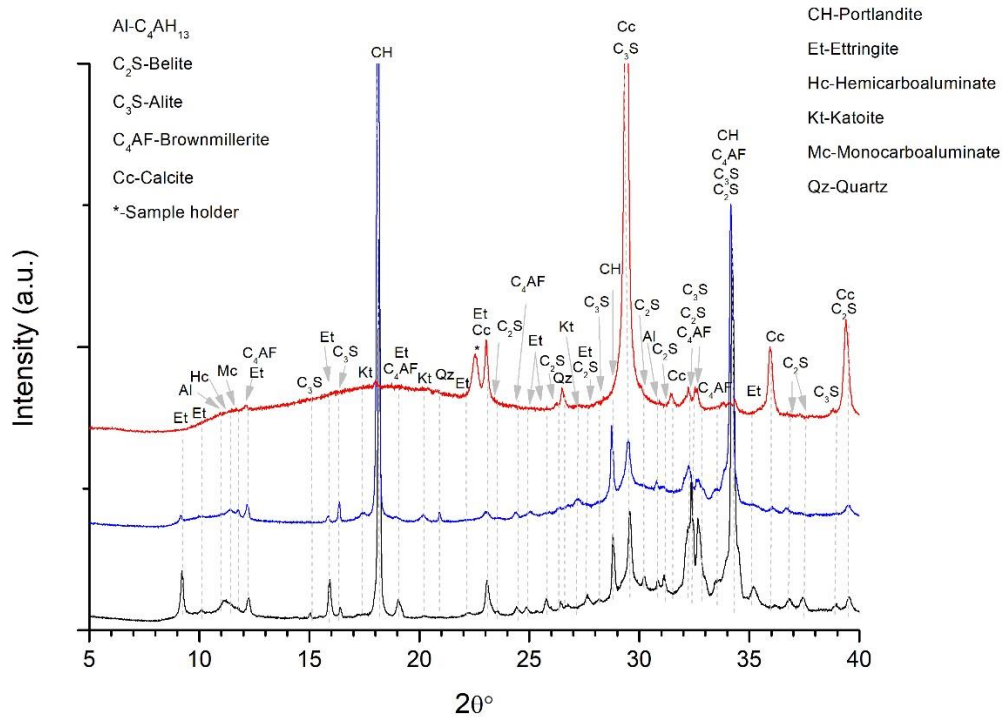


Figure 5-8 – XRD pattern of the HCP slice collected in the unaltered area (blue) and at the interface (red) with the stainless steel filter in the SM539 cell. The XRD pattern of a CIBELCOR® HCP cured for 20 days is given for comparison.

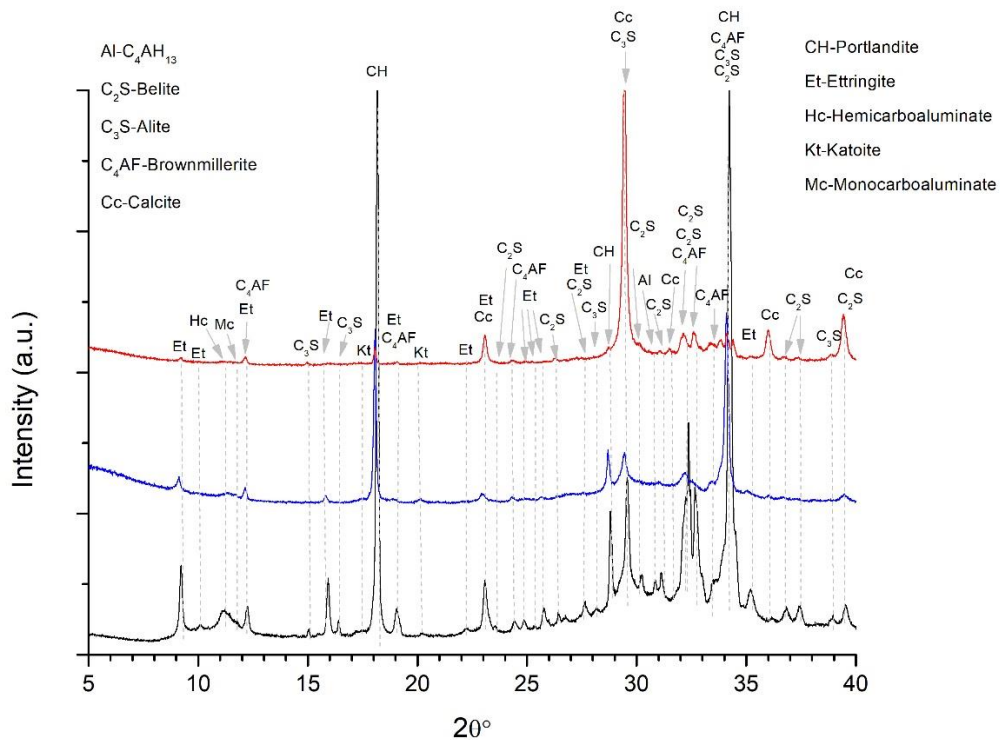


Figure 5-9 – XRD pattern of the HCP slice collected in the unaltered area (blue) and at the interface (red) with the stainless steel filter in the SON68 cell. The XRD pattern of a CIBELCOR® HCP cured for 20 days is given for comparison.

The *CIBELCOR*[®] cement paste cured for 20 days shows diffraction peaks corresponding to portlandite (CH), brownmillerite (C4AF), alite (C3S), belite (C2S), ettringite, calcite, monocarboaluminate, hemicarboaluminate and C4AH13. This latter phase is present in a very low amount and can be formed in a low gypsum containing clinker. The diffraction patterns of the cement paste slices collected at 2 mm from the interface in both cells are similar, indicating that the same phases are present. However, the intensity ratio of the peaks corresponding to the different phases are different between the *CIBELCOR*[®] cement paste cured for 20 days and the cement slices collected at 2mm from the interface. This might be due to the hydration state of the cement paste which is more advanced for the cement paste coming from the cells and thus, the UC content is higher in the cement paste cured for only 20 days. In addition, peaks arising from the presence of katoite ($Ca_3Al(SiO_4)_3$) are depicted in the unaltered HCP. This phase is an end-member of the hydrogarnet serie $Ca_3(Al_{1-x}Fe^{3+x})(SiO_4)_{3-y}(OH)_{4y}$ and thus, partial substitutions of Fe for Al and OH⁻ for Si are possible in this phase. It should be noticed that ettringite was not reported in the study of Ferrand et al. (2018), probably due to its low content in the cement paste, whereas it is observed in both cells in this study.

The diffraction patterns collected at the interface between stainless steel filter and the HCP are very different from the one collected in the unaltered HCP. For the SON68 cell, the XRD pattern is characterized by a strong intensity decrease of the peaks corresponding to portlandite and ettringite, and a strong increase of the intensity corresponding to the calcite peaks. As observed by SEM, UC phases such as brownmillerite (C4AF) and belite (C2S) are still present at the interface. However, note that the depth of analysis by this technique varies with the 2θ angle and the density of the analysed phase. For example, the theoretical depth of a layer of calcite (d = 2.7) is approximately 30 μm at 2θ = 18° (Dauzères, 2010); but due to the sample preparation, a deeper part of the sample might have been simultaneously analysed. Consequently, the XRD pattern corresponding to the interface sample might reveal phases at greater distance than the altered zone (i.e. ≈ 200 μm for the SON68 cell).

For the SM539 cell, the XRD pattern is also characterized by the dominance of calcite, the disappearing of portlandite and the presence of remaining UC phases (mainly C4AF and C2S). Ettringite peaks are not present anymore at the interface for this sample, meaning that its amount is too low to be detected or that this phase was degraded at the interface. Quartz is also present at the interface between SM539 glass and the HCP. In addition, a bulge is depicted in the XRD pattern between 2θ = 9° and 2θ = 25°. This suggests that amorphous phases precipitate at the interface with the stainless steel filter.

Note that the presence of a peak localized at 2θ ≈ 22.5° is due to the sample holder.

It is thus clearly evidenced that carbonation occurs in the altered HCP zone, even if the experiment was conducted in a decarbonized atmosphere.

As precipitates were observed in the stainless steel filter pores at the vicinity of both HCP and glass powder, XRD analyses were also conducted directly on the SS filters for both cells. Apart from calcite, no crystalline phases that precipitate in the filter pores were revealed by this technique (not shown).

5.4.2.3 TG-DSC analyses

The TG-DSC scans of the *CIBELCOR*[®] HCP cured for 20 days and of the HCP coming from the SON68 and SM539 cells are presented in Figure 5-10. The DSC scan of the young *CIBELCOR*[®] HCP reveals the presence of C-S-H, AFt (ettringite), portlandite and calcite. It was possible to quantify these two latter phases by integrating the TG curves in the zone defined by the DSC curve for each phase. The weight fraction obtained from duplicate measurements of these two phases in the young *CIBELCOR*[®] HCP are given in Table 5-7. The volumetric proportions were obtained using the measured density of the cement phases, ρ = 2.23 g/cm³ for portlandite and ρ = 2.7 g/cm³ for calcite. The portlandite content is around 18.5 vol% (12 vol%, considering 35% porosity), which is much lower than the 25 vol% predicted by the geochemical modelling. This difference can be explained by the predicted hydration state of the cement paste, because the model makes the assumption that all C3S, C3A, C4AF and almost all C2S reacted

to form hydrated cement phases. In fact, an important amount of unreacted cement phases is observed in the HCP cured for 20 days (see section 5.6.2), and thus predicted amounts of the different hydrates, including portlandite, are lower than the measured one. In addition, the presence of calcite in this HCP might come from the carbonation of the portlandite, thus lowering its amount in the HCP.

In addition, a new DSC peak is observed in the carbonate region for HCP coming from both cells, meaning that an additional carbonated phase is present in the unaltered HCP region at the end of the experiment. This newly formed carbonate might be magnesite ($MgCO_3$), as this carbonate starts to decompose at $600^\circ C$ (Li et al., 2020). Due to the proximity of the two carbonate peaks, the percentage of carbonates in both cells was determined by integrating the TG curve in the region including the two peaks. As the proportion between the two phases is not known, the density of calcite was used to determine the volumetric content of carbonate in these samples. This simplification introduces bias in the quantification. However, it was clearly evidenced that the carbonate content in the SON68 cell was approximately 2 times higher than in the SM539 cell. As already mentioned, this can be due to the sample preservation conditions. Regarding the portlandite content, it is shown that its amount is slightly higher in the HCP coming from the SM539 cell than in the young HCP (Table 5-7). On the other hand, its amount is much lower in the HCP coming from the SON68 cell, which can be explained by the partial carbonation of this phase in this cell.

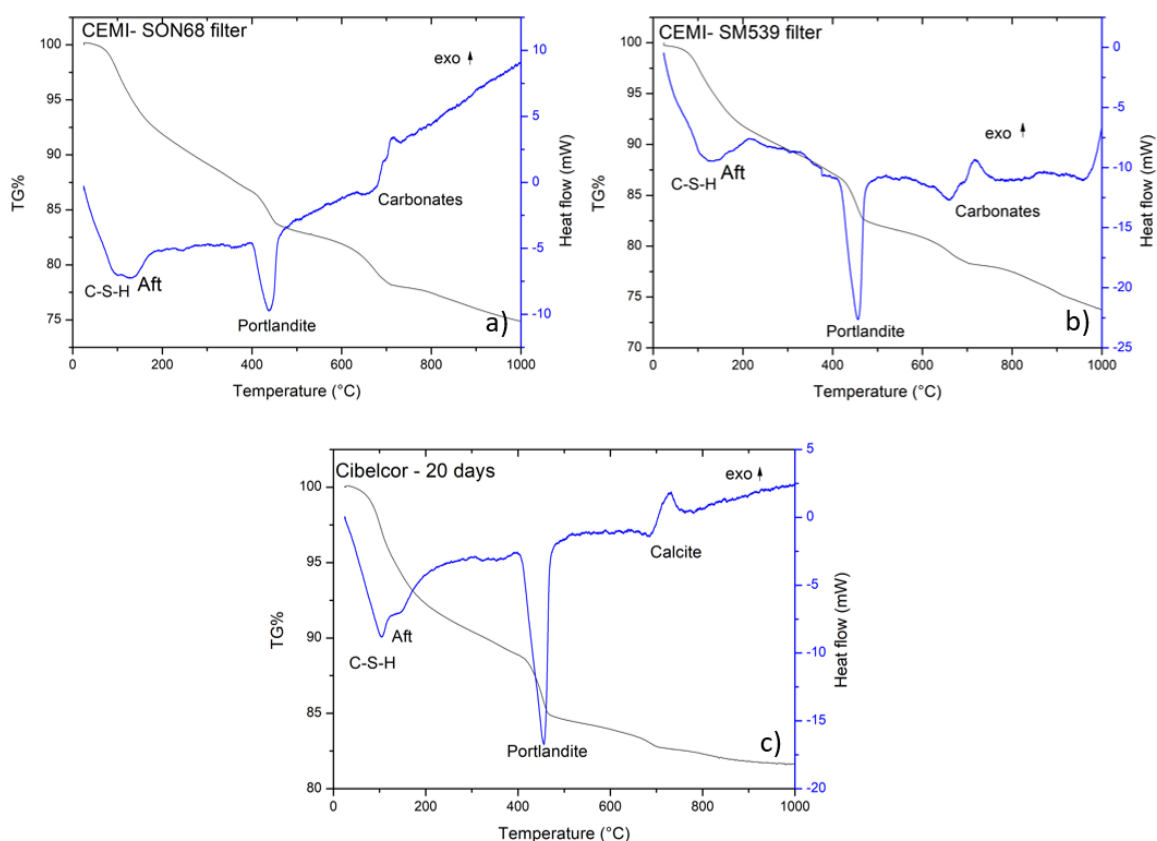


Figure 5-10 – TG-DSC measurements of the samples a) HCP-SON68 filter, b) HCP-SM539 filter and c) CIBELCOR[®] cement paste cured for 20 days. TG and DSC measurements are shown as black and blue lines respectively.

Table 5-7 – Volumetric and weight percent of portlandite and carbonates of the HCP coming from the cell SM539 and SON68 as well as a CIBELCOR[®] HCP cured for 20 days. The Loss on Ignition (LOI) values at $1000^\circ C$ are also given.

Samples	% vol portlandite	% vol carbonate	% W portlandite	% W carbonate	LOI (1000°C) %W
Cibelcor 20 days	18.5 (±2.1)	1.3 (±0.2)	15.9 (2)	1.4 (±0.2)	20.1 (±2.2)
HCP-SM539	21.2 (±0.4)	2 (±1.1)	19.1(±0.4)	2.2 (±1.1)	22.9 (±1.9)
HCP-SON68	15.1 (±0.2)	4.4 (±0.5)	14.0 (±0.2)	5.0 (±0.6)	21.8 (±3.8)

5.4.2.4 μ -Raman spectroscopy

In an attempt to characterize the phases precipitating either in the filter pores close to the glass and to the HCP or edging the HCP, μ -Raman spectra were collected in both cells. Due to the diffusion of the laser spot in the metallic part of the stainless steel filter, the Raman signal of the precipitating phases analysed in the filter pores was noisy, and thus it was not possible to characterize them properly with this technique. However, it was possible to collect Raman signal representative of the phases precipitating close to the HCP.

In the SON68 cell, the edging phase analysed by SEM was considered to be principally composed of a C-S-H phase with a low Ca/Si ratio (0.6) and enriched in alkalis (Ferrand et al., 2018). Raman spectra collected on this area are presented in Figure 5-11. The analysed spots identified as 1 and 2, clearly evidenced the presence of monocarboaluminate ($\text{Ca}_4\text{Al}_2\text{CO}_9 \cdot 11\text{H}_2\text{O}$). The main features of these spectra are the presence of bands centred at 529 cm^{-1} and 1067 cm^{-1} corresponding to the stretching vibration of the $\text{Al}(\text{OH})_6$ octahedral groups and to the stretching vibration of the CO_3^{2-} groups, respectively (Torrens-Martin et al., 2013). This AFm phase can incorporate HBO_3^{2-} ions by substitution of the CO_3^{2-} groups that are weakly bonded to the calcium ions in the interlayer. When all the CO_3^{2-} groups are substituted by HBO_3^{2-} ions, a structural change from space group P1 (Francois et al., 1998) to $\text{R}\bar{3}\text{C}$ (Champenois et al., 2012) occur, leading to local symmetry change of the anionic group. This structural feature change provokes the apparition of new vibrational modes located at 495 cm^{-1} , 550 cm^{-1} , 856 cm^{-1} , 888 cm^{-1} (ν_s B-O) and 1429 cm^{-1} , 1473 cm^{-1} (ν_{as} B-O). Such bands were not observed in the collected Raman spectra, and the observed frequency of the CO_3^{2-} group is not shifted compared to pure monocarboaluminate. However, partial substitution of CO_3^{2-} by HBO_3^{2-} , as well as SO_4^{2-} , cannot be completely excluded in this phase.

The Raman spectra of the major edging phase are also presented in Figure 5-11 and are referenced as spots 3 and 4. The spectra collected for this phase present similarities with C-S-H Raman signal. The broad bands centred around 650 cm^{-1} , with a shoulder at approximately 600 cm^{-1} and the band at approximately 1065 cm^{-1} can correspond to the bending vibration of Si-O-Si linkages and to the Si-O stretching vibrational modes both present in C-S-H (Kirkpatrick et al., 1997). The large broadening of these bands indicate that this phase is poorly crystalline or amorphous. Those spectra also present similarities with amorphous gel that precipitate during ASR (alkali silica reaction), with Ca/Si ratio of 0.33 and (Na+K)/Si ratio of 0.36 (Leemann et al., 2020). Indeed, the broad band centred near 650 cm^{-1} , with the shoulder around 600 cm^{-1} , can correspond to Q^2 and Q^3 sites bending vibrations respectively and the band centred around 1065 cm^{-1} can correspond to a combination of stretching vibration arising from Q^2 and Q^3 sites (Balachandran et al., 2017; Leemann et al., 2020). The sharp band located near 1080 cm^{-1} can be attributed to partial carbonation of this phase. As this phase seems to be partially carbonated, its Ca/Si ratio might be lower than 0.6 and can correspond to an alkali containing gel. Further characterizations are, however, needed to fully understand the nature of this precipitating phase.

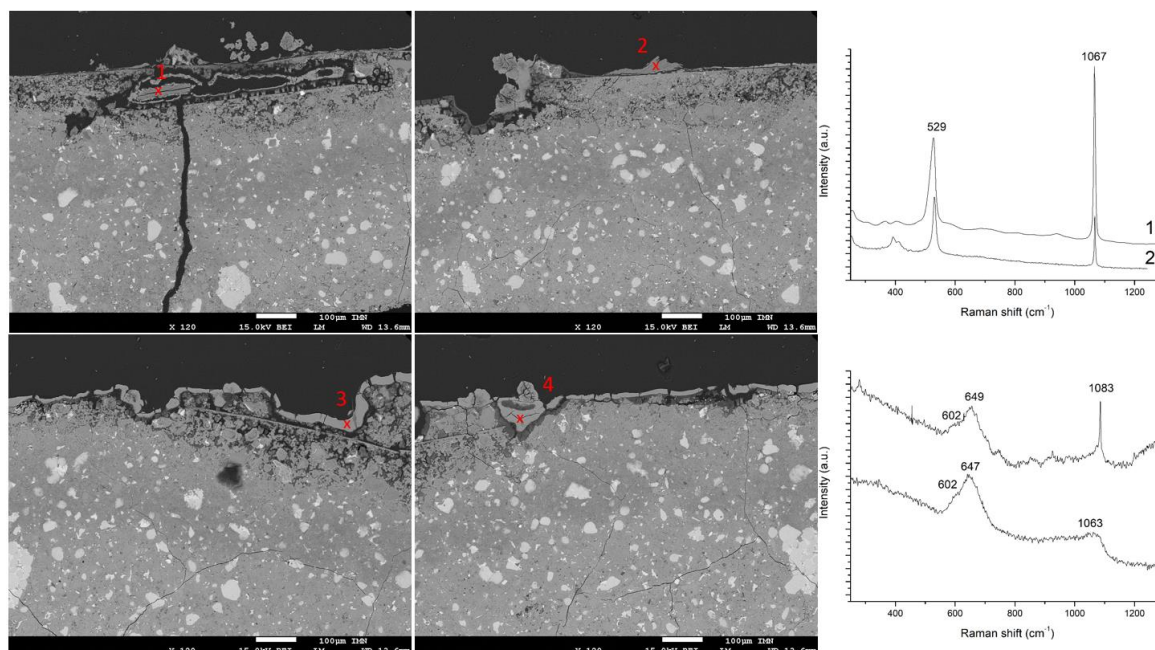


Figure 5-11 – Raman spectra of the precipitates localized at the interface between the SS filter and the HCP in the SON68 cell. The analysed spots are localized in the associated BSE-SEM picture.

Raman spectra of the edging precipitating phase observed at the interface between the HCP and the stainless steel filter in the SM539 cell are presented in Figure 5-12 (analysed spot 1). As observed by SEM, the chemical composition of this phase can correspond to a mixture of C-A-S-H phase incorporating high amount of alkalis, with a Si gel, leading to a Ca/Si ratio close to 1. The broad bands centred around 675 cm^{-1} and 1080 cm^{-1} can again correspond to the bending vibration of Si-O-Si linkages and to the Si-O stretching vibrational modes in C-(A)-S-H, or to the Q2 and Q3 sites symmetric stretching and bending vibrational modes observed in ASR gel. The sharp band located near 1080 cm^{-1} is again due to the partial carbonation of this phase. The broad bands can be shifted compared to the one observed in the SON68 cell due to the incorporation of aluminium in this phase (Ortaboy et al., 2017). However, a large background signal is depicted in the spectra collected on this phase. This background signal can be linked to the presence of a glassy phase coexisting with the C-A-S-H phase or the ASR gel. Due to the poor crystallinity of this edging phase, it is again difficult to make conclusions about its exact nature. Another edging phase was identified on a thin section and its Raman spectrum is presented in Figure 5-12 (spot 2). A high fluorescence signal combined with a sharp band located at 510 cm^{-1} are depicted in this spectrum. According to literature, this band can correspond to bending vibration of the four membered ring Si-O-Al observed in synthetic zeolite type X with the following nominal composition $3.2\text{Na}_2\text{O}:1.6\text{K}_2\text{O}:1.0\text{Al}_2\text{O}_3:2.0\text{SiO}_2:76\text{H}_2\text{O}$ (Yu et al., 2001). The high fluorescence signal can be attributed to incorporation of minor amount of Fe in this phase. Even if this phase was only observed once in the SM539 cell, the presence of K-phillipsite in the filter pores, close to the OPC was suggested in Ferrand et al. (2018). Crystallized zeolites might thus be present at the interface between SM539 glass and HCP.

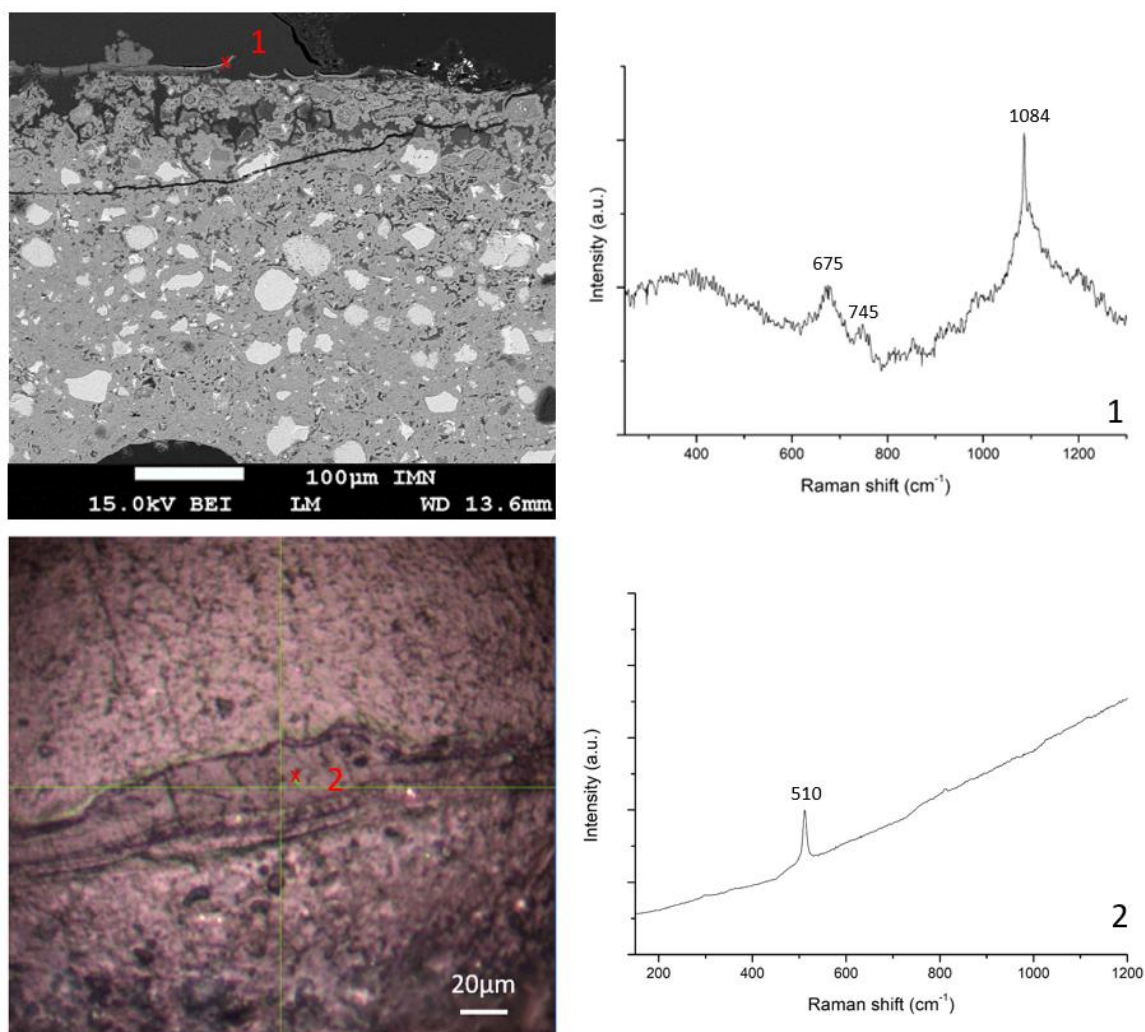


Figure 5-12 – Raman spectra of a precipitate localized at the interface between the SS filter and the HCP in the SM539 cell. The analysed spots are localized in a BSE image (spot 1) and an optical micrograph (spot 2).

Raman spectra were also collected in the glass in order to (i) characterize the structural evolution of the altered layer, and (ii) to check the presence of secondary phases precipitating at the surface of glass grains.

Despite the use of a large panel of excitation wavelengths (325 nm, 457 nm, 514 nm, 532 nm, 633 nm, 785 nm), it was not possible to avoid the overlapping of the Raman signal by fluorescence for both glasses. Thus, it was not possible to conduct glass analysis with this technique.

5.4.2.5 LA-ICP-MS

LA-ICP-MS profiles of 58 elements were collected across the HCP, in order to assess: (i) the chemical changes occurring at the interface and (ii) the diffusion of glass dissolution tracer elements across the HCP. As the HCP is a heterogeneous multiphase matrix, the line ablation mode was chosen to obtain mean profiles for each measured element. The profiles of the major constituting oxides of the HCP are given in Figure 5-13 for both cells. As no significant change in the concentration of the major constituting elements of the clinker occurs at a distance greater than 1 mm from the interface, the displayed chemical profiles are limited to this area. In both cells, the oxide contents in the unaltered HCP are very close to those of the initial clinker. As the external standard chosen for the analyses was a glass, and as the results were not corrected for loss on ignition of the HCP measurements, these results are consistent with the expected ones. Indeed, H,C and Cl cannot be measured by this technique and S was not measured in our study, thus the normalization process excludes those elements in the calculations of

the oxide percentages. However, note that the measured magnesium oxide content is a bit lower than expected. This latter observation can be partly explained by the presence of dispersed large grains of Mg-O containing phase (probably periclase transformed to magnesite) in the HCP that were not always included in the ablated lines. Also, an increase in the Mg content of glass grains was depicted for both glasses, meaning that Mg-bearing phases might have been lixiviated during the experiment followed by diffusion of Mg through the stainless steel filter.

Changes in the chemical composition of the interface are depicted. As already observed by SEM, the alkali content is higher at the interface for both cells. K and Na enrichment are noticed until approximately 300 µm in the SM539 cell and until approximately 600 µm for the SON68 cell (see Figure 5-13 and Figure 5-16). For this latter, it should be noticed that the ablated material in the first analysed line, principally consists of a low Ca/Si C-S-H phase or an ASR gel, with an important alkali uptake. This can explain the large amount of alkalis and the important decrease in the Ca/Si ratio measured for this line. In the SON68 cell, Fe and Al content seem to decrease in the first 100 µm. In this cell, the amount of remaining C4AF at the interface is very low and thus, it can explain the decrease of the content of these elements. In addition, correlation between Fe, Al and Mg profiles is depicted. The Fe and Al correlation can be related either to varying amount of ettringite in the HCP, or to the remaining presence of large grains of C4AF phase in the unaltered HCP. On the other hand, Mg is known to be present as periclase or substituted to Si in alite and belite in the clinker (Gharibi et al., 2017). As C4AF, C2S and C3S grains are locally gathered in clusters in the HCP (see Figure 5-2 as example), this correlation suggests that even after more than 900 days of hydration, these UC phases are still a source of Al, Fe and Mg. Together with the enrichment of Mg in the altered glass grains, it can also explain why hydrotalcite was not observed by XRD., whereas this phase is predicted by the geochemical model (Report D2.14, in preparation), in which all UC phases reacted to form hydrates.

In the SM539 cell, the concentration of the other major oxides (SiO₂, CaO, MgO, Fe₂O₃ and Al₂O₃) does not significantly vary at the interface between HCP and SS filter. It should be noticed that in this cell, the thin edging HCP phase, presumably composed of C-A-S-H phase with a low Ca/Si ratio, or to an ASR gel containing aluminium, was not analysed in the first ablated line. Also, the UC content still remaining at the interface for this cell is close to the UC content in the bulk cement paste, thus the Al and Fe concentration does not decrease at the interface.

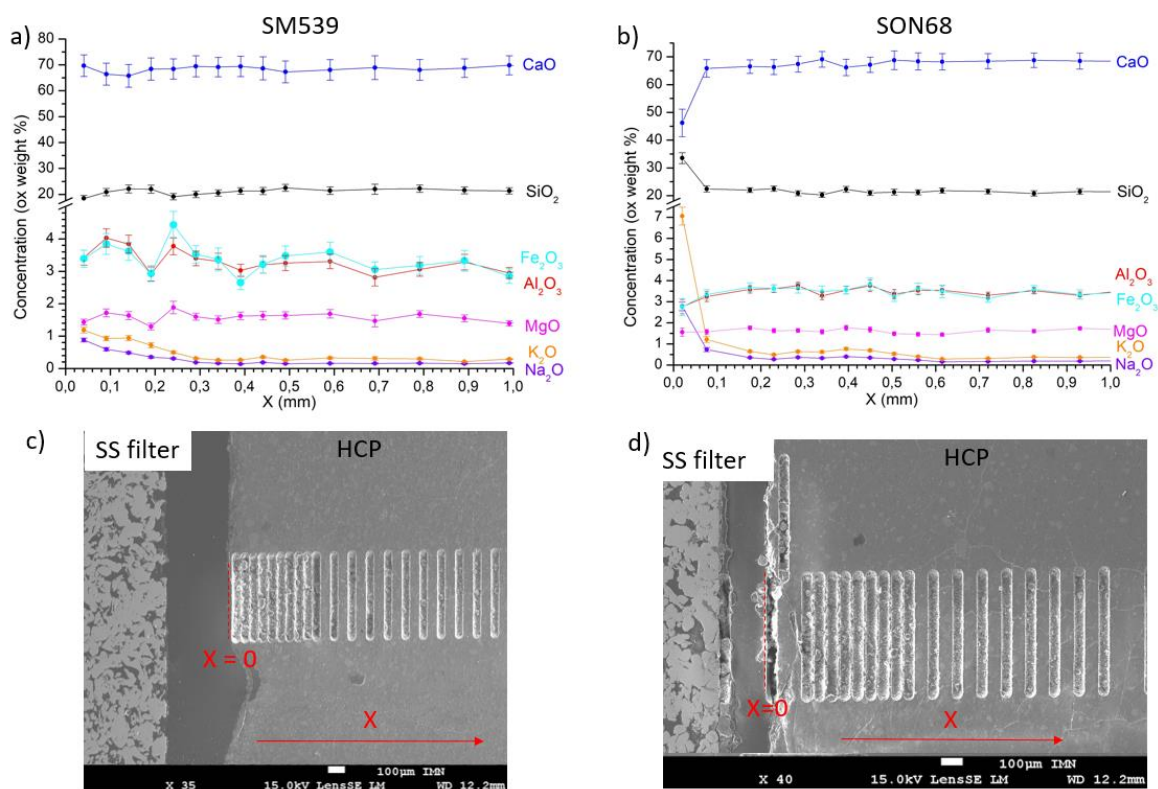


Figure 5-13 – LA-ICP-MS profile measurements of major constituting elements across the hydrated cement paste for the SM539 cell (a) and for the SON68 cell as well as the SEM SE pictures of the sample SM539 (c) and SON68 (d) after laser ablation. The standard deviations are given at 95% confidence interval. Dots are connected for a better visualization.

LA-ICP-MS profiles of B and Li were acquired across the HCP for both cells (Figure 5-14 and Figure 5-15). It is clearly evidenced from the measurements that boron and lithium, coming from glass dissolution, diffuse across the HCP. Interestingly, the boron and lithium diffusion profiles are similar in the two different cells, which was not the case in the experiment without stainless steel filters (Ferrand et al., 2018). However, as the lixiviated amount of boron in the SM539 cell was more than two times higher than in the SON68 cell (see section 5.5), the boron amount that precipitates at the interface between stainless steel filter and HCP is much higher in the SM539 cell.

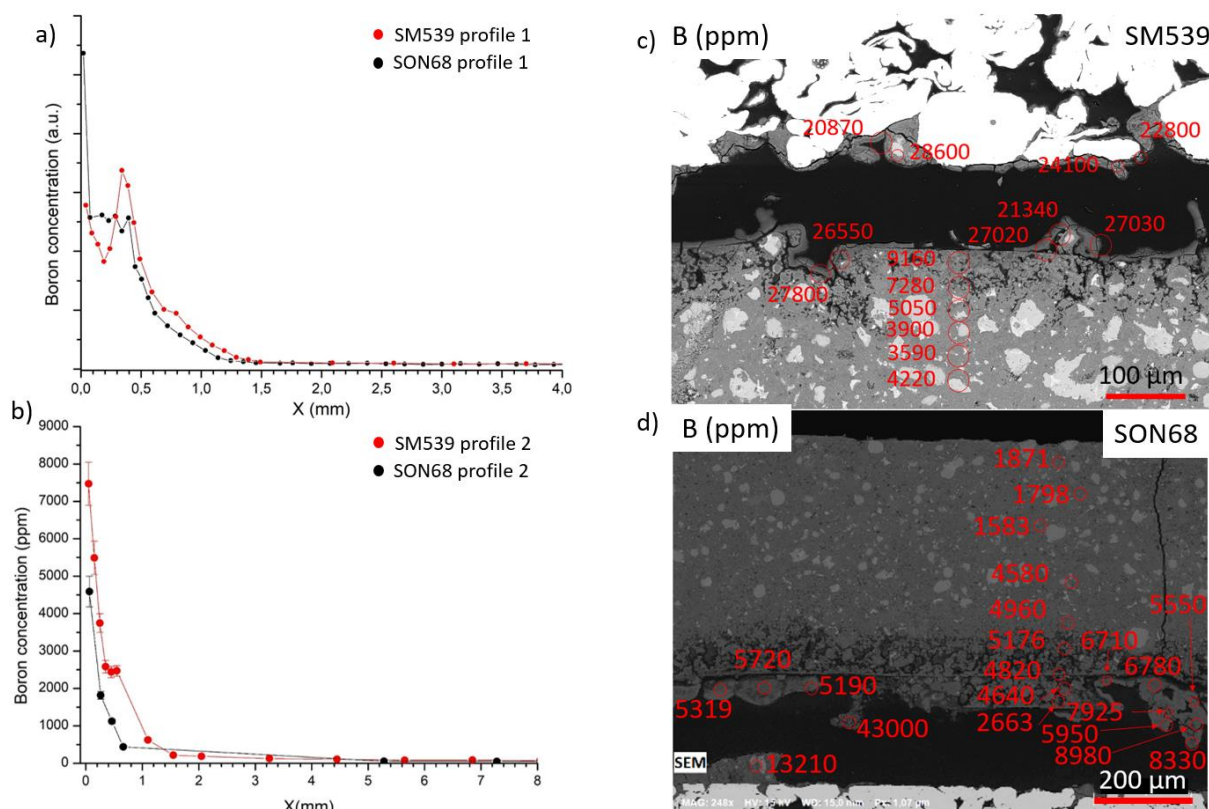


Figure 5-14 – Line mode LA-ICP-MS profile measurements of boron across the cement paste for the SM539 and SON68 cell (a) and (b) and spot mode LA-ICP-MS measurements of boron in the cell SM539 (c) and SON68 (d). Profiles 1 are only qualitative and correspond to the same profile as the major oxides and profile 2 correspond to profiles acquired in another cross section. The standard deviations are given at 95% confidence interval. Dots are connected for a better visualization.

Boron diffusion: Boron is considered as a good tracer of glass dissolution in a wide range of pH values (acidic to low alkaline) due to its good mobility and because this element is not retained in the glass alteration layer (Suzuki-Muresan et al., 2018). The aqueous boron chemistry is dominated by the constant dissociation of boric acid following the equation:



In highly alkaline media, the tetrahedral ion $B(OH)_4^-$ will be the dominating species and thus, this ion will diffuse in the cement paste.

In both cells, it was shown that boron is rapidly retained in the HCP, as it diffuses over approximately 1.25 mm in the SON68 cell and 1.5 mm in the SM539 cell. This can be partly explained by the steric hindrance of this tetrahedral ion, as well as its negative electrostatic charge interacting with the positive charge of the cement phases (Ferrand et al., 2018). Moreover, a low retention factor of 14 L.Kg^{-1} was obtained in geochemical modelling where glass powders were altered in the presence of HCP powders (Ferrand et al., 2013). This can explain the rapid retention of boron in the HCP. However, partial substitution of anionic species by B-bearing entities in HP and/or precipitation of B-bearing phases are necessary to explain the observed profiles. Indeed, boron can form solid solution with AFt and AFm phase, as mentioned in section 5.4.2.4 and in Ferrand et al. (2018) or with cations in porewater solution such as Na and Ca, to form aqueous complex (e.g. NaB(OH)_4 , CaB(OH)_4^+). Furthermore, boron might be retained in the structure of C-S-H. To the best of our knowledge, there are no study about incorporation of boron in C-S-H phase. However, Nozawa et al. (2018) observed co-precipitation of boron with silicon and magnesium in M-S-H, in the presence of magnesium oxide, amorphous silica and

$B(OH)_3$ solutions. In their study, they show that approximately 50% of boron is retained in the precipitates after 18 days of interaction, with an initial concentration of 100 ppm of boron. They suggest that boron can be either isomorphically substituted to the tetrahedral Si or incorporated in triangular planar form in the interlayer of the M-S-H structure.

In both cells, anomalous boron concentration fluctuations are depicted in the LA-ICP-MS spot profiles and in the qualitative profiles⁴ (Figure 5-14). These fluctuations reflect the preferential incorporation of boron in specific cement phases (AFt, AFm), or the precipitation of B-bearing phases (e.g. $NaBO_2$, $Na_2(B_4O_5(OH)_4) \cdot 8 H_2O$, $Ca_2B_6O_{11} \cdot 5 H_2O$). Indeed, Ca borates are suspected to precipitate in such alkaline environment (Utton et al., 2013). However, they were not observed with the different characterization methods employed for this study. Although such phases were not detected, they might be intimately mixed with other cement phases, thus limiting their detection by conventional techniques.

However, the localized LA-ICP-MS analyses allows a better understanding of the speciation of boron in the HCP. Indeed, in the SM539 cell, the B concentration is much higher in the S.A.P, either precipitating in the stainless steel filter or edging the HCP than in the porous altered area. This observation suggests that boron is highly retained in the mixture of C-A-S-H/Al containing ASR gel and Si glass. In the SON68 cell, the highest boron concentration value (43000 ppm) is localized in an area enriched in sulphur and aluminium (see Figure 5-4a and Figure 5-14d) suggesting a partial substitution of boron in AFt and or AFm phases. Such phases were observed at the interface by SEM and μ -Raman only for this cell. The ASR gel edging the HCP also retains boron in a lesser extent in the SON68 cell.

Lithium diffusion: In glass leaching tests in the presence of cement, lithium could be a more suitable tracer of glass dissolution than boron, as the high amount of Ca in the HCP environment can favour, for instance, the precipitation of calcium borate phase (Suzuki-Muresan et al., 2018). Indeed, the profiles of Li show that contrary to boron, lithium is less retained and diffuses much further in the cement paste, i.e. over a distance of at least 7 mm for both cells. This behaviour was already observed in the cells without stainless steel filters by means of LIBS measurements. However, the Li profiles seem to be made of two regions,. This is particularly evidenced for the sample from the SON68 cell, in which a first drop in the Li concentration is depicted between 0 and 0.6 mm, and then a linear decrease is observed (Figure 5-15). Also, a correlation between Li and other alkalis (Na, K, Cs) can be highlighted (see Figure 5-16). Indeed, a slight increase in the K, Na, Cs and Li concentration is depicted between 0.2 and 0.6 mm. This may suggest that Li, K, Na and Cs may interact with the same phases.

Indeed, these four elements can be incorporated in different amount in the C-S-H or C-A-S-H phase. It was notably demonstrated that K and Na can be incorporated into the C-S-H structure in a roughly equal amount, whereas Li can be incorporated in a much greater extent (Mitchell et al., 2007; Stade, 1989). This difference in incorporation can be based on structural ground, as Li can adopt tetrahedral or octahedral environment in silicates, whereas Na and K, which have a higher ionic radii, generally occupy sites with at least, a 5-five coordination state (Mitchell et al., 2007). Stade (1989) also demonstrates that the alkali incorporation is higher with decreasing C/S ratio and with increasing alkali concentration. Note that a difference in diffusivity between the alkalis is linked to the size and the charge density of these cations. Indeed, higher charge density induces stronger electrostatic interactions with the surface and higher solvation shell radii induces lower retention For instance, it was recently shown by atomistic simulation that this ion diffuses much more rapidly in C-S-H than Na with a difference of two orders of magnitude in the diffusion coefficients (Duque-Redondo et al., 2018). These authors also showed that the alkali diffusivity is drastically reduced in C-A-S-H compared to C-S-H, due to the increase of the electrostatic interactions induced by the aliovalent substitution of Si by Al in the structure. However,

⁴ Contrary to profiles 2, the element concentrations of profiles 1 (SM539 and SON68 cells) were calculated using an unpolished NIST610 standard sample. A significant underestimation of the boron concentration was found using such unpolished standard by measuring the boron concentration in a pristine SON68 standard. Thus profile 1 are only qualitative profiles for boron.

some experimental data showed that the effect of silicon substitution by aluminium on alkali retention have no significant effect (L'Hopital et al., 2016b).

It should be noticed that literature about interaction between these alkali elements in C-S-H is lacking and it would be beneficial to know if the incorporation of potassium and/or sodium enhance or decrease Li sorption capacity of the C-S-H phases. Nevertheless, the “bimodal diffusion regime” of Li can be explained by mineralogical changes at the interface. Indeed, the spot analyses revealed a large drop in the Li concentration from the first analyses in the unaltered area for both cells (see Figure 5-15b and c).

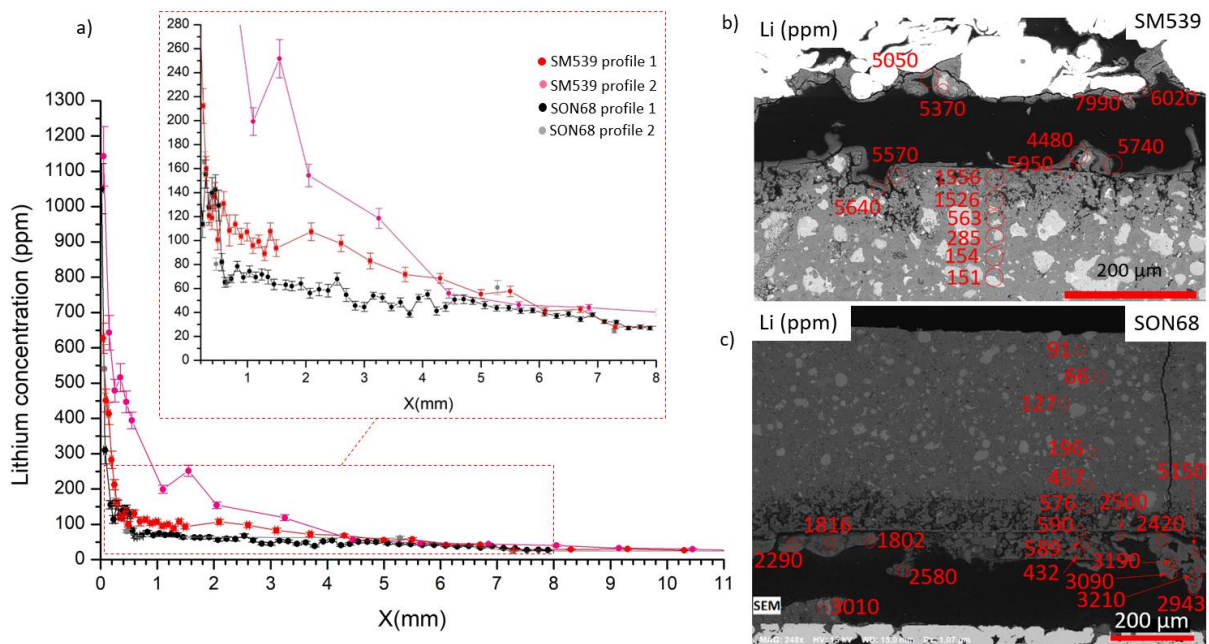


Figure 5-15 – Line mode LA-ICP-MS profile measurements of lithium across the cement paste for the SM539 and SON68 cell (a) and spot mode LA-ICP-MS measurements of lithium in the cell SM539 (b) and SON68 (c) . Profiles 1 are corresponding to the same profiles as the major constituent oxide ones and profile 2 correspond to a profile acquired in another cross section. The standard deviations are given at 95% confidence interval. Dots are connected for a better visualization.

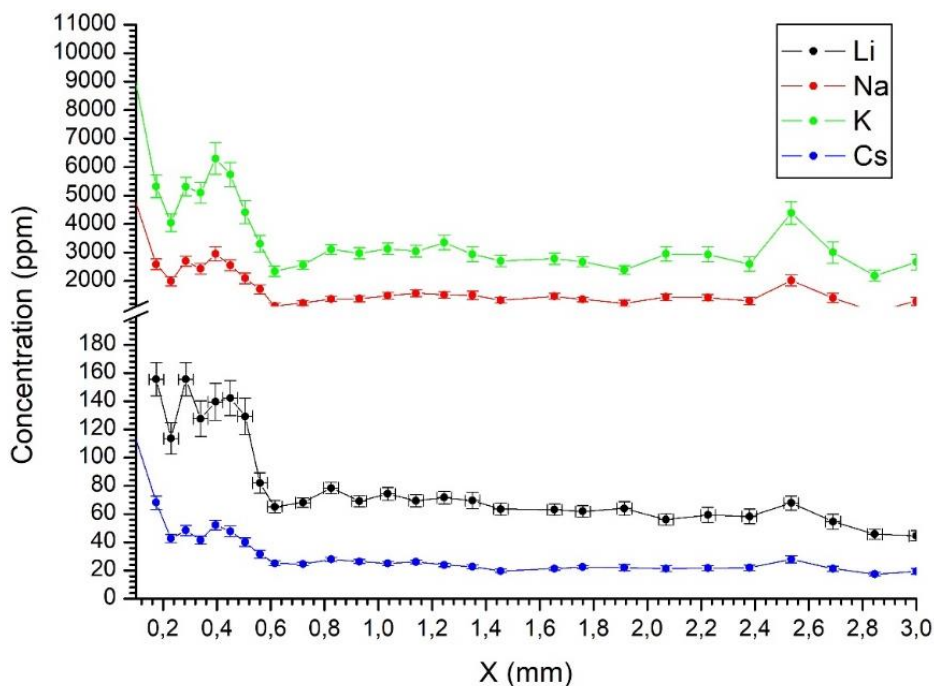


Figure 5-16 – LA-ICP-MS alkali profiles across the cement paste for the SON68 cell. Dots are connected for a better visualization. The standard deviations are given at 95% confidence interval. First points of the profiles are not presented for clarity reasons

Glass compartment In addition to the SEM-EDXS analyses collected on the glass grains at close contact with the SS filters, LA-ICP-MS analyses in spot mode were conducted. Spot size diameter of 60, 20 and 10 μm were adapted to the analysed area.

In addition to the Na depletion observed by SEM, the analyses of the altered layers of the SM539 glass grains reveal their strong depletion in Li and B. The core composition of these grains are, however, very close to the pristine glass one. The Li and B depletions are expected because these elements are among the first to solubilize during glass alteration (Gin et al., 2001; Suzuki-Muresan et al., 2018).

In the SON68 cell, the K enriched rim layer was too thin to be analysed by this technique. Consequently, only the core of the grains were analysed. A strong depletion of boron (from 4.3 wt% in the pristine glass to approximately 3.5 wt % in the altered grains) as well as a Li depletion (from 0.9 wt% in the pristine glass to approximately 0.8 wt% in the altered grains) are depicted. This latter observation suggests that the glass grains localized at the vicinity of the stainless steel filters are altered up to their core. This phenomenon was not taken into account in the calculation of the glass dissolution rate from the measurement of the altered thickness layer in the previous study of Ferrand et al. (2018). However, these measurements were only performed at the vicinity of the stainless steel filter where glass alteration might have been more extensive than in the rest of the compartment.

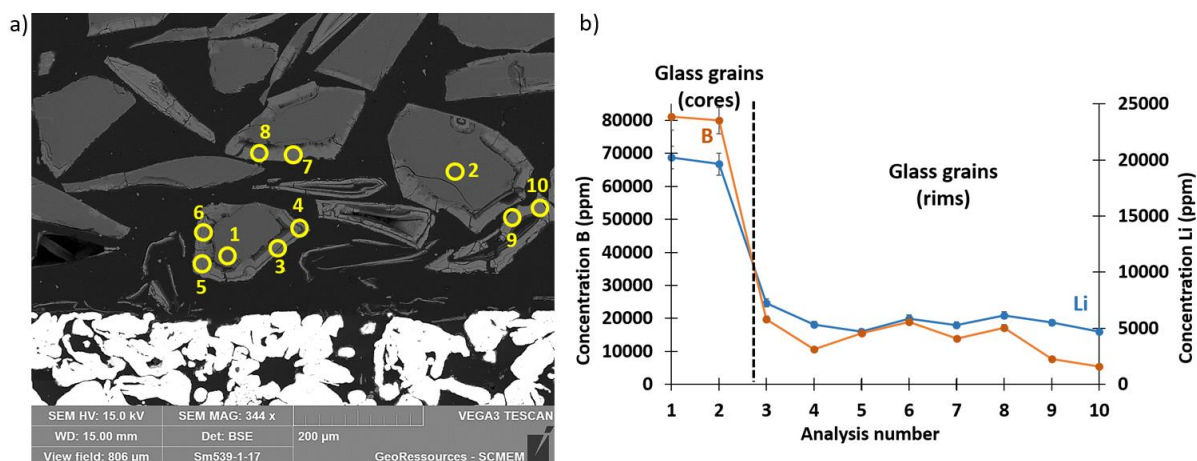


Figure 5-17 – SEM-BSE image of LA-ICP-MS localized spot analyses of SM539 glass grains at the interface with SS filter (a) along with their B and Li content.

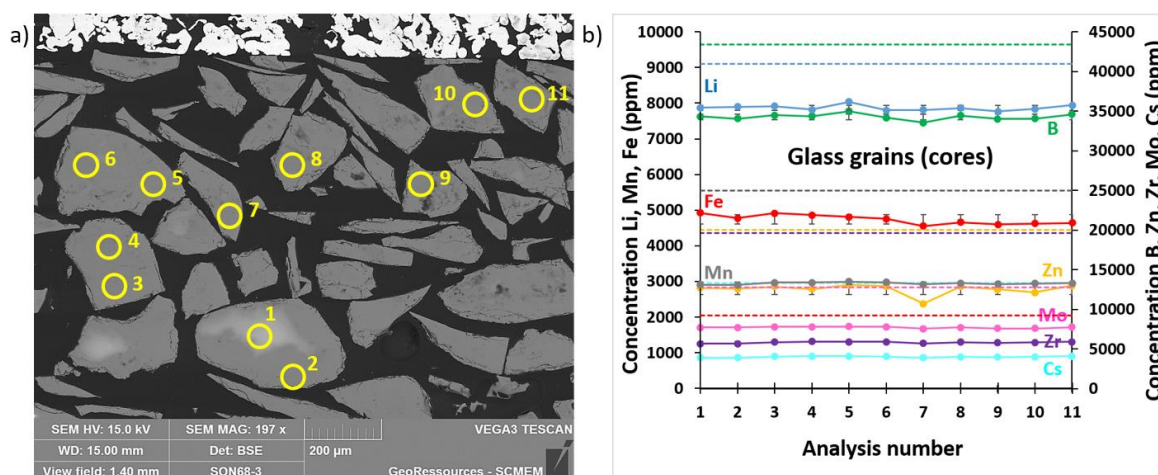


Figure 5-18 – SEM-BSE image of LA-ICP-MS localized spot analyses of SON68 glass grains at the interface with SS filter along with their chemical composition.

5.5 Analysis of the leaching solution

5.5.1 Methods, operating conditions and uncertainties

Following measurements were done:

- pH measurement (InLab® Mettler Toledo microelectrode),
- Inductively Coupled Plasma-Optical Emission Spectrometry (ICP-OES),
- Inductively Coupled Plasma-Mass Spectrometry (ICP-MS),
- Ionic Chromatography (IC)

The uncertainty at 95% confidence interval on the pH measurement was ± 0.2 . The collected solutions were diluted with 2 % HNO₃ to determine their chemical composition by ICP-OES and ICP-MS (ThermoScientific Iris Intrepid II dualview and ThermoScientific Xseries2). To perform IC (ThermoScientific Dionex DX600) the solutions were diluted with Milli-Q® water. For both analytical techniques ICP and IC, the uncertainty at 95% confidence interval was $\pm 10\%$.

5.5.2 Results

Table 5-8 gives the pH values measured at room temperature in the integrated tests. The pH was quite constant in the cement plug, *i.e.* from 12.5 at 52.5 mm, whereas a slightly lower pH is observed in the glass compartment at 72.5 mm, probably due to the release of boric and silicic acid from the glass.

Table 5-8 – pH values measured at room temperature in the integrated tests.

Duration days	Distance mm	pH SM539 glass	Duration days	Distance mm	pH SON68 glass
180	12.5	13.87	182	12.5	13.63
	27.5	13.9		27.5	13.69
	42.5	13.9		42.5	13.7
	57.5	13.86		57.5	13.68
	72.5	13.7		72.5	13.5
365	12.5	13.88	383	12.5	13.85
	27.5	13.89		27.5	13.88
	42.5	13.92		42.5	13.88
	57.5	13.87		57.5	13.92
	72.5	13.59		72.5	13.69
524	12.5	13.55	586	12.5	13.54
	27.5	13.57		27.5	13.56
	42.5	13.59		42.5	
	57.5	13.51		57.5	
	72.5	13.3		72.5	
707	12.5	13.65	769	12.5	13.66
	27.5	13.66		27.5	13.67
	42.5	13.67		42.5	13.67
	57.5	13.62		57.5	13.61
	72.5	13.38		72.5	13.34
898	12.5	13.65	960	12.5	13.63
	27.5	13.66		27.5	13.64
	42.5	13.67		42.5	13.71
	57.5	13.62		57.5	13.64
	72.5	13.31		72.5	13.31

Elemental concentrations measured by ICP and Cl⁻ and SO₄²⁻ concentrations measured by IC are indicated in Table 5-9.

Table 5-9 – Element concentrations in mg/L in the integrated tests

SON68 glass															
Time days	Distance mm	Al mg/L	B mg/L	Ca mg/L	Fe mg/L	K mg/L	Li mg/L	Mg mg/L	Mo mg/L	Na mg/L	Si mg/L	Sr mg/L	Cs mg/L	Cl- mg/L	SO42- mg/L
182	12.5	1.3	6.2	56	0.25	13260	6.2	0.12	0.19	3330	36	13	0.81	8.5	644
	27.5	0.91	5.9	64	0.23	14099	6.8	0.12	0.21	3495	2.9	19	2.9	7.2	1040
	42.5	1.1	6.1	61	0.25	13477	6.1	0.12	0.18	3431	19	16	1.9	5.1	946
	57.5	0.84	9.0	68	0.24	12633	16	0.12	5.3	3519	9.0	15	29	6.5	917
	72.5	11	571	1.2	0.30	13161	91	0.12	144	4217	2064	0.12	118	8.8	607
383	12.5	0.91	3.6	66	0.14	13938	6.0	0.07	0.13	3186	33	17	2.6	17	1013
	27.5	0.91	3.6	66	0.14	13983	6.0	0.07	0.13	3196	33	17	2.6	17	1005
	42.5	1.1	3.1	70	0.13	14834	5.8	0.06	0.12	3344	16	16	3.2	8.9	1114
	57.5	0.97	3.6	77	0.14	12306	21	0.07	1.3	3177	7.9	18	38	5.9	887
	72.5	5.9	1057	0.95	0.55	12939	164	0.09	146	4629	3535	0.11	164	13	576
769	12.5	1.2	2.9	61	0.11	13769	5.2	0.06	0.14	3184	13	15	1.5	22	915
	27.5	1.0	2.8	60	0.11	14388	6.5	0.06	0.12	3273	1.9	17	2.3	7.8	1016
	42.5	1.3	2.9	58	0.12	14173	4.6	0.06	0.18	3240	2.8	15	2.0	6.1	949
	57.5	1.0	3.0	67	0.12	11917	21	0.06	1.2	3069	2.8	18	26	8.0	840
	72.5	3.7	1313	2.1	1.5	12847	211	0.06	403	5567	3940	0.20	188	16	545
960	12.5	0.77	3.6	73	0.14	13644	8.0	0.07	0.12	3411	15	16	1.9	34	930
	27.5	0.60	3.6	65	0.14	14248	9.4	0.07	0.09	3419	2.0	16	2.8	27	1046
	42.5	0.72	3.6	65	0.14	14021	7.2	0.07	0.12	3434	3.1	15	2.8	23	1022
	57.5	0.92	3.6	83	0.14	11303	31	0.07	0.88	3233	3.2	18	34	29	761
	72.5	3.9	1649	1.8	1.7	12726	260	0.07	497	6103	4194	0.12	171	48	541
SM539 glass															
Time days	Distance mm	Al mg/L	B mg/L	Ca mg/L	Fe mg/L	K mg/L	Li mg/L	Mg mg/L	Mo mg/L	Na mg/L	Si mg/L	Sr mg/L	Cs mg/L	Cl- mg/L	SO42- mg/L
180	12.5	0.70	2.9	64	0.12	13633	4.1	0.06	0.10	3249	12	17	1.7	18	1343
	27.5	0.84	2.9	65	0.12	14124	5.5	0.06	0.12	3315	18	17	2.2	12	1061
	42.5	0.70	2.9	63	0.12	13971	2.9	0.06	0.26	3260	9.2	13	0.80	7.4	911
	57.5	0.18	175	84	0.12	12569	96	0.06	0.57	3625	4.0	15	1.1	9.5	1418
	72.5	101	1527	2.7	0.21	12040	297	0.06	3.2	4434	485	0.07	0.58	19	649
365	12.5	0.58	2.9	61	0.12	13019	5.5	0.06	0.16	3269	10	16	2.1	29	1146
	27.5	0.83	2.7	62	0.11	13147	7.2	0.05	0.14	3381	25	16	2.8	25	1105
	42.5	0.80	2.7	47	0.11	14275	4.4	0.05	0.24	3432	16	14	1.5	12	1142
	57.5	0.25	53	20	0.11	11978	101	0.06	0.33	3593	3.4	13	1.7	14	1588
	72.5	101	2076	2.4	0.17	10548	421	0.06	4.0	4805	392	0.06	0.56	19	640
707	12.5	1.2	2.8	58	0.11	14198	6.0	0.06	0.14	3124	3.5	17	1.7	24	1017
	27.5	1.1	2.9	60	0.12	13964	7.0	0.06	0.10	3258	16	17	2.0	9.5	992
	42.5	1.2	2.8	58	0.11	14479	4.8	0.06	0.17	3236	5.4	15	1.2	31	1008
	57.5	0.71	36	65	0.12	12960	52	0.06	0.21	3152	2.2	15	0.88	8.3	1169
	72.5	86	2682	3.3	0.14	11096	525	0.06	4.8	4913	322	0.08	0.53	14	661
898	12.5	0.66	3.6	62	0.14	13745	8.3	0.07	0.09	3379	4.1	17	2.0	23	1019
	27.5	0.65	3.6	66	0.14	13639	9.4	0.07	0.07	3523	18	17	2.4	16	997
	42.5	0.74	3.6	65	0.14	14549	7.1	0.07	0.11	3566	6.5	16	1.6	7.7	1050
	57.5												1.2	53	1233
	72.5	82	3601	4.4	0.22	11126	677	0.09	5.6	5473	288	0.09	0.45	113	648

The boron concentration measured in the boreholes of the cement paste was very low and constant around 3 – 9 mg/L, whereas it increased strongly in the glass compartment: up to 1650 mg/L for SON68 glass, and up to 3600 mg/L for SM539 glass.

For SON68 glass, high increasing silicon concentrations were measured in the glass compartment, reaching a value of ~4200 mg/L after 960 days but probably increasing further afterwards, suggesting that the silicon concentration in solution was not (yet) limited by solubility. For SM539 glass, silicon concentration first increased up to ~500 mg/L, and then decreased down to ~300 mg/L, indicating Si incorporation into secondary phases.

The Al concentration in the glass compartment first increased and then decreased: maximum concentrations of ~110 and 10 mg/L were measured for SON68 and SM539 glasses, respectively.

A low Ca concentration of 1 – 5 mg/L was measured in the glass compartment whereas in the cement plug, Ca concentrations were quite constant around 60 mg/L.

The Na concentration increased in the glass compartment whereas it was rather constant in the cement plug, *i.e.* close to the initial value of 3200 mg/L in YCWCa. In contrast, the evolution of the K concentration showed a slight decrease in the glass compartment as well as in the cement borehole close to the glass.

Based on the B concentration measured in the glass compartment (*i.e.* at 72.5 mm), bulk or overall dissolution rates were calculated (Table 5-10). These rates are similar to the dissolution rates that were measured in another experimental setup, where glass powder was confined between stainless steel filters and leached in YCWCa without cement, but lower than the dissolution rate in cement water with dispersed glass particles without cement or with dispersed cement particles (Table 5-10). The dispersion of the glass and cement particles increases the reactive surface area and thus accelerates the interaction.

This shows that the presence of the cement can increase the dissolution rate in YCWCa, but only if there is good contact between glass and cement. When a cement plug is used, the small reactive surface area and transport processes slow down the interaction with the glass.

Table 5-10 – Glass dissolution rates in $g.m^{-2}.d^{-1}$ determined from different leaching tests in YCWCa; the uncertainty at 2 sigma is <15%.

Leaching Solution: YCWCa	SM539 glass	SON68 glass
Integrated tests	0.0015	0.001
Unconfined glass, 30 °C (no cement)	0.0065	0.0085
Confined glass, 30 °C (no cement)	0.00052	0.00057
Dispersed glass and cement powder, 30 °C	0.021 - 0.048	0.0032 - 0.0094

5.6 Other tests and characterizations

5.6.1 Porosity and density measurements of HCP

After dismantling of the cells, the porosity of the unaltered cement paste was determined by water porosity measurement. In parallel, a CIBELCOR® cement paste with W/C = 0.4 and cured for 20 days was prepared to assess the porosity of the HCP at the beginning of the experiment. Table 5-11 presents the results of the water porosity measurement for the different samples. The porosity of the CIBELCOR® HCP cured for 20 days, measured on 4 different samples is around 37%. This value is consistent with water porosity measurements on similar HCP (Lalan, 2016). The difference between predicted and measured porosity might come from the partial degradation of cement hydrates during the drying of the samples, even if the selected drying temperature was low (*i.e.* 60°C) to avoid this phenomenon.

The porosity of the HCP coming from both cells is much lower than the initial value measured on the young HCP. This can be attributed to the hydration state and to the carbonation of the HCP, which both favour porosity clogging. Interestingly, lower porosity is depicted for the SON68 cell compared to the SM539 cell. In this cell, the carbonate content is higher than in the other one and the UC content is lower (see section 5.6.2), which explains these differences.

Unfortunately, it was not possible to assess the porosity change at the interface between HCP and stainless steel filter with this technique, due to the very low thickness of the altered HCP in the cells (<200 µm). However coarse porosity change in the HCP was assessed by SEM (see section 5.6.2).

Table 5-11 – Water porosity measurement of the cement paste samples collected in the SM539 and SON68 with filter cells and of the CIBELCOR® cement paste cured for 20 days.

Sample id	CIBELCOR® 20days	HCP SM539	HCP SON68
Porosity	36.6 (± 1.4)	25.9 (± 0.3)	21.3 (± 2.4)
Density (saturated HCP)	2.01 (± 0.04)	2.09 (± 0.01)	2.12 (± 0.04)

Density (unsaturated HCP)	1.65 (± 0.05)	1.83 (± 0.01)	1.91 (± 0.07)
Density of cement phases	2.60 (± 0.03)	2.47 (± 0.01)	2.42 (± 0.02)

The density of the HCP, collected far from the interface and of the CIBELCOR® HCP cured for 20 days are also given in Table 5-11. The densities for the CIBELCOR® HCP cured for 20 days are not far from the modelled values of 1.78 kg/m³ for unsaturated HCP and 2.69 kg/m³ for the cement phases. The slight difference in the unsaturated value is due to the porosity difference between measured and modelled value. However, as the porosity strongly decreases in the HCP collected in the two cells, the density of unsaturated HCP strongly increases. The observed decreasing value of the cement phase density in both cells is due to the lowering content in UC, which has a higher density than the hydrated phases (see Table 5-11).

5.6.2 SEM grey analyses

In addition to the EDXS mapping/analyses, grey level analyses were conducted in the two cells, in both the unaltered and altered area. Such analyses were performed in order to obtain more quantitative data on the distribution of the mineralogical phases and the evolution of the microstructure of the HCP at the interface with the stainless steel filters. The results of the different analyses are compiled in Figure 5-19 and Figure 5-20. For the two cells, it was possible to differentiate the following components in the unaltered HCP area: unreacted cement clinkers (C2S/C3S/C4AF), hydration products (HP, including at least C-S-H, portlandite, monosulfate, ettringite, hemicarboaluminate, monocarboaluminate, katoite and calcite), very porous products (principally consisting in AFt, AFm and calcite spherules) that can be separated from other HP (Hu and Ma, 2016) and coarse porosity. The unaltered HCP SEM images show characteristics of naturally carbonated HCP, with the presence of calcite spherules and the impossibility to discriminate between portlandite and other HP products (Shah et al., 2018) (Figure 5-19).

The major difference between the two cells is the remaining UC content in the HCP, which is two times larger in the SM539 cell. Indeed, the amount of C3S/C2S replaced by inner hydration products is larger in the SON68 cell (Figure 5-21). It should be noticed that the analyses were performed at a distance not further than 1 mm from the interface with the stainless steel filters, and thus the ingress of H₃SiO₄⁻ from the glass dissolution and its further diffusion in the HCP can be responsible for the higher hydration rate observed in the cell with SON68 glass. Indeed, the release of H₃SiO₄⁻ was much more important in this cell (see Table 5-8) than in the cell with SM539 glass.

At the interface, the following components were discriminated: unreacted cement (C2S/C3S/C4AF), calcite, hydration products (including at least C-S-H, monosulfate, ettringite, hemicarboaluminate, monocarboaluminate, katoite), very porous C-S-H with low Ca/Si ratio and coarse porosity. Note that the high discrepancy in the different component grey level values at the interface is due to the important heterogeneity of the interfaces, as well as the low surface analysed in each BE image. However, due to the important area analysed in both cells, the mean value is representative of the sample.

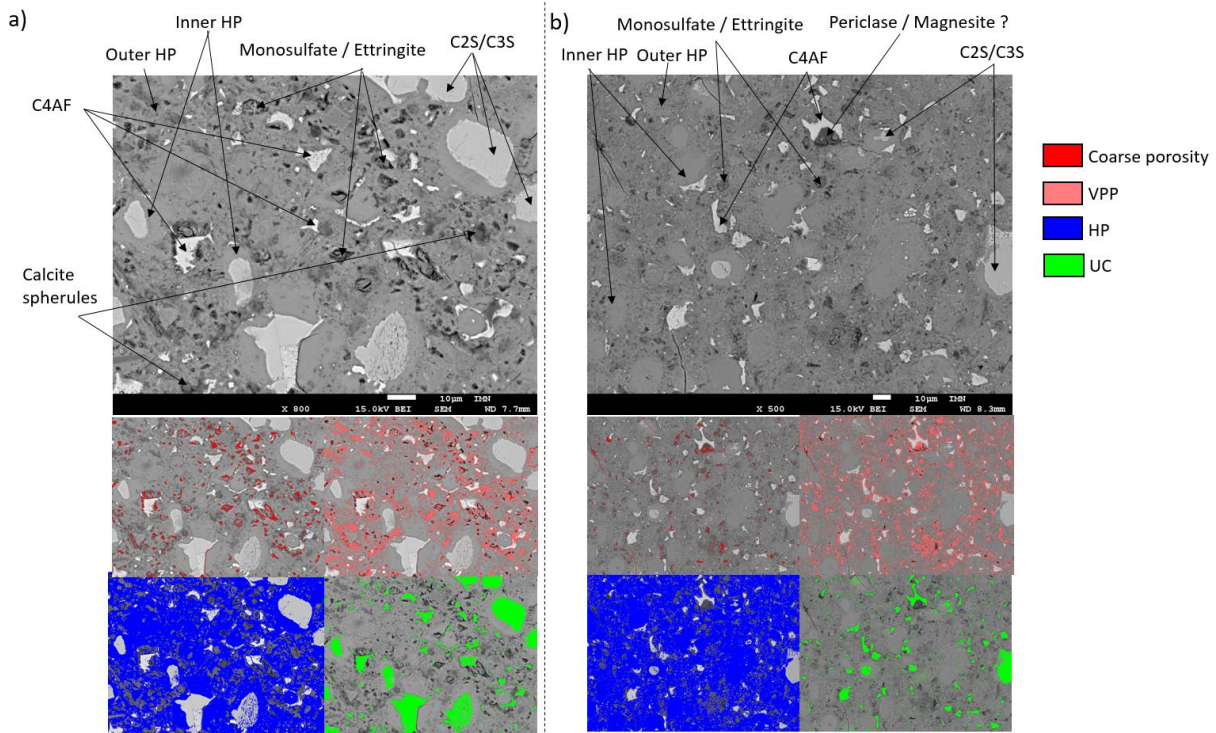


Figure 5-19 – Annotated BE-SEM images of the HCP in the SM539 cell (a) and in the SON68 cell (b) at a distance greater than 400 μm from interface, along with the corresponding maps which show coarse porosity (red), Very porous products (VPP pink), Hydration Products (HP blue), Unreacted Cement (UC green).

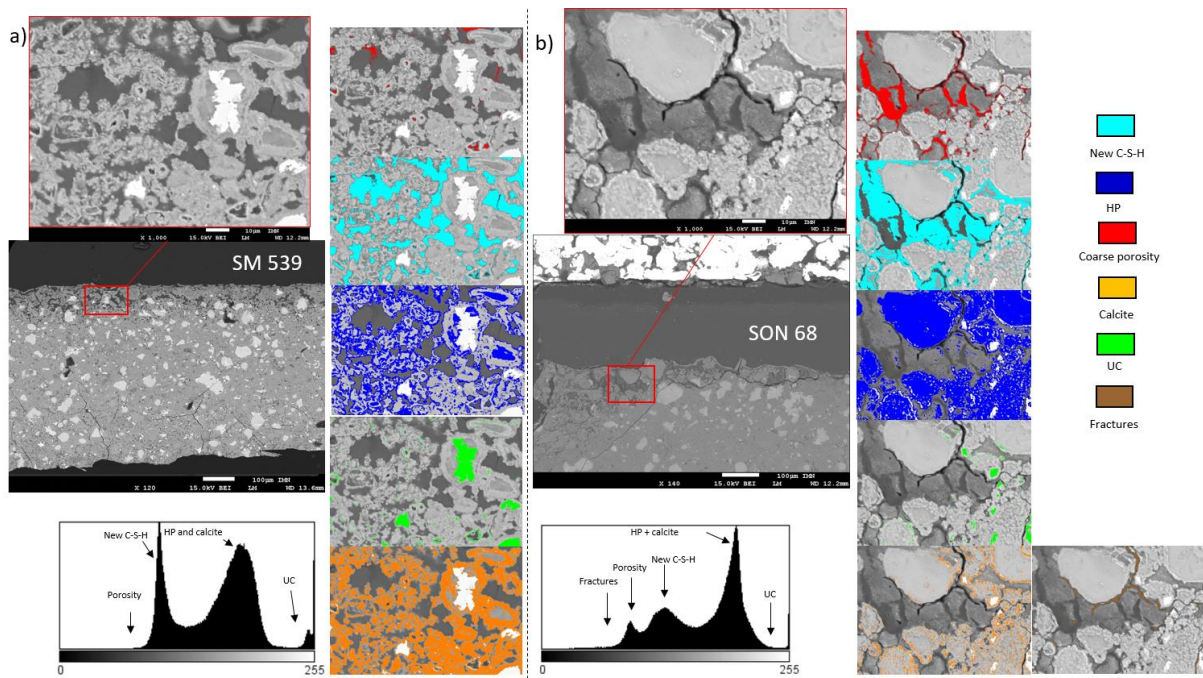


Figure 5-20 – BE-SEM images of the HCP at the interface with SM539 glass (a) and SON68 glass (b), along with the gray level histograms and the corresponding maps which show fractures (brown), macroporosity (red), newly formed C-S-H with low Ca/Si ratio (light blue), hydration products (HP, blue), carbonated hydrates (orange), unreacted cement (UC, green) and fractures (brown).

The evolution of the microstructural and mineralogical features of the HCP at the interface with SON68 and SM539 glass, is summarized in the following sections:

Mineralogical evolution: Major mineralogical changes occur at the interface between HCP and glass in both cells. First, the UC content decreases for both cells (Figure 5-21 and Figure 5-22), and particularly for the SON68 cell. This can be related to the continuous hydration of the UC grains in this area due to the continuous leaching of the HP forming at the surface of the UC grains. Thus, UC grains, totally replaced by inner HP are visible at the interface (Figure 5-20). Secondly, the presence of large amount of carbonates, already depicted by XRD as calcite, is revealed by this technique. Lastly, an important amount of C-S-H with low Ca/Si and with an important alkali uptake precipitate in the porosity generated by the leaching of the HCP, due to the input of Si from glass dissolution and portlandite leaching. This phase, forming fibrous clusters, is particularly well discriminated in the grey level histograms (Figure 5-20). However, due to the high porosity content of this cluster, it is difficult to assess the exact amount of tobermorite like C-S-H phase that precipitates at the interface.

Note that the denser product that precipitate at the edge of the HCP interface with stainless steel filter was not integrated in the grey level analyses. This phase, principally composed of ASR gel or low Ca/Si C-S-H enriched in alkalis, measures approximately 30-40 μm (max 160 μm) in the SON68 cell and less than 10 μm in the SM539 cell.

Porosity evolution: In the bulk part of the SON68 cell, the water porosity measurements give a value of (21.3 vol% \pm 2.4), which is very close to the grey level analyses value, combining coarse porosity and very porous HP (22.4 vol% \pm 4). This value increases at the interface between stainless steel filter and HCP to 36.9%, combining the fractures, the coarse porosity and the new very porous C-S-H clusters that fill the pores generated by the HP leaching.

In the SM539 cell, the combined value of coarse porosity and VPP (20.5 vol% \pm 3.5) is lower than the porosity measured by water porosity measurements (25.9 vol% \pm 0.3%). The porosity, combining the fractures, the coarse porosity and the new very porous C-S-H clusters, only slightly increase to 22.4% at the interface, even if the size of pores and the porosity connectivity are much greater than in the unaltered HCP.

It should be noticed that an important amount of nanopores are also present in the HP and the calcite components, which means that the porosity is greater at the interface. An analysis of the nanoporosity of the HP and carbonated product is thus necessary to obtain accurate results on the porosity evolution at the interface.

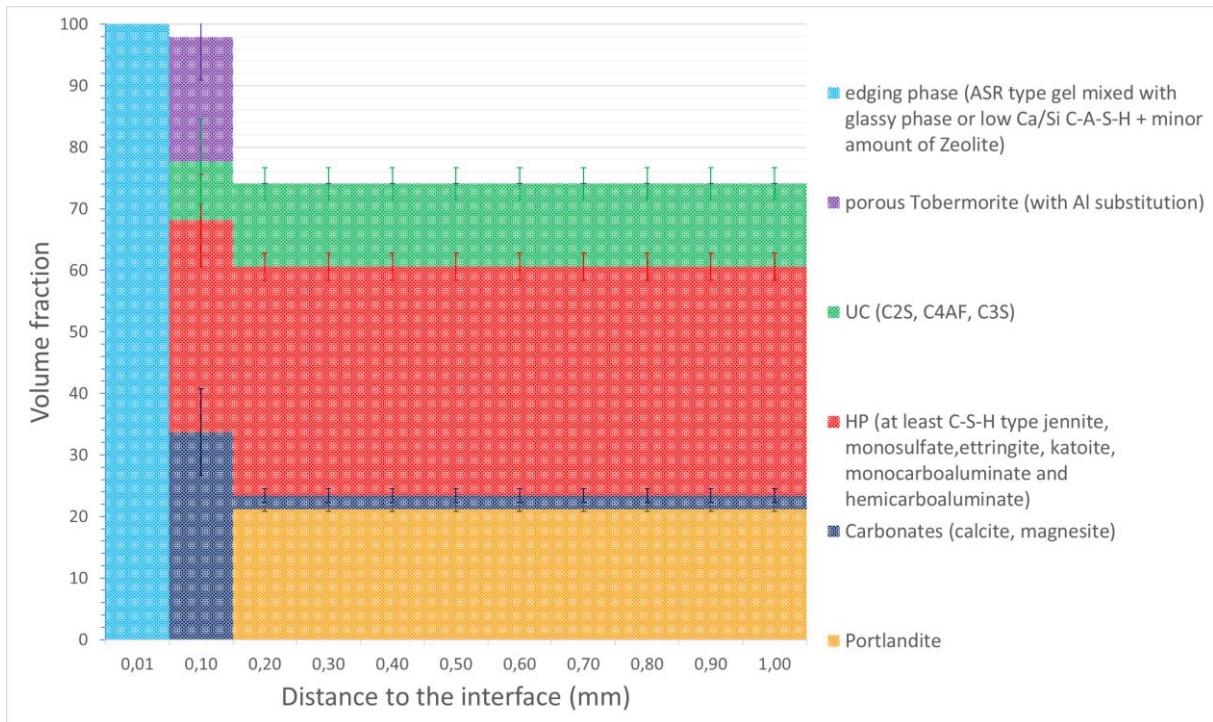


Figure 5-21 – Mineralogical and microstructural evolution in the HCP for SM539 cell obtained by gray level analyses except for porosity, carbonates and portlandite content in the unaltered area (100 μ m to 1mm). In this latter, porosity was obtain from water porosity measurement and portlandite and carbonate contents were obtained by TG-DSC measurements.

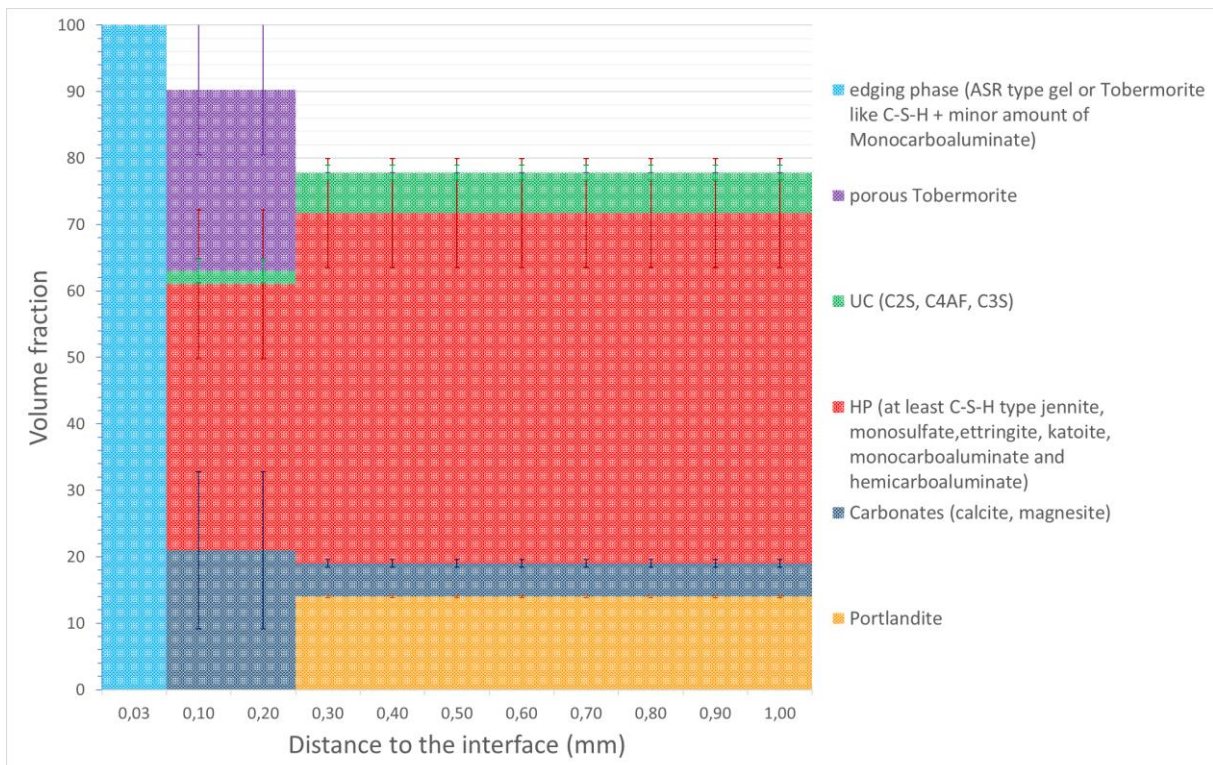
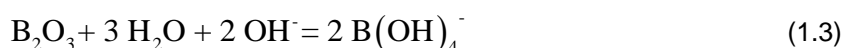


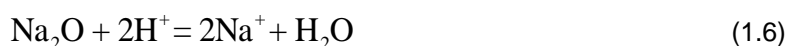
Figure 5-22 – Mineralogical and microstructural evolution in the HCP for SON68 cell obtained by gray level analyses except for porosity, carbonates and portlandite content in the unaltered area (200 μ m to 1mm). In this latter, porosity was obtain from water porosity measurement and portlandite and carbonate contents were obtained by TG-DSC measurements.

5.7 Main findings, conceptual models and input towards modelling

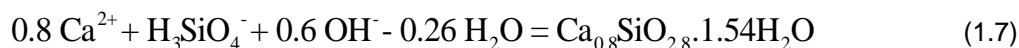
Although the basic dissolution mechanisms of glass are the same at (hyper)alkaline and (near) neutral pH, their relative importance and the dissolution kinetics are different. The solubility of major glass network constituents (SiO_2 , Al_2O_3 , ZrO_2) increases at high pH, favouring congruent dissolution. The high concentrations in solution lead to oversaturation and precipitation of secondary phases that are typical for high pH. At (near) neutral pH, the dissolution rate tends to decrease because of the decreasing affinity (degree of undersaturation for the dissolution rate determining glass constituents). This leads to a steady state, where the alteration layer is in (pseudo) equilibrium with the solution, leading to a low residual dissolution rate. At high pH, such affinity driven model is questionable, because the high solubility destabilizes the alteration layer. Hence, relatively high dissolution rates are observed, together with precipitation of amorphous (low temperature) or crystalline (higher temperature) secondary phases. However, when glass is dissolving in a closed system, the initially high pH can decrease as a result of the dissolution of glass constituents. Such pH decrease can be enhanced at high ratio of glass surface area to solution volume (SA/V). Both dissolution and precipitation reactions can have an effect on the pH. Hereunder the most important reactions considered in the modelling (D2.14, in preparation) are listed. Dissolution of glass network formers and intermediates such as Si, B and Al oxides tends to decrease the solution pH as indicated in Equations (1.2) to (1.4).



On the other hand, dissolution of glass network modifiers such as Ca and Na oxides tends to increase the solution pH as indicated in Equations (1.5) and (1.6).



Not only the dissolution reaction, but also precipitation of secondary phases from the solution can change the solution pH in both direction. For example, equilibrium precipitation of calcium silicate hydrates (C-S-H) such as CSH0.8 in Equation (1.7) and zeolites such as phillipsite_K in Equation *equation reference goes here* has the opposite effect on the solution pH, *i.e.* C-S-H precipitation decreases the solution pH by consuming OH^- ions while phillipsite K precipitation increases the solution pH by consuming H^+ ions from the solution.



When the (hyper) alkaline leaching medium contains (hardened) cement paste, reactions between glass and cement paste constituents will be promoted.

The main mechanisms according to which the glass interacts with fresh OPC concrete are

- (I) the reaction of Si released from the glass with portlandite to form Calcium Silicate Hydrates (C-S-H), *i.e.* the *pozzolanic reaction*,
- (II) the reaction of the Al released from the glass with the C-S-H phases to form Calcium Aluminium Silicate Hydrates (C-A-S-H phases),
- (III) the further enrichment of the C-S-H phases with Si,
- (IV) the formation of an Alkali – Silica – Reaction (A-S-R) gel.

In degraded OPC concrete, where all portlandite has been converted into C-S-H, carbonated or leached, only the 2nd, 3rd, and possibly the 4th mechanism should be important. Unfortunately, very little is known about the effective impact of these mechanisms on the glass alteration rate. The experiments performed so far to study the impact of cement phases on glass alteration typically focused on systems at pH 12.5 to <13, where the reaction with portlandite triggers the glass dissolution. No experiments have been done with old OPC concrete (C-S-H, 10.5 < pH < 12) or iron containing C-S-H phases. Tests with old OPC concrete water in initial equilibrium with C-S-H, but without addition of the solid phases have been performed, though. They suggest that low dissolution rates can be reached at pH \approx 11, probably thanks to the protective effect of the remaining Ca (Ferrand et al., 2018) in the old cement water. Hence, in absence of more focused studies and for the time being, one can assume that the glass dissolution mechanisms in the old OPC concrete are similar to the mechanisms in more neutral pH media, including the potential temporary triggering effect of the iron (corrosion products).

The mock-up experiment described in this report was done with fresh OPC, though. It was designed as a complement to tests in high pH cementitious solutions without OPC phases.

In the experiments without OPC phases, the dissolution rate tends to decrease with time, but the mechanisms explaining this decrease are not clear. In tests at high SA/V, where an advanced reaction progress is reached, the aforementioned pH decrease will be part of the explanation. Whether an affinity effect plays also a role at high pH is not yet clear. The leaching data can in general be fitted well by diffusion processes, though. The currently used conceptual model to interpret the leaching experiments at high pH thus assumes a congruent dissolution followed by reprecipitation of an alteration layer. Hence the dissolution of the glass at high pH is described as a process of diffusion through this growing alteration layer, and the dissolution kinetics are controlled by the diffusion properties of this layer, summarized in the lumped parameter called effective diffusion coefficient (D_{glass}).

In the presence of OPC phases, an alteration layer is formed not only on the glass, but also on the cement paste surface, where the reactions (I) to (IV) also take place.

Reactions between glass and cement constituent thus take place on or in the glass surface, in the solution, and on or in the cement surface. Cement components such as $K^+ \cdot Mg^{2+}$ and Ca^{2+} can diffuse into the glass alteration layer, while glass components such as boron ($B(OH)_4^-$) can diffuse into the cement alteration layer. The transport of species in the cement is also diffusion controlled, with a different effective diffusion coefficient D_{cement} . The interaction between glass and cement could thus be described as a set of reactive transport processes.

The mock-up experiments reported here allow to determine these diffusion profiles, but the focus of the used techniques was on the profiles in the cement, where the profiles are much thicker than the very thin alteration layers on the glass particles. Hence the experiment could be used to validate conceptual models and to fit parameter values.

The modelled experiment also includes a stainless steel filter separating the glass and the concrete. This filter simulates the iron corrosion product layer that is expected to be formed at the glass/canister-overpack interface. At high pH, the corrosion rate of steel is very low. Hence the reaction of the stainless steel with the solution, the glass and the cement was expected to be negligible, and this is also confirmed by the characterization (see section 5.4). The stainless steel filter thus provides merely an inert permeable separation between the glass and the cement. The experiment can be used to evaluate the effect of such separation, which will exist also in the real disposal system, where the iron alteration layer will be thicker and denser.

The applied model (D2.14, in preparation) considers the following processes:

- The porosity and initial condition in the cement are defined through a cement hydration model. This includes sorption of K and Na on tobermorite and jennite (C-S-H) using distribution coefficients from literature. This results in a calculated mineralogical composition of the

hardened cement paste, a calculated bulk porosity, and an equilibrium composition of the pore water. This can be compared to the experimental data obtained in subtask 3.1.

Dissolution of cement hydration products and precipitation of secondary phases may alter the volume fraction of the free water in the cement and thus change the porosity. A porosity change can affect the diffusion coefficient, but in an approximation the system can also be described assuming constant diffusion coefficients.

Three diffusion coefficients are required to modelling such a system: (1) the diffusion coefficient in the glass, (2) the diffusion coefficient in the iron filter, and (3) the diffusion coefficient in the cement. The diffusion coefficients in the glass and cement are fitting parameters in the modelling. The diffusion coefficient in the iron filter is related to the known porosity of the iron filter.

The mock-up test cells were saturated at the start of the experiment with synthetic young cement water, with a similar composition as the theoretical composition calculated with the cement model used to model the mock-up experiments.

- To fit the diffusion coefficient in the cement paste (D_{cement}) and in the glass alteration layer (D_{glass}), the combined data were used from (1) the measured B concentration evolution in the cement pore water of the glass compartment and (2) the boron diffusion profiles in the cement, measured by LA-ICP-MS. Because boron is known to sorb on cement phases, a distribution coefficient K_f for boron had to be fitted as well. The model do not consider the precipitation of B-bearing phase or substitution of B in phases such as AFt or AFm as such phenomenon were not observed experimentally.

The effect of the stainless steel filter was evaluated in the geochemical model (ref D2.14). The filter was not considered as a diffusion barrier. However, precipitation in the filter pores was observed, decreasing the porosity.

- A reactive coupled transport model is used to simulate the formation of reaction products (minerals), the porosity evolution and the pH of the pore water in the cement close to the steel filter and glass.
- The profiles of calcium, silica, alumina, potassium and sodium in the cement, measured by LA-ICP-MS, as well as the experimentally observed mineralogical changes are used to validate the reactive transport model.

The glass dissolution model used to simulate the experiment with the mock-up tests thus describes the dissolution process as a series of coupled transport processes, governed by the transport properties of the interface layers. The diffusion coefficients are the main parameters that are derived from the experiment. The forward rate of dissolution of the glass plays a role only on the short term. The glass composition could have an effect if it affects the diffusion properties of the glass and cement alteration layers. The ratio of the glass surface area to solution volume (SA/V) is fixed from the start and is also related to the diffusion coefficient (higher SA/V leads to smaller D_{glass})

6 Conclusions

This deliverable intends to give an overview of information obtained on experiments that were studied in subtask 3.1.

Characterizations performed on the altered/corroded solids, along with the solution data can be used for modelling purposes. It can be noted that the level of information significantly differs between studies. This can be explained by the date of availability of the samples along with the means dedicated to each study.

In study 1 and 4, a lot of details are provided on the alteration products formed during interaction between glass, steel and near-field materials thanks to multiscale analytical approaches. It is worth noting that the identification of neoformed phases is difficult because the amount of products is generally small and phases are generally poorly crystallized. Even though they have been identified, their thermodynamic properties are not necessarily available in geochemical database. In this case, they must be estimated/calculated.

The rate of steel corrosion or glass alteration is generally estimated from the thickness of corrosion/alteration layers. This is a common and useful assumption but which suffers of uncertainty, especially if the glass alteration layer is formed by precipitation. In that case, either the molar volume of the neoformed phases or the space available for precipitation can impact the volume of alteration products.

Although static and compact experiments (high solid/liquid ratio) are more representative of actual disposal conditions, it is difficult to collect and analyse pore water. In experiment 1, an attempt was performed to flush the pore water, but the results cannot be used, likely because the injected solution passed through preferential pathways. Experiment 4 is the more complete experiment with a special design allowing the collection and analysis of pore water.

For the modelling effort at the laboratory scale, it is proposed to focus on experiments 1 and 4, which provide the largest set of data. The two experiments explore most of the situations expected for HLW glass in Europe (near neutral to hyperalkaline pHs). It is recommended to consider glass dissolution at a constant rate of following a first order rate law based on Si and steel corrosion at a constant rate. In the perspective of upscaling the models, the geometry is a key aspect of the problem. Two other parameters not taken into account is the laboratory experiments should be kept in mind: the fractures within the glass block, the effects of radioactivity on the mechanisms of glass dissolution and secondary phase precipitation. So far, the last mechanism have been poorly studied.

7 References

- ANDRA 2016 Safety Options Report - Operating Part (DoS-Expl).
- Babaei, S., Seetharam, S.C., Dizier, A., Steenackers, G. and Craeye, B. 2021. An analytical framework for estimating drying shrinkage strain of OPC based hardened cement paste. *Cement and Concrete Composites* 115, 103833.
- Balachandran, C., Munoz, J.F. and Arnold, T. 2017. Characterization of alkali silica reaction gels using Raman spectroscopy. *Cement and Concrete Research* 92, 66-74.
- Bouakkaz, R., Abdelouas, A., El Mendili, Y., Grambow, B. and Gin, S. 2016. SON68 glass alteration under Si-rich solutions at low temperature (35-90 degrees C): kinetics, secondary phases and isotopic exchange studies. *Rsc Adv* 6(76), 72616-72633.
- Bourdelle, F., Benzerara, K., Beyssac, O., Cosmidis, J., Neuville, D.R., Brown, G.E. and Paineau, E. 2013. Quantification of the ferric/ferrous iron ratio in silicates by scanning transmission X-ray microscopy at the Fe L-2,L-3 edges. *Contrib Mineral Petr* 166(2), 423-434.
- Bradbury, M.H. and Baeyens, B. 1997a Derivation of In Situ Opalinus Clay Porewater Compositions from Experimental and Geochemical Modelling Studies. PSI.
- Bradbury, M.H. and Baeyens, B. 1997b. A mechanistic description of Ni and Zn sorption on Namontmorillonite Part II: modelling. *Journal of Contaminant Hydrology* 27(3), 223-248.
- Carriere, C., Dillmann, P., Foy, E., Neff, D., Dynes, J.J., Linard, Y., Michau, N. and Martin, C. 2019. Use of nanoprobe to identify iron-silicates in a glass/iron/argillite system in deep geological disposal. *Corrosion Science* 158.
- Carriere, C., Dillmann, P., Gin, S., Neff, D., Gentaz, L., Bruguier, F., Monnet, I., Gardes, E., Saheb, M., Foy, E., Nuns, N., Delanoe, A., Dynes, J.J., Michau, N. and Martin, C. 2021. The fate of Si and Fe while nuclear glass alters with steel and clay. *Npj Materials Degradation* 5(1).
- Champenois, J.B., Mesbah, A., Coumes, C.C.D., Renaudin, G., Leroux, F., Mercier, C., Revel, B. and Damidot, D. 2012. Crystal structures of Boro-AFm and sBoro-AFt phases. *Cement and Concrete Research* 42(10), 1362-1370.
- Dauzères, A. (2010) Etude expérimentale et modélisation des mécanismes physico-chimiques des interactions béton-argile dans le contexte du stockage géologique des déchets radioactifs, Université de Poitiers.
- Dohmen, L., Lenting, C., Fonseca, R.O.C., Nagel, T., Heuser, A., Geisler, T. and Denkler, R. 2013. Pattern Formation in Silicate Glass Corrosion Zones. *Int J Appl Glass Sci* 4(4), 357-370.
- Duque-Redondo, E., Yamada, K., Lopez-Arbeloa, I. and Manzano, H. 2018. Adsorption and Diffusion of Na⁺, Cs⁺ and Ca²⁺ Ions in C-S-H and C-a-S-H Nanopores. *ChemRxiv*.
- Fábián, M., Proffen, T., Ruett, U., Veress, E. and Sváb, E. 2010. Uranium surroundings in borosilicate glass from neutron and x-ray diffraction and RMC modelling. *Journal of Physics Condensed Matter* 22(40).
- Fábián, M., Sváb, E., Mészáros, G., Révay, Z., Proffen, T. and Veress, E. 2007. Network structure of multi-component sodium borosilicate glasses by neutron diffraction. *Journal of Non-Crystalline Solids* 353(18-21), 2084-2089.
- Fábián, M., Sváb, E. and Zimmermann, M.V.M.V. 2013. Structure study of new uranium loaded borosilicate glasses. *Journal of Non-Crystalline Solids* 380, 71-77.
- Ferrand, K., Lemmens, K. and Liu, S. 2018 Integrated leach tests with simulated HLW glass in contact with ordinary Portland cement paste: Topical Report. ER-0431.
- Ferrand, K., Liu, S.H. and Lemmens, K. 2013. The Interaction Between Nuclear Waste Glass and Ordinary Portland Cement. *Int J Appl Glass Sci* 4(4), 328-340.
- Francois, M., Renaudin, G. and Evrard, O. 1998. A cementitious compound with composition 3CaO.Al₂O₃.CaCO₃.11H₂O. *Acta Crystallogr C* 54, 1214-1217.

EURAD Deliverable D2.12 – High level radioactive waste package – Characterization of glass/steel/buffer interaction experiments

- Gagnon, J.E., Fryer, B.J., Samson, I.M. and Williams-Jones, A.E. 2008. Quantitative analysis of silicate certified reference materials by LA-ICPMS with and without an internal standard. *J Anal Atom Spectrom* 23(11), 1529-1537.
- Gates, W.P., Klopogge, J., Madejova, J. and Bergaya, F. (2017) *Infrared and Raman Spectroscopies of Clay Minerals*, Elsevier.
- Geisler, T., Nagel, T., Kilburn, M.R., Janssen, A., Icenhower, J.P., Fonseca, R.O.C., Grange, M. and Nemchin, A.A. 2015. The mechanism of borosilicate glass corrosion revisited. *Geochimica Et Cosmochimica Acta* 158, 112-129.
- Gharibi, E., Jabri, M. and Ramdani, A. 2017. The effect of magnesium on the alite phase structural stability and its hydration process. *Journal of Materials and Environmental Science* 8, 1312-1319.
- Gin, S., Jollivet, P., Fournier, M., Berthon, C., Wang, Z.Y., Mitroshkov, A., Zhu, Z.H. and Ryan, J.V. 2015. The fate of silicon during glass corrosion under alkaline conditions: A mechanistic and kinetic study with the International Simple Glass. *Geochimica Et Cosmochimica Acta* 151, 68-85.
- Gin, S., Ribet, I. and Couillard, M. 2001. Role and properties of the gel formed during nuclear glass alteration: importance of gel formation conditions. *Journal of Nuclear Materials* 298, 1-10.
- Gin, S., Tocino, F., Ferrand, K., Martin, C. and Fabian, M. 2019 HLW: Report describing the selected experiments and the existing/expected experimental results. Final version as of 17/12/2019 of deliverable D2.10 of the HORIZON 2020 project EURAD. EC Grant agreement no: 847593.
- Hong, S.Y. and Glasser, F.P. 1999. Alkali binding in cement pastes Part I. The C-S-H phase. *Cement and Concrete Research* 29(12), 1893-1903.
- Hu, C.L. and Ma, H.Y. 2016. Statistical analysis of backscattered electron image of hydrated cement paste. *Advances in Cement Research* 28(7), 469-474.
- Jollivet, P., Gin, S. and Schumacher, S. 2012. Forward dissolution rate of silicate glasses of nuclear interest in clay-equilibrated groundwater. *Chemical Geology* 330, 207-217.
- Kirkpatrick, R.J., Yarger, J.L., McMillan, P.F., Yu, P. and Cong, X.D. 1997. Raman spectroscopy of C-S-H, tobermorite, and jennite. *Advanced Cement Based Materials* 5(3-4), 93-99.
- L'Hopital, E., Lothenbach, B., Kulik, D.A. and Scrivener, K. 2016a. Influence of calcium to silica ratio on aluminium uptake in calcium silicate hydrate. *Cement and Concrete Research* 85, 111-121.
- L'Hopital, E., Lothenbach, B., Scrivener, K. and Kulik, D.A. 2016b. Alkali uptake in calcium alumina silicate hydrate (C-A-S-H). *Cement and Concrete Research* 85, 122-136.
- Labbez, C., Pochard, I., Jonsson, B. and Nonat, A. 2011. C-S-H/solution interface: Experimental and Monte Carlo studies. *Cement and Concrete Research* 41(2), 161-168.
- Lafuente, S.N., Downs, R.T. and Yang, H. (2015) *Highlights Mineralogical Crystallography*. Armbruster, T. and Danisi, R.M. (eds), W. De Gruyter, Berlin.
- Lalan, P. (2016) Influence d'une température de 70°C sur la géochimie, la microstructure et la diffusion aux interfaces béton/argile : expérimentations en laboratoire, in situ et modélisation.
- Lantenois, S., Lanson, B., Muller, F., Bauer, A., Jullien, M. and Plancon, A. 2005. Experimental study of smectite interaction with metal Fe at low temperature: 1. Smectite destabilization. *Clays and Clay Minerals* 53(6), 597-612.
- Leemann, A., Shi, Z.G. and Lindgard, J. 2020. Characterization of amorphous and crystalline ASR products formed in concrete aggregates. *Cement and Concrete Research* 137.
- Leon, Y., Dillmann, P., Neff, D., Schlegel, M.L., Foy, E. and Dynes, J.J. 2017. Interfacial layers at a nanometre scale on iron corroded in carbonated anoxic environments. *Rsc Adv* 7(33), 20101-20115.
- Li, P.R., Li, W.G., Yu, T., Qu, F.L. and Tam, V.W.Y. 2020. Investigation on early-age hydration, mechanical properties and microstructure of seawater sea sand cement mortar. *Construction and Building Materials* 249.

EURAD Deliverable D2.12 – High level radioactive waste package – Characterization of glass/steel/buffer interaction experiments

- Liu, Y.S., Hu, Z.C., Gao, S., Gunther, D., Xu, J., Gao, C.G. and Chen, H.H. 2008. In situ analysis of major and trace elements of anhydrous minerals by LA-ICP-MS without applying an internal standard. *Chemical Geology* 257(1-2), 34-43.
- Longerich, H.P., Jackson, S.E. and Gunther, D. 1996. Laser ablation inductively coupled plasma mass spectrometric transient signal data acquisition and analyte concentration calculation. *J Anal Atom Spectrom* 11(9), 899-904.
- Mann, C., Ferrand, K., Liu, S., Eskelsen, J.R., Pierce, E., Lemmens, K. and Corkhill, C. 2019. Influence of young cement water on the corrosion of the International Simple Glass. *Npj Materials Degradation* 3(1).
- Michelin, A., Drouet, E., Foy, E., Dynes, J.J., Neff, D. and Dillmann, P. 2013. Investigation at the nanometre scale on the corrosion mechanisms of archaeological ferrous artefacts by STXM. *J Anal Atom Spectrom* 28(1), 59-66.
- Mitchell, L.D., Margeson, J.C. and Beaudoin, J.J. 2007. Synthesis and characterisation of lithium and sodium doped C-S-H, pp. 1-17.
- Music, S., Ristic, M., Gotic, M. and Foric, J. 1988. Corrosion of Simulated Nuclear Waste Glass. *J Radioan Nucl Ch Ar* 122(1), 91-102.
- Neeft, E., Weetjens, E., Vokal, A., Leivo, M., Cochepin, B., Martin, C., Munier, I., Deissmann, G., Montoya, V., Poskas, P., Grigaliuniene, D., Narkuniene, A., Garcia, E., Samper, J., Montenegro, L. and Mon, A. 2020. Treatment of chemical evolution in National Programmes, D 2.4 of the HORIZON 2020 project EURAD. . EC Grant agreement no: 847593.
- Nozawa, S., Sato, T. and Otake, T. 2018. Effect of Dissolved Silica on Immobilization of Boron by Magnesium Oxide. *Minerals* 8(2), 76.
- Ortaboy, S., Li, J.Q., Geng, G.Q., Myers, R.J., Monteiro, P.J.M., Maboudian, R. and Carraro, C. 2017. Effects of CO₂ and temperature on the structure and chemistry of C-(A-)S-H investigated by Raman spectroscopy. *Rsc Adv* 7(77), 48925-48933.
- Paton, C., Hellstrom, J., Paul, B., Woodhead, J. and Hergt, J. 2011. Iolite: Freeware for the visualisation and processing of mass spectrometric data. *J Anal Atom Spectrom* 26(12), 2508-2518.
- Roduit, N. 2007. JMicroVision: Image analysis toolbox for measuring and quantifying components of high-definition images. Version 1.2.7.
- Saheb, M., Descostes, M., Neff, D., Matthiesen, H., Michelin, A. and Dillmann, P. 2010. Iron corrosion in an anoxic soil: Comparison between thermodynamic modelling and ferrous archaeological artefacts characterised along with the local in situ geochemical conditions. *Applied Geochemistry* 25(12), 1937-1948.
- Scrivener, K.L. 2004. Backscattered electron imaging of cementitious microstructures: understanding and quantification. *Cement and Concrete Composites* 26(8), 935-945.
- Shah, V., Scrivener, K., Bhattacharjee, B. and Bishnoi, S. 2018. Changes in in microstructure characteristics of cement paste on carbonation. *Cement and Concrete Research* 109, 184-197.
- Stade, H. 1989. On the Reaction of C-S-H(Di,Poly) with Alkali Hydroxides. *Cement and Concrete Research* 19(5), 802-810.
- Suzuki-Muresan, T., Abdelouas, A., Landesman, C., Ait-Chaou, A., El Mendili, Y., Ribet, S., Perrigaud, K., Shitara, D., Martin, C. and Bourbon, X. 2018. Alteration of vitrified intermediate level nuclear waste in alkaline media: effects of cementitious materials, pH and temperature. *Rsc Adv* 8(66), 37665-37680.
- Torrens-Martin, D., Fernandez-Carrasco, L., Martinez-Ramirez, S., Ibanez, J., Artus, L. and Matschei, T. 2013. Raman Spectroscopy of Anhydrous and Hydrated Calcium Aluminates and Sulfoaluminates. *J Am Ceram Soc* 96(11), 3589-3595.
- Utton, C.A., Hand, R.J., Bingham, P.A., Hyatt, N.C., Swanton, S.W. and Williams, S.J. 2013. Dissolution of vitrified wastes in a high-pH calcium-rich solution. *Journal of Nuclear Materials* 435(1-3), 112-122.

EURAD Deliverable D2.12 – High level radioactive waste package – Characterization of glass/steel/buffer interaction experiments

- van Elteren, J.T., Tennent, N.H. and Selih, V.S. 2009. Multi-element quantification of ancient/historic glasses by laser ablation inductively coupled plasma mass spectrometry using sum normalization calibration. *Anal Chim Acta* 644(1-2), 1-9.
- Verney-Carron, A., Gin, S. and Libourel, G. 2010. Archaeological analogs and the future of nuclear waste glass. *Journal of Nuclear Materials* 406(3), 365-370.
- Wang, A.A., Freeman, J.J. and Jolliff, B.L. 2015. Understanding the Raman spectral features of phyllosilicates. *J Raman Spectrosc* 46(10), 829-845.
- Yu, Y., Xiong, G., Li, C. and Xiao, F.S. 2001. Characterization of aluminosilicate zeolites by UV Raman spectroscopy. *Microporous and Mesoporous Materials* 46(1), 23-34.